Optics of dielectric microstructures

Søndergaard, Thomas

Publication date:
2002

Document Version
Publisher's PDF, also known as Version of record

Optics of dielectric microstructures

part 1: emission of radiation by sources
part 2: planar photonic crystal waveguides

Thomas Søndergaard

Research Center COM

Technical University of Denmark

Optics of dielectric microstructures

part 1: emission of radiation by sources
part 2: planar photonic crystal waveguides

Thomas Søndergaard

The thesis is submitted as part of the requirements for obtaining the ph.d degree from the Technical University of Denmark

Supervisors

Anders Bjarklev, Research Center COM

Bjarne Tromborg, Research Center COM

Thomas Søndergaard Kgs. Lyngby, 29. January 2002

Contents

Chapter 1

Introduction

Dielectric microstructures are generally dielectric structures where the refractive index varies on length scales comparable to the optical wavelengths of light that they were designed for. Microstructures are interesting for guiding and processing of light wave signals. In the standard step-index fiber the refractive-index contrast between fiber core and cladding is less than a percent [1]. Mirrors for propagation of light in one dimension may be created by making small periodic refractive-index variations in one dimension on a wavelength scale. Mirrors for propagation of light in two or three dimensions requires large refractive-index contrasts and has been achieved with the class of dielectric microstructures known as photonic crystals [2]. In more recent years attention has been given to microstructures with high refractive-index contrasts, and in particular to structures with microstructure variations in more than one dimension. High-refractive index contrast optical fibers have emerged [3–5]. In planar structures large refractive index contrasts between e.g. silicon and air can be used to confine and manipulate light in small spatial regions [2]. High-refractive-index contrast planar structures have prospective uses in future integrated optics that to some extend may replace electronic processing of signals by optical processing of signals.

1.1 Photonic crystals

Photonic crystals or photonic bandgap structures were proposed in 1987 by Yablonovitch and John [6, 7]. Photonic crystals are interesting because they can be designed to have frequency intervals, photonic bandgaps, where light cannot propagate in the crystal structure for certain directions and certain

polarizations of the light. These frequency intervals are analogous to the electronic bandgaps in semiconductor materials that can be related to the periodic arrangement of atoms on a crystal lattice. Photonic bandgaps were originally defined for three-dimensionally periodic structures, where propagation of light can be completely inhibited for all directions of propagation. Three-dimensionally periodic structures with complete bandgaps have been demonstrated experimentally for microwave frequencies and optical frequencies and include the Yablonovite structure [8], the stacks of logs structure [9], and the silicon based inverse opal structure [10, 11] just to name a few.

Although three-dimensionally periodic photonic crystals with complete bandgaps have been demonstrated experimentally for optical frequencies [10, 11] fabricating these structures for the optical wavelength range is still very difficult by todays technology. Instead there has been intense focus on simpler two-dimensionally periodic structures. The concepts *photonic crystal* and *photonic bandgap* have also commonly been adopted to structures that are only periodic in one and two dimensions. In these structures a complete photonic bandgap does not exist for all directions of propagation and not necessarily for both polarizations of the light. However, a photonic bandgap can exist for propagation in one and two dimensions, respectively.

A bold vision put forward by scientists in the field of photonic crystals is that photonic bandgap materials may make possible a technological revolution for integrated optics in the same way that silicon and other semiconductor materials have made possible the technological revolution within integrated electronics that have e.g. given us computers and a variety of other electronic devices [2, 12]. The discovery of photonic crystals has led to a new field of research that seeks to understand the new physics of these materials and that seeks to take advantage of the new material properties for making novel optical components [2, 13].

As is the case for semiconductor structures, or electronic bandgap structures, also photonic bandgap structures become ever more useful when defects are introduced. An example of a photonic crystal and two types of defects are illustrated in Fig. 1.1. A two-dimensional photonic crystal is illustrated in Fig. 1.1(a). The crystal consists of air-holes arranged periodically on a triangular lattice in silicon. For an appropriate choice of the air-hole diameter D and lattice constant Λ this structure is characterized by a frequency interval, a photonic bandgap, where propagation of light in the xy-plane is not allowed. Fig. 1.1(b) shows a photonic crystal where a line defect has been introduced by removing a row of air-holes. Fig. 1.1(c) shows a photonic crystal where a point defect has been introduced by removing one air-hole. There may for a properly designed defect exist photon

wavefunctions in the region of the defect with frequencies within the photonic bandgap of the surrounding photonic crystal. These wavefunctions are trapped to the region of the defect because they are not allowed in the photonic crystal material surrounding the defect. In the case of the crystal with a point defect (Fig. 1.1(c)) the structure can be used as e.g. an optical microcavity with prospective uses in e.g. laser and resonator designs [14–17].

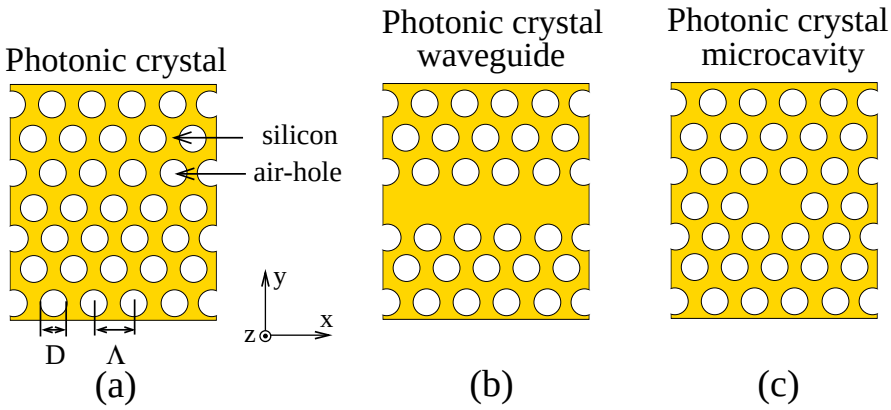

Figure 1.1: Illustration of a photonic crystal (a), and how a waveguide (b) and a cavity (c) can be created by making a line defect and point defect, respectively, in the photonic crystal.

In the case of the crystal with a line defect the structure can be used as a waveguide for electromagnetic waves. It has been suggested that by use of waveguides based on photonic crystals it may be possible to obtain efficient transmission of light (>98%) through sharp bends [18] and branching points [19]. The high refractive-index contrast and the photonic bandgap make possible the creation of small optical components that can be closely spaced. These are important issues for integrated optics, where it is desirable to integrate a large number of optical components together. A photonic crystal microcavity will be encountered in chapter 3. The whole of part II of this thesis is devoted to planar photonic crystal waveguides. Part II advances the understanding of the optical properties of photonic crystal waveguides. Furthermore part II addresses the issue of how to design photonic crystal waveguides with optical properties such as leakage-free guidance of light and large bandwidth.

1.2 Spontaneous and classical emission of radiation from sources in the presence of microstructures

A particular interesting topic for dielectric microstructures is the emission of radiation from sources. The spontaneous emission properties of an emitter changes when it is placed in a small cavity [20], between mirrors [21, 22], or in a medium with spatially varying dielectric constant [23–27]. The general explanation is that a cavity or a varying dielectric constant will modify the strength and distribution of electromagnetic modes with which an emitter can interact, resulting indirectly in altered spontaneous emission properties. The effect was first noticed by Purcell in 1946 [20] and has since been demonstrated in a number of experiments on Rydberg atoms, quantum dots and rare-earth materials [28–37]. One of the perspectives of the effect is that spontaneous emission of an emitter can, to some extend, be controlled and even engineered by tailoring the surrounding structure on a transition wavelength scale.

The experiments for Rydberg atoms [28–30] involve transition wavelengths in the microwave regime, and in this regime metals are excellent conductors that can be used for making good cavities. The rate of spontaneous emission for a transition wavelength matching the wavelength of a cavity mode in good cavities is for narrow-line-width emitters inversely proportional to the cavity linewidth, and inversely proportional to the cavity volume [20].

For optical wavelengths metals are not perfect conductors and to some extend metals absorb light which results in a broadening of the cavity linewidth. This is a good reason for considering instead dielectric materials since dielectric materials can be essentially loss-less at optical frequencies. For example dielectric spheres and circular cylindrically symmetric dielectric disks [27] are examples of good cavity structures, where the light confinement mechanism is total internal reflection of light around the rim of the sphere or disk. The strong resonances for the electromagnetic fields in this type of cavity structures are often referred to as whispering gallery modes.

Properties similar to those of metals can be achieved at optical frequencies with microstructured dielectric materials, namely photonic crystals, which, as is also the case for metals at microwave frequencies, can be used as a perfect mirror. A defect in a three-dimensionally periodic dielectric photonic crystal can be used as a cage for light. In a three-dimensionally periodic photonic crystal there can be frequency intervals, photonic bandgaps,

where there are no electromagnetic modes available, and consequently spontaneous emission may be rigorously forbidden [6]. One of the motivations for working with the topic of emission of radiation in dielectric microstructures is the possibility to reduce, in a semiconductor laser structure, the radiative losses of energy because of spontaneous emission into other modes than the lasing mode. In semiconductor lasers a significant amount of the electric current consumed to produce lasing is wasted due to spontaneous emission of light.

The original formula for enhancement of spontaneous emission suggested by Purcell is useful for good cavities but is not useful for open structures or poor cavity structures. In this thesis methods will be presented for calculating spontaneous emission of radiation from sources in general open inhomogeneous dielectric structures, and a general theory will be put forward for spontaneous emission in structures with absorption and amplification of light. Furthermore the theories will take into account the position of the emitter in the structure, and in some cases the methods also take into account the vector orientation of the emitter. An appropriate method for calculating spontaneous emission in the weak coupling regime is to use a semi-classical approach where spontaneous emission is modelled as being proportional to the emission from an electric dipole emitter. A general source distribution can be composed as a collection of dipole currents, and therefore the methods presented in this thesis do not only apply to spontaneous emission but do also address the classical emission of light from a distribution of current sources.

Some of the methods that will be considered will allow the calculation of near and far fields generated by the sources. This is useful for investigating and engineering the electrodynamic properties of optical components such as vertical cavity surface emitting lasers and light emitting diodes, and for designing antennas and other light-emitting devices with certain preferred directions of the emission of radiation.

1.3 Outline of the thesis

From the work carried out within the ph.d-project two topics have been selected for this thesis, namely emission of radiation by sources in dielectric microstructures, and planar photonic crystal waveguides. The work done within the first topic, emission of radiation by sources in dielectric microstructures, will be presented in the part I of this thesis consisting of the chapters 2-5. An introduction is given in chapter 2. In part I three meth-

ods are presented for calculating spontaneous and classical emission from sources in dielectric microstructures. The first method presented in chapter 3 is based on the Fermi Golden Rule, and spontaneous emission from emitters in a passive dielectric microstructure is calculated by summing over the emission into each electromagnetic mode of the radiation field. This method is applied to investigate spontaneous emission in a two-dimensional photonic crystal and photonic crystal microcavity. In chapter 4 a general theory based on a Green's tensor formalism is put forward for spontaneous emission in active dielectric microstructures, and an example is given where the method is applied to a fiber amplifier. The Green's tensor in chapter 4 is constructed as a summation over a biorthogonal set of electromagnetic modes. An alternative method based on a Lippmann-Schwinger type integral equation is presented in chapter 5 for the construction of the Green's tensor and calculation of emission of radiation by sources. The integral equation approach is applied to calculate near fields and far fields generated by a dipole emitter in finite-sized dielectric disks.

A collection of results obtained within the second topic, planar photonic crystal waveguides, are presented in part II of this thesis consisting of the chapters 6-10. Chapter 6 contains a further introduction to the topic planar photonic crystal waveguides. Chapter 7 contains fundamental research on the electromagnetic energy flow and the number of guided modes versus waveguide width and frequency for two-dimensional photonic crystal waveguides. In chapter 8 it is shown how two-dimensional calculations for infinite-height photonic crystal waveguides can be used to obtain guidelines for the design of leakage-free finite-height planar photonic crystal waveguides. Guidelines are obtained by comparing the two-dimensional calculations to dispersion relations for the media above and below the finite-height waveguide. In chapter 9 both a two-dimensional and three-dimensional theoretical analysis is presented for a photonic crystal waveguide based on the semiconductor-on-insulator materials system. The chapter 10 addresses the design of planar photonic crystal waveguides that support leakage-free guidance of light over a large bandwidth.

Part I

Emission of radiation by sources in dielectric microstructures

Chapter 2

Introduction - part I

The chapters 3-5 contain a collection of contributions to the understanding and modelling of emission of radiation by sources in dielectric microstructures. The chapters 3-4 concern semi-classical models for spontaneous emission in dielectric microstructures, whereas the chapter 5 concerns classical emission of light from a distribution of current sources. In the models for spontaneous emission the emitter, which can e.g. be an excited atom or a quantum dot, is treated as a classical electric dipole current source. The rate of emission from a dipole current source depends on the dielectric environment in much the same way as the rate of spontaneous emission from an excited atom. The methods that will be presented for calculating spontaneous emission can therefore also be applied to calculate classical emission of light from a distribution of current sources. The method for classical emission can correspondingly be applied to calculate spontaneous emission. In the analysis we restrict ourselves to the regime where the coupling between field and emitter is sufficiently weak for reabsorption of emitted light by the emitter to be negligible.

For *passive* dielectric structures it is possible to calculate the position-dependent rate of spontaneous emission by use of the Fermi Golden Rule, where the spontaneous emission is calculated as the sum of emission into each electromagnetic mode. The coupling to an electromagnetic mode for a dipole emitter with random orientation is proportional to the amplitude of the electric field squared of the mode at the position of the emitter. In this model each electromagnetic mode is normalized to one quantum of energy, and a complete set of power orthogonal electromagnetic modes exists. The method can be applied to open structures where a continuum of electromagnetic states exists. The approach is applied to investigate spontaneous

emission in a photonic crystal and a photonic crystal microcavity in chapter 3. The model used here assumes that the structures considered are periodic structures, and the fields are calculated by use of plane-wave-expansion theory and a variational principle. Chapter 3 is based on Ref. [38].

For dielectric microstructures with absorption or gain the concept of modes becomes more subtle. In that case a complete set of power-orthogonal electromagnetic modes does not exist, and the method used in chapter 3 cannot be applied. In chapter 4 a general theory is presented for spontaneous emission in active dielectric microstructures. For active dielectric microstructures it is convenient to use the electromagnetic fields and generating currents as primary observables represented by operators that are defined by their commutation relations. The relation between field and current operators is given by the classical electric field Green's tensor. The rate of spontaneous emission can be related to the transverse Green's tensor. A method is given for calculating the Green's tensor based on a summation over a complete set of biorthogonal electromagnetic modes. The method is exemplified for the case of an active step-index fiber which is sufficiently simple to allow analytic solutions. The solutions illustrate some subtle issues concerning the singularity of the Green's tensor that are not easily studied by purely numerical methods. Chapter 4 is based on material from Ref. [39].

In chapter 5 the emission of radiation from a dipole source in finite-sized dielectric structures is investigated using a vectorial integral equation method. The calculation of the dipole field is equivalent to calculating elements of the electric field Green's tensor. In the integral-equation method the finite-sized dielectric microstructure is discretized, and the electric field is assumed constant within each discretization element. For general three-dimensional structures a large number of discretization elements is required to obtain acceptable convergence. The chapter 5 contains a method for taking advantage of cylindrical symmetry in dielectric structures. By taking advantage of cylindrical symmetry a large reduction is obtained in the required number of discretization elements. The standard approach in the integral equation method is to assume the field constant within each discretization element. However, for e.g. a dipole sources inside the dielectric structure the dipole field is singular in the region which is discretized, and the assumption of constant field within discretization elements is problematic. A method is presented in chapter 5 for removing the field singularity from the integral equations. The chapter is partly based on material from Ref. [40].

Chapter 3

Spontaneous emission in two-dimensional photonic crystal microcavities

3.1 Introduction

In this chapter the rate of spontaneous emission from emitters in passive microstructured dielectric media is modelled by use of the Fermi Golden Rule. In this method the electromagnetic field operator is expanded in a complete set of power-orthogonal electromagnetic modes. The spontaneous emission is calculated as the sum of spontaneous emission into each mode. The method that will be presented can be used for calculating spontaneous emission from emitters in open structures, and not just good cavity structures. Furthermore, the position of the emitter in the structure is taken into account through the concept of the position-dependent photon density of states (DOS). It is shown how the model combined with plane-wave-expansion theory can be applied to calculate spontaneous emission from emitters in periodic dielectric structures such as photonic crystals. It is in principle not a restriction that the method has to be applied to periodic structures because non-periodic structures can always be approximated by a periodic structure.

The microstructures that will be focused on are a photonic crystal and a photonic crystal microcavity. One example of these structures created by introducing properly arranged air-holes in a semiconductor material are analyzed in detail. The structures that will be considered have been used in experimental work by Painter et. al. for making a laser with a pho-

tonic crystal microcavity [14, 41]. One of the interesting prospects of using photonic crystals for making lasers is that it may be possible to control spontaneous emission and reduce the fraction of spontaneous emission into other electromagnetic modes than the lasing mode. This reduction can for example be achieved by making a structure where the number or density of other modes than the lasing mode is small. In particular the density of modes in a photonic crystal can be reduced to zero for certain frequency intervals, the bandgaps, for three-dimensional photonic crystals. Significant modifications in the density of modes are also possible for two-dimensional photonic crystals. In this chapter we will concentrate on spontaneous emission rate alteration in the two-dimensional structures shown in Fig. 3.1(a) and Fig. 3.1(b).

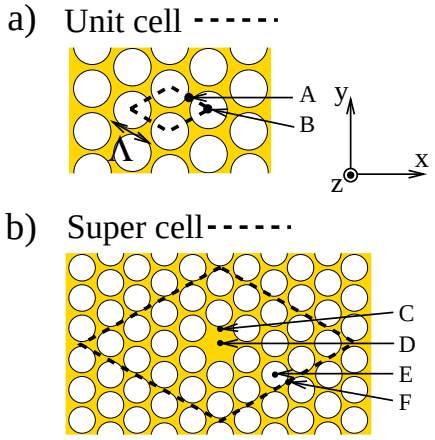

Figure 3.1: a) Photonic crystal with circular air-holes arranged on a triangular lattice in a dielectric background with dielectric constant 13. The volume fraction of the air-holes is 0.625. b) The same structure where a microcavity has been introduced by removing a single air-hole.

Fig. 3.1(a) shows a two-dimensional photonic crystal, where circular air-holes are arranged on a triangular lattice in a dielectric background with dielectric constant 13. The volume fraction of the air-holes is 0.625. The photonic crystal is characterized by a frequency interval, which will be referred to as an in-plane photonic bandgap, where propagation of electromagnetic waves in the xy-plane is forbidden. Fig. 3.1(b) shows a photonic crystal, where a defect has been introduced by removing a single air-hole in the otherwise periodic structure. This particular defect has the function of a microcavity, where a few electromagnetic modes are strongly localized.

A number of positions in Fig. 3.1 have been labelled *A*-*F*. In this chapter the rate of spontaneous emission will be considered for dipole emitters with random orientation located at these positions.

Previous work on spontaneous emission in two-dimensional photonic crystals, where position-dependence of the emitter was not taken into account, may be found in [42, 43]. For the case of free space the position-independent DOS is well known [44], and for a two-level atom in free space the rate of spontaneous emission may be simply related to the position-independent DOS. This is, however, not the case for an atom placed in e.g. a photonic crystal, where taking into account the position of the emitter is very important as the results of this chapter will show. Therefore, the position-dependent DOS is introduced, which is obtained from the position-independent DOS by weighting the contribution from each electromagnetic state by the position-dependent amplitude of the electric field squared. With this modification spontaneous emission can be simply related to the now position-dependent DOS. Previous theoretical calculations of the position-dependent DOS in photonic crystals may be found in [45, 46]. In general, the rate of spontaneous emission may depend significantly on the position of the emitter in any structure, where the dimensions are comparable to the emission wavelength in concern.

In order to evaluate the enhancement or suppression of spontaneous emission from an excited two-level system in a photonic crystal the position-dependent DOS must be compared to a proper reference. For the structures considered in this chapter consisting of a high-refractive-index material and air, we might assume that the active medium is placed in the high-refractive-index material region, and in that case a proper reference is the photon DOS in a homogeneous dielectric with the same dielectric constant as the high-refractive-index material. The first result for spontaneous emission rate alteration for a photonic crystal using this method may be found in [45]. For e.g. microcavity laser structures based on introducing a defect in a photonic crystal it is relevant to investigate and obtain an understanding of the spontaneous emission from emitters close to the defect. A model for spontaneous emission near defects in photonic crystals must take into account not only spontaneous emission into the cavity modes but also take into account spontaneous emission into a continuum of modes that are not localized to the cavity. Modeling the position-dependent DOS near defects in two-dimensional photonic crystals is a considerably more demanding numerical task compared to modeling photonic crystals. Therefore the calculations of the DOS presented in this chapter are based on a more powerful plane-wave-expansion method for large numerical problems [47, 48] compared to

the plane-wave-expansion method [49] used for calculating the DOS for photonic crystals in Ref. [46].

The chapter is organized in the following way. In Sec. 3.2 a model for spontaneous emission in passive microstructured dielectric media is presented, and it is shown how plane-wave-expansion theory can be used when the model is applied to periodic dielectric structures such as photonic crystals. In Sec. 3.3 an analysis is given for the DOS and spontaneous emission in the photonic crystal and photonic crystal microcavity shown in Fig. 3.1. Peaks in the DOS are related to a few strongly localized cavity modes. A conclusion is given in section 3.4.

3.2 Model for spontaneous emission in two-dimensional photonic crystal microcavities

In this section a model based on the Fermi Golden rule [50] is presented for the position-dependent rate of spontaneous emission for a two-level atom with random orientation. The atom is treated as an electric dipole with dipole operator μ, and it is assumed that the dipole is placed in a passive dielectric structure. The first-order interaction Hamiltonian for the interaction between the atom and the radiation field is in the space representation given by

$$H_I = -\mu \cdot \mathbf{E}, \tag{3.1}$$

where $\mathbf{E}$ is the transverse electric field operator. In general passive dielectric structures, the electric field operator may be expanded in a complete set of power-orthogonal transverse electromagnetic modes $\mathbf{e}(s, \mathbf{r})$ satisfying $\nabla \cdot (\varepsilon(\mathbf{r})\mathbf{e}(s, \mathbf{r})) = 0$, where the eigenfunctions denoted s are solutions to the complex Maxwell equations [51]. The function $\varepsilon(\mathbf{r})$ is the position-dependent dielectric constant of the structure under investigation.

In the Schrödinger picture, the electric field operator can be written

$$\mathbf{E}(\mathbf{r}) = -\frac{i}{\sqrt{2}} \sum_s [a_s - a_s{}^\dagger]\mathbf{e}(s, \mathbf{r}), \tag{3.2}$$

where a_s and $a_s{}^\dagger$ are the creation and annihilation operators for the modes s [50]. The angular frequency of mode s is denoted ω_s. The rate of spontaneous emission for an atom treated as an electric dipole depends on the modal field distributions $\mathbf{e}(s, \mathbf{r})$. The frequencies and position-dependence of these field distributions depend on the position-dependent dielectric constant distribution. Therefore we can expect from Eq. (3.1) and (3.2) that the

interaction Hamiltonian may be altered by modifying the dielectric constant distribution because this changes the properties of the radiation field.

By use of the normalization and orthogonality requirement

$$\int \varepsilon(\mathbf{r})\mathbf{e}(s,\mathbf{r})^* \cdot \mathbf{e}(s',\mathbf{r})d\mathbf{r} = \delta_{ss'}, \tag{3.3}$$

the strength of the vacuum field fluctuations of the transverse electric field is described by the function

$$\mathcal{E}(\omega,\mathbf{r}) = \sum_s \delta(\omega - \omega_s)\mathbf{e}(s,\mathbf{r})^* \cdot \mathbf{e}(s,\mathbf{r}) \ . \tag{3.4}$$

Here, $\sum$ in general represents a summation over discrete modes and an integration over a continuum of modes. However, for the two-dimensional structures considered in this chapter there are no true discrete modes, and consequently $\sum$ refers to an integration. The function $\mathcal{E}$ will be referred to as the position-dependent photon density of states.

For the passive dielectric structures and random dipole orientation considered here the rate of spontaneous emission can be related to the function $\mathcal{E}$. The approach used in this chapter is a special case of a more general approach. In chapter 4 more general structures with absorption or gain will be considered. In this case the rate of spontaneous emission from an electric dipole emitter can be written in the form

$$\Gamma = -\frac{2\mu_0{\omega_0}^2}{\hbar}\mathrm{Im}\left(\mu^\dagger \cdot \mathbf{G}_T(\mathbf{r}_0,\mathbf{r}_0;\Omega)\cdot\mu\right) \ , \tag{3.5}$$

where μ_0 is the vacuum permittivity, the dagger $\dagger$ refers to Hermitian conjugation, and $\mathbf{G}_T$ is the retarded Green's tensor for the transverse electric field. An expression similar to Eq. (3.5) has been used by Barnett et al. [52] for calculating the decay rate by an electric dipole emitter in a homogeneous absorbing dielectric. In the following chapter 4 a general method based on summation over a complete set of biorthogonal electromagnetic modes is presented for the construction of $\mathbf{G}_T$. An integral equation method for calculating elements of Green's tensors is presented in chapter 5.

In this chapter we will restrict ourselves to passive dielectric media, and we will also average the emission rate over all possible orientations for the transition dipole moment. In this case the expression (3.5) simplifies considerably from being proportional to elements of a complex Green's tensor to being proportional to the position-dependent DOS $\mathcal{E}$, i.e.

$$\Gamma = \frac{2\pi}{\hbar^2} \mid M \mid^2 \mathcal{E}(\Omega,\mathbf{r}) \ , \tag{3.6}$$

where M is the atomic matrix element or the dipole matrix element. An expression of the type Eq. (3.6) was introduced by Ching et al. [50, 53] for the rate of spontaneous emission in dielectric microspheres.

For a homogeneous dielectric, the function $\mathcal{E}(\omega, \mathbf{r})$ becomes parabolic in ω and independent of the position $\mathbf{r}$, i.e. $\mathcal{E}_{hom}(\omega) = \mathcal{E}(\omega, \mathbf{r})$. Consider a two-level atom located at position $\mathbf{r}$ in a homogeneous dielectric. By modifying the dielectric in a distance from the atom being large relative to the size of an atom, we expect $\mid M \mid^2$ to be unchanged. However, if this distance is not large relative to the emission wavelength of interest $\mathcal{E}(\omega, \mathbf{r})$ may change significantly. In this case, the change in the rate of spontaneous radiative decay for the atom due to the change in the dielectric $\varepsilon(\mathbf{r})$ is given by the ratio

$$\frac{\mathcal{E}(\Omega, \mathbf{r})}{\mathcal{E}_{hom}(\Omega)} \ . \tag{3.7}$$

The expression (3.7) can be applied to calculate spontaneous when an electric dipole emitter is placed in a wide range of passive dielectric microstructures. The expression can be evaluated by calculating the position-dependent DOS using Eq. (3.4). The summation in Eq. (3.4) is straightforward for a discrete set of electromagnetic modes. However, in this case there are a continuum of modes and the summation becomes an integration. This integration will be performed by taking advantage of the fact that in reciprocal space the density of modes is uniform.

The eigenfunctions $\mathbf{e}(s, \mathbf{r})$ are calculated using a numerical method based on plane-wave-expansion theory, effective-medium theory, and a variational principle [47, 48, 54, 55]. Methods based on plane-wave-expansion theory are convenient for periodic structures, i.e. structures characterized by discrete translational symmetries. The structures that will be considered in this chapter have discrete translational symmetry in the xy-plane. The photonic crystal without a defect is shown in Fig. 3.1(a). This structure is fully described by the unit cell shown in Fig. 3.1(a) by repeating the unit cell periodically on a triangular lattice. The photonic crystal with a microcavity introduced is not a periodic structure. However, this structure can be approximated by a periodic structure by use of a supercell approximation, i.e the structure is approximated with the discrete-translationally symmetric structure described by periodic repetition of the supercell shown in Fig. 3.1(b).

For passive dielectric media the magnetic-field wave equation

$$\nabla \times \left(\frac{1}{\varepsilon(\mathbf{r})} \nabla \times \mathbf{H}(\mathbf{r}) \right) = \frac{\omega^2}{c^2} \mathbf{H}(\mathbf{r}) \ , \tag{3.8}$$

may be treated as a Hermitian eigenvalue problem, where $\mathbf{H}$ represents the eigenvector and $\frac{\omega^2}{c^2}$ is the corresponding eigenvalue.

For the case of dielectric structures $\varepsilon(\mathbf{r})$ characterized by discrete translational symmetry, a complex magnetic field may, according to Bloch's theorem, be expanded in Bloch mode solutions in the form

$$\mathbf{H}_{\mathbf{k},n}(\mathbf{r}) = \mathbf{U}_{\mathbf{k},n}(\mathbf{r})e^{i\mathbf{k}\cdot\mathbf{r}} \quad , \tag{3.9}$$

where $\mathbf{U}_{\mathbf{k},n}$ is a function which is periodic with the same periodicity as the periodic dielectric structure, and $\mathbf{k}$ is a wave-number vector. The wave-number vector $\mathbf{k}$ is usually restricted to a region which will be referred to as the 1st Brillouin zone. For a given $\mathbf{k}$-vector there is an infinite number of discrete field solutions labelled with the band-index n.

The periodic function $\mathbf{U}_{\mathbf{k},n}$ is written as a Fourier expansion, and the magnetic-field solution becomes

$$\mathbf{H}_{\mathbf{k},n}(\mathbf{r}) = \sum_{\mathbf{G}} \sum_{\lambda=1,2} \mathbf{h}_{\mathbf{k},\mathbf{G},\lambda,n} e^{i(\mathbf{k}+\mathbf{G})\cdot\mathbf{r}} \quad , \tag{3.10}$$

where $\mathbf{G}$ is a reciprocal lattice vector. Transversality ($\nabla \cdot \mathbf{H} = 0$) is guaranteed by letting λ refer to the two field directions for $\mathbf{h}_{\mathbf{k},\mathbf{G},\lambda,n}$ that are perpendicular to $\mathbf{k}+\mathbf{G}$.

The eigenvalue corresponding to the eigenvector $\mathbf{H}_{\mathbf{k},n}$ is denoted $\frac{{\omega_{\mathbf{k},n}}^2}{c^2}$. The eigenfunctions (3.10) are found using a variational method based on minimization of the functional

$$E(\mathbf{H}) = \frac{\langle \nabla \times \left(\frac{1}{\varepsilon(\mathbf{r})}\nabla \times \mathbf{H}\right) \mid \mathbf{H} \rangle}{\langle \mathbf{H} \mid \mathbf{H} \rangle} \quad . \tag{3.11}$$

When this functional is at a minimum the argument $\mathbf{H}$ is an eigenvector, and $E(\mathbf{H})$ is the corresponding eigenvalue. By inserting a trial vector of the form (3.10) in (3.11), the functional effectively becomes a function of the coefficients $\mathbf{h}_{\mathbf{k},\mathbf{G},\lambda,n}$, and the problem is reduced to varying the coefficients along a path that minimizes the functional. An efficient iterative approach that performs this task is described in Ref. [54]. Higher-order solutions are found by use of the same minimization principle, where the trial-vectors are restricted to be orthogonal to all previously found eigenvectors. The calculation time is reduced by performing the rotations $\nabla\times$ in Fourier-space, and the operation $\frac{1}{\varepsilon(\mathbf{r})}$ in real-space. The Fast Fourier Transform (FFT) is used to go from one space to the other. Using this approach, however, interpolation of the dielectric function in real-space is necessary to achieve good

convergence. A method for interpolation based on effective medium theory [55] and a tensor representation of the dielectric constant is described in Refs. [47, 48]. The required computer memory scales linearly with the number of plane waves N used in the expansion (3.10), whereas the calculation time scales as $N\log(N)$. Therefore, relative to previous plane-wave methods [49], this approach offers a significant improvement for large numerical problems making accurate modeling of photonic crystals with defects feasible.

The electric field in translationally symmetric dielectric structures may in general be written in the form

$$\mathbf{E}(\mathbf{r},t) = \mathrm{Re}\left(\sum_{\mathbf{k},n} a_{\mathbf{k},n}\mathbf{E}_{\mathbf{k},n}(\mathbf{r})e^{i\omega_{\mathbf{k},n}t}\right) \quad , \tag{3.12}$$

where Re refers to the real part, and the complex field distribution $\mathbf{E}_{\mathbf{k},n}(\mathbf{r})$ represents the n'th complex eigensolution related to the wave-number-vector $\mathbf{k}$. These field distributions for the electric field are derived from the numerically calculated solutions for the magnetic field by use of the usual relation

$$\mathbf{E}_{\mathbf{k},n}(\mathbf{r}) = \frac{1}{i\omega_{\mathbf{k},n}\varepsilon(\mathbf{r})}\nabla\times\mathbf{H}_{\mathbf{k},n}(\mathbf{r}) \quad . \tag{3.13}$$

With the formulation (3.12), the position-dependent DOS (3.4) may be written

$$\mathcal{E}(\omega,\mathbf{r}) = \sum_{\mathbf{k},n}\delta(\omega-\omega_{\mathbf{k},n}) \mid \mathbf{E}_{\mathbf{k},n}(\mathbf{r}) \mid^2 \quad . \tag{3.14}$$

The usual position-independent DOS may, correspondingly, be written

$$\rho(\omega) = \sum_{\mathbf{k},n}\delta(\omega-\omega_{\mathbf{k},n}) \quad . \tag{3.15}$$

In-plane photonic bandgaps can be defined by use of the in-plane DOS, which correspond to Eq. (3.15), where only the $\mathbf{k}$-vectors with no component normal to the xy-plane are summed over, i.e. $k_z = 0$. Previous calculations of the position-independent in-plane DOS may be found in Ref. [56].

In Eq. (3.14) and (3.15) the in-plane component of $\mathbf{k}$ should be integrated over the 1st Brillouin zone, and the out-of-plane component of $\mathbf{k}$ should be integrated over an interval large enough to ensure that the frequency interval of interest is covered. The integration is performed numerically by sampling $\mathbf{k}$ at a large number of discrete equidistant points in reciprocal space. The DOS (3.15) is then obtained by counting the number of $\omega_{\mathbf{k},n}$

corresponding to the discrete values of $\mathbf{k}$ that fall within small frequency intervals. The position-dependent DOS (3.14) for a given position $\mathbf{r}$ is obtained by furthermore weighting the contribution from each state by the normalized amplitude of the electric field squared. The integration over $\mathbf{k}$ is straightforward because the density of $\mathbf{k}$-vectors is uniform.

The integration over the 1st Brillouin Zone in Eqs. (3.14) and (3.15) may be simplified significantly for dielectric structures characterized by various symmetries. In our case all field solutions may be derived from the field solutions related to 1/12 of the 1st Brillouin Zone, i.e. the irreducible 1st Brillouin Zone. Furthermore, the Fourier-coefficients in Eq. (3.10) may be restricted to be real due to the inversion symmetry of the considered structures.

3.3 Results and discussion

In this section numerical results will be given for the position-dependent photon DOS and the rate of spontaneous radiative decay for the photonic crystal and photonic crystal microcavity shown in Fig. 3.1. The properties of the radiation field in the photonic crystal with no microcavity introduced (see Fig. 3.1(a)) are summarized in Fig. 3.2.

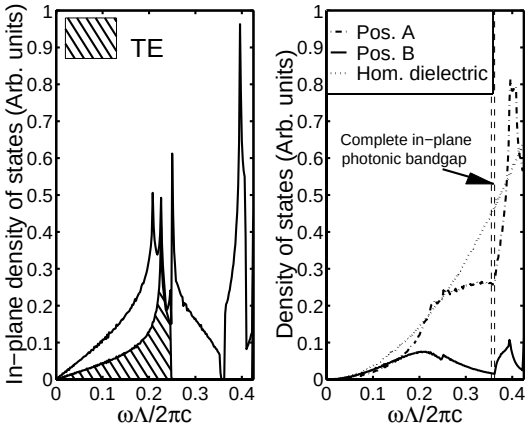

Figure 3.2: Density of states (DOS) for the photonic crystal shown in Fig. 3.1(a). Left: Position-independent in-plane DOS. Right: Position-dependent DOS for positions A (dash-dot line) and B (solid line). The DOS for a homogeneous dielectric with the same dielectric constant as the background material is shown with a dotted line. The edges of the complete in-plane photonic bandgap is shown with two dashed lines.

The in-plane DOS shown to the left in Fig. 3.2 illustrates the in-plane photonic bandgap properties of the photonic crystal. An in-plane photonic bandgap is defined as a frequency interval where the in-plane DOS is zero. Fig. 3.2 shows that in-plane propagating modes with TE polarization (magnetic field parallel to the z-axis) are not allowed within the frequency interval from $\omega\Lambda/2\pi c = \Lambda/\lambda = 0.25$ to 0.42, where ω is the angular frequency, Λ is the center-to-center hole spacing defined in Fig. 3.1(a), λ is the free-space wavelength, and c is the speed of light in vacuum. This frequency interval will be referred to as a TE bandgap. Fig. 3.2 also shows the complete in-plane DOS for the photonic crystal taking into account both TE and TM polarized modes. TM refers to modes with the electric field parallel to the z-axis. A TM bandgap exists from the frequency $\omega\Lambda/2\pi c = 0.355$ to 0.362. In fact, the frequency interval from $\omega\Lambda/2\pi c = 0.355$ to 0.362 represents a complete in-plane photonic bandgap since the TE bandgap and the TM bandgap overlap. The in-plane photonic bandgaps are important for understanding localization of electromagnetic modes to defects in the photonic crystal. TE (TM) polarized cavity modes in the photonic crystal microcavity shown in Fig. 3.1(b) must have a frequency within the corresponding TE (TM) photonic bandgap.

Along with the in-plane DOS, Fig. 3.2 shows the position-dependent DOS Eq. (3.14) mid between two air-holes (*Pos. A*) and in the center of an air-hole (*Pos. B*). The two positions A and B are shown in Fig. 3.1(a). Along with the position-dependent DOS for the photonic crystal, a similar calculation is shown for a homogeneous dielectric with the same dielectric constant as the photonic crystal background material. For an atom with transition frequency within the complete in-plane photonic bandgap, it is clear according to Eq. (3.7) that by taking the ratio between the curve for position A and the curve for a homogeneous dielectric, the rate of spontaneous emission mid between two air-holes is suppressed by 42% relative to the corresponding rate in the homogeneous dielectric. The suppression for other positions will be higher for this narrow range of frequencies. The position-dependent DOS in the center of an air-hole (*Pos. B*) is shown to illustrate, that the position-dependent DOS depends strongly on position. The DOS in Fig. 3.2 was calculated using 32x32 reciprocal lattice vectors $\mathbf{G}$ in Eq. (3.10). The position-dependent DOS Eq. (3.14) was calculated using app. 840000 reciprocal space points $\mathbf{k}$, whereas app. 130000 points were used for the in-plane DOS.

As a cavity is created in the photonic crystal by e.g. removing an air-hole in the periodic structure, electromagnetic modes may exist being localized to the cavity. These modes are interesting as lasing modes in future lasers

based on photonic crystals. Fig. 3.3 shows a banddiagram for TM-polarized modes related to the periodic structure defined by the supercell shown in Fig. 3.1(b). The diagram shows the allowed frequencies $\omega\Lambda/2\pi c$ as a func-

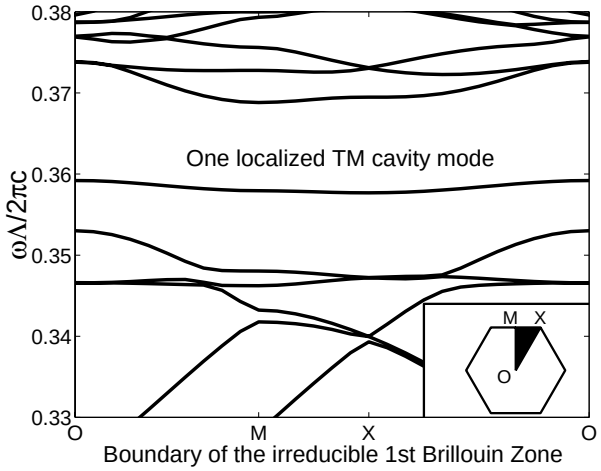

Figure 3.3: In-plane banddiagram of TM-polarized modes for the supercell shown in Fig. 3.1 taken over the boundary of the irreducible 1st Brillouin zone. The inset shows the 1st Brillouin zone, and the black region within this zone corresponds to the irreducible 1st Brillouin zone.

tion of the Bloch wave vector $\mathbf{k}$, where the Bloch wave vector is taken over the boundary of the irreducible 1st Brillouin zone. The inset shows the 1st Brillouin zone, and the black region within this zone corresponds to the irreducible 1st Brillouin zone. In the banddiagram one defect band exists within the complete in-plane photonic bandgap from $\omega\Lambda/2\pi c = 0.355$ to 0.362 for the photonic crystal with no microcavity introduced. This band corresponds to a non-degenerate TM polarized mode being localized to the photonic crystal microcavity. Note that due to the finite size of the supercell the upper edge of the bandgap is shifted towards higher frequencies. In the periodic approximation described by the supercell the microcavity is repeated periodically, and the distance between neighbouring microcavities is five photonic crystal lattice constants Λ. Due to the finite distance between neighbouring cavities we see a broadening of the defect band. This broadening is due to coupling between neighbouring cavities. As the distance between neighbouring cavities is increased the broadening of the defect band will eventually decrease to zero, and in this limit the defect band gives rise to a delta function peak in the position-dependent in-plane DOS for positions

where the field of the cavity mode is non-zero. However, for any finite distance between neighbouring cavities, i.e. any finite-size supercell, the defect band will be broadened.

The banddiagram in Fig. 3.3 was calculated for a zero out-of-plane component of $\mathbf{k}$, i.e. $k_z = 0$. However, as k_z is increased the bands will also increase in frequency [2,42,43,57], and a continuum of modes is formed. Consequently, a delta function peak will not appear in the DOS given by (3.14) and (3.15). Since the integration in (3.14) and (3.15) is over a continuum of modes the approach of dividing the frequency axis in small intervals and considering only a finite number of discrete vectors $\mathbf{k}$ is justified.

The amplitude of the electric field squared for the non-degenerate TM polarized cavity mode with normalized frequency $\omega'\Lambda/2\pi c \approx 0.36$ is shown in Fig. 3.4. The dash-dot lines represent the air-holes in the photonic crystal,

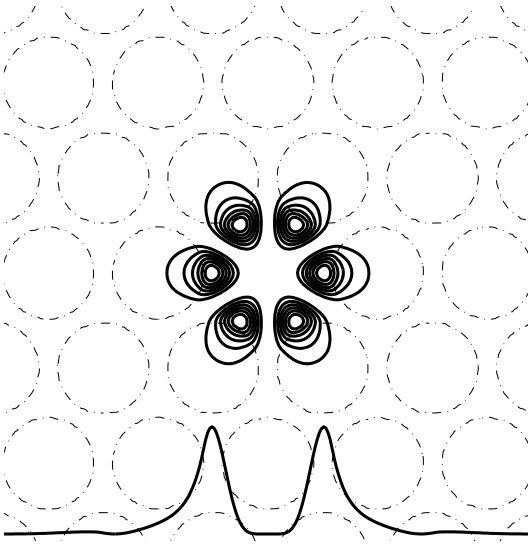

Figure 3.4: Amplitude of electric field squared for a non-degenerate TM polarized cavity mode with normalized frequency $\omega\Lambda/2\pi c = 0.36$.

whereas the solid curves in the region of the microcavity are contour lines of the amplitude of the electric field squared. Below the cavity is shown a horizontal cross section of the amplitude squared through the center of the cavity. Note that for TM polarization the electric field is parallel to the interfaces between the air-regions and the high-index material regions in the structure. Therefore the electric field is continuous across these interfaces. This does not have to be the case for TE polarized modes, where the electric field may have a component being perpendicular to the interface.

The amplitude of the TM polarized mode is high at position C and low at position D. Therefore, for the frequency $\omega'\Lambda/2\pi c = 0.36$ a strong peak is expected in the position-dependent DOS (3.14) at position C, whereas a peak is not expected at position D. The peak at position C is expected to start abruptly at the frequency $\omega'\Lambda/2\pi c = 0.36$, and is expected to roll off roughly as $1/\sqrt{(\omega^2 - \omega'^2)}$ as was the case for a metallic wire waveguide in [58]. This behaviour is similar to the behaviour of the electronic density of states in an electronic quantum wire. In fact we may think of two-dimensional photonic crystal microcavities as the optical analogue to electronic quantum wires. Due to the broadening of the defect band the calculated photon DOS obtained by use of a finite-sized supercell is not expected to be singular at the frequency $\omega'\Lambda/2\pi c = 0.36$. However, if the size of the supercell is increased towards infinity, the calculated DOS at this frequency may eventually become singular.

A banddiagram for the TE polarized modes related to the periodic structure defined by the supercell shown in Fig. 3.1(b) is shown in Fig. 3.5. In

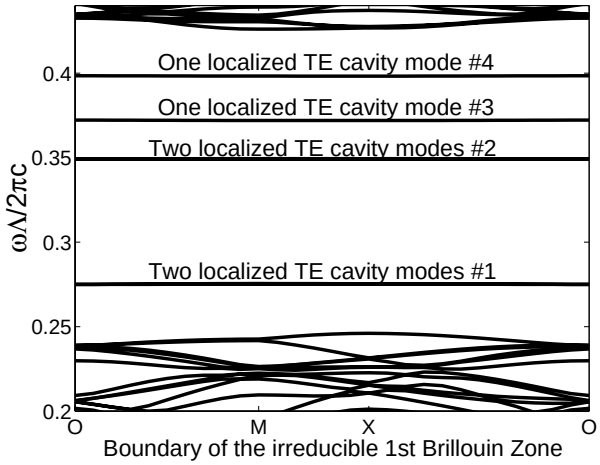

Figure 3.5: In-plane banddiagram of TE-polarized modes for the supercell shown in Fig. 3.1.

this case we find two degenerate bands at the frequency $\omega\Lambda/2\pi c = 0.27$. Two degenerate bands are also found at the frequency $\omega\Lambda/2\pi c = 0.35$, and nondegenerate bands are found at the frequencies $\omega\Lambda/2\pi c = 0.37$ and $\omega\Lambda/2\pi c = 0.40$. These defect bands are all within the TE bandgap and correspond to TE polarized modes being localized to the two-dimensional microcavity. Although these bands appear to be flat they are in fact slightly broadened due to the finite size of the supercell.

The two bands at the frequency $\omega\Lambda/2\pi c = 0.27$ correspond to two degenerate orthogonal cavity modes. There are, however, many possible ways of choosing the two orthogonal TE modes. Other choices of modes may be obtained by making linear combinations of the two modes. In general, the amplitude of the electric field squared for one of these two modes does not exhibit 60° rotational symmetry about the center of the microcavity. However, if the two orthogonal degenerate modes are normalized to unity energy within the supercell, then the sum of the electric field squared for the two modes does not depend on how these modes were chosen. From symmetry considerations the sum must exhibit 60° rotational symmetry about the center of the microcavity. Furthermore, according to Eq. (3.4) it is indeed the sum of the amplitudes of the electric field squared which is the relevant parameter in a calculation of the position-dependent DOS. The amplitude of the electric field squared is shown for one possible choice of two orthogonal degenerate modes denoted #1a and #1b in Fig. 3.6. Also shown is the more important sum of the amplitudes of the electric field squared for the two modes. The summation of the intensities peaks in the center of the

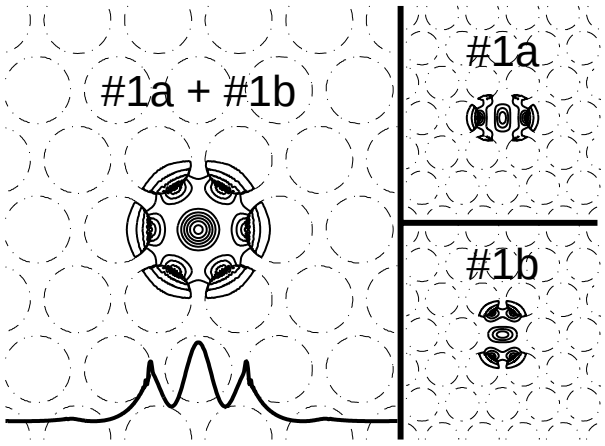

Figure 3.6: Amplitude of the electric field squared for one possible choice for two orthogonal degenerate TE polarized cavity modes #1a and #1b with normalized frequency $\omega\Lambda/2\pi c = 0.27$. Also shown is the sum of the amplitudes squared for the two modes.

microcavity (position D in Fig. 3.1(b)). The intensity is also high near the air-holes surrounding the microcavity (position C in Fig. 3.1(b)). Therefore, for the frequency $\omega\Lambda/2\pi c = 0.27$ a high peak is expected at position D for the position-dependent DOS, and a smaller peak is expected at position C.

Fig. 3.7 shows the amplitude of the electric field squared for the other TE polarized cavity modes denoted #2, #3 and #4 in the banddiagram. For the two degenerate modes denoted #2 only the sum of the amplitudes squared is shown. We should note that the frequency of the TE polarized cavity

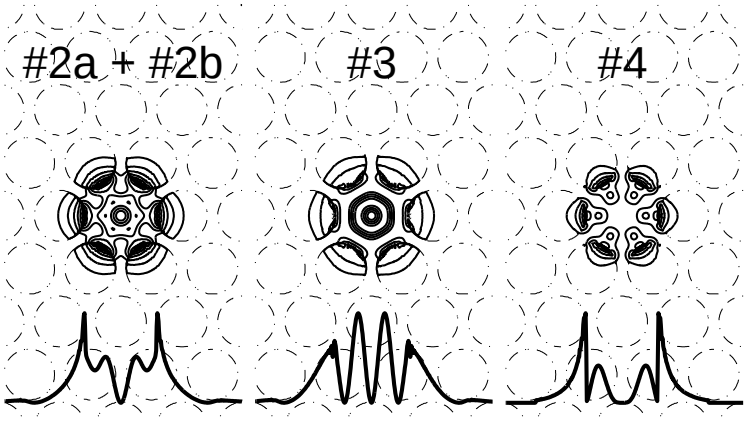

Figure 3.7: Left: The sum of the amplitudes of the electric field squared for two orthogonal, degenerate and normalized TE polarized cavity modes #2a and #2b with normalized frequency $\omega\Lambda/2\pi c = 0.35$. Middle: Amplitude of the electric field squared for a TE polarized cavity mode #3 with frequency $\omega\Lambda/2\pi c = 0.37$. Right: Amplitude of the electric field squared for a TE polarized cavity mode #4 with frequency $\omega\Lambda/2\pi c = 0.40$.

modes #2 ($\omega\Lambda/2\pi c = 0.35$) is close to the frequency of the TM polarized cavity mode ($\omega\Lambda/2\pi c = 0.36$).

In Fig. 3.8, we have shown the position-dependent DOS for the four positions labelled C, D, E and F in Fig. 3.1(b). The number of eigenvectors $\mathbf{E}_{\mathbf{k},n}$ used for calculating Fig. 3.8 is equivalent to the number of eigenvectors used for calculating Fig. 3.2. The number of Bloch wave vectors used for calculating Fig. 3.8 is smaller compared to the calculation of Fig. 3.2 due to the smaller Brillouin zone for a larger structure. However, the number of discrete bands used for a given reciprocal lattice vector is correspondingly higher compared to what was used for calculating Fig. 3.2. For the calculation of Fig. 3.8 the number of reciprocal lattice vectors $\mathbf{G}$ used in Eq. (3.10) was 128x128.

The two positions E and F in Fig. 3.1(b) are similar to the positions A and B in Fig. 3.1(a) in the sense that A and F are both located mid between two air-holes, whereas B and E are both located in the center of an air-hole. By comparison between positions E and F in Fig. 3.8 and positions A and

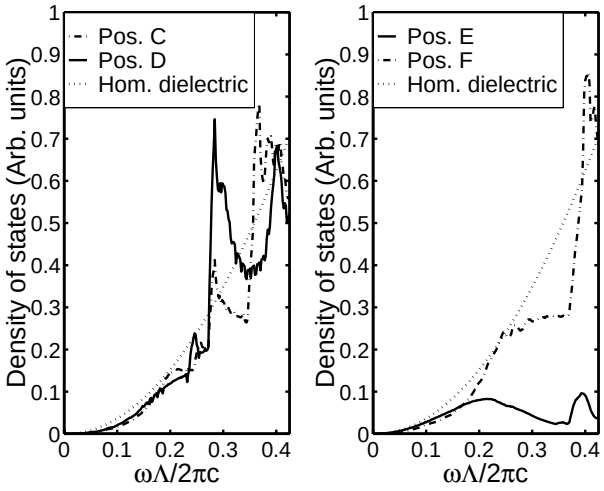

Figure 3.8: Position-dependent density of states for four positions C, D, E and F in the structure shown in Fig. 3.1(b).

B in Fig. 3.2, it is clear that the DOS in the two cases differs only slightly. As a conclusion, the position-dependent DOS and the rate of spontaneous radiative decay, in a distance of a few photonic crystal lattice constants Λ from the defect, appears to be only weakly affected by the presence of the defect. This is the case except when a transition frequency is considered where a small shift of the DOS frequency spectrum will have a large effect. For example the upper bandgap edge may be shifted to higher frequencies due to the microcavity, and consequently for transition frequencies near the upper bandgap edge a small shift can have a large effect on the position-dependent DOS.

For a photonic crystal microcavity laser the active medium must be placed in such a way that it interacts with a cavity mode. Therefore it is recommended that the active medium is placed at the positions where the intensity of the relevant cavity mode is high. Two relevant positions for the TE polarized cavity modes shown in Fig. 3.6 are the positions C and D, whereas position C is relevant for the TM polarized cavity mode shown in Fig. 3.4.

The position-dependent DOS at the positions C and D is shown to the left in Fig. 3.8. A clear peak is seen in the DOS at position D (center of the cavity) for the frequency $\omega\Lambda/2\pi c = 0.27$, whereas a smaller peak is seen at position C (near the edge of the cavity). This is in agreement with the intensity profiles of the TE polarized modes shown in Fig. 3.6.

The peak at position C near the frequencies $\omega\Lambda/2\pi c = 0.35$ and $\omega\Lambda/2\pi c = 0.36$ may in a similar way be related to the TE polarized cavity modes #2 and the TM polarized cavity mode. Two peaks could have been expected. However, if the first peak rolls off slowly and is broadened, then the result is that only one peak is seen.

For the frequency $\omega\Lambda/2\pi c = 0.4$ another peak is seen in the DOS at position D. Even though a TE polarized cavity mode (#4) exists at this frequency, the amplitude of the electric field squared for this mode is practically zero at position D. The peaks related to cavity modes are characterized by a steep edge at the frequency of the cavity modes. This steep edge is seen for the frequencies 0.27 (TE polarized cavity modes #1) and 0.36 (TM polarized cavity mode). A steep edge is, however, not seen for the peak at the frequency 0.4 at position D, and this peak cannot be related to a cavity mode. Similarly, the TE polarized cavity mode (#3) with frequency 0.37 does not give rise to a peak at position D at this frequency. However, a small peak is seen at position C for this frequency.

By comparison with the DOS for a homogeneous dielectric, it is clear that the rate of spontaneous radiative decay may be enhanced relative to a homogeneous dielectric due to the cavity modes. For the case of a narrow linewidth atomic source with transition frequency Ω at position $\mathbf{r}$ the spontaneous emission factor β, i.e. the fraction of the total spontaneous emission going into a cavity mode $\mathbf{E}_{cav}(\omega, \mathbf{r})$, is given by

$$\beta(\Omega, \mathbf{r}) = \frac{\mid \mathbf{E}_{cav}(\Omega, \mathbf{r}) \mid^2}{\mathcal{E}(\Omega, \mathbf{r})} \quad . \tag{3.16}$$

This expression for β is similar to Eq. (3) in Ref. [59]. For a given atomic transition frequency Ω, the denominator in the expression for β at positions C and D may be obtained from Fig. 3.8. For the frequency $\omega\Lambda/2\pi c = 0.27$ the nominator is then the contribution to the DOS from the TE polarized cavity modes #1. This contribution is identified as the steep edge at this frequency. For an atom at position D with transition frequency $\omega\Lambda/2\pi c = 0.27$ this leads to a conservative estimate of $\beta \approx 70\%$. The estimated spontaneous emission factor may increase as the distance between neighbouring cavities, i.e. the size of the supercell, increases. This is expected since the broadening of the defect bands decreases as the size of the supercell increases.

By use of the same approach for an atom at position C with transition frequency 0.36 we would expect a large fraction of the spontaneous emission to go into the TM polarized cavity mode shown in Fig. 3.4. However, another large fraction of the emission may also go into modes being similar to the

TE polarized cavity modes #2 with a non-zero out-of-plane component of the wave vector $\mathbf{k}$.

3.4 Conclusion

In conclusion, a model based on the Fermi Golden Rule for spontaneous emission in microstructured passive dielectric media has been applied to a two-dimensional photonic crystal and photonic crystal microcavity.

It was shown that spontaneous emission may be suppressed by at least 42% for an electric dipole with random orientation in a two-dimensional photonic crystal.

By comparing the position-dependent photon density of states (DOS) at two positions within the photonic crystal, it was clear that the strength of the electric field vacuum fluctuations depends strongly on position. Furthermore, the rate of spontaneous emission in the photonic crystal is, except for a frequency shift, practically unaffected by the presence of a defect or a microcavity being only a few photonic crystal lattice constants away from the emitter. Strong peaks in the position-dependent DOS at two positions within a photonic crystal microcavity have been related to a few strongly localized cavity modes. The rate of spontaneous radiative decay for a narrow linewidth two-level atom inside the photonic crystal microcavity interacting with cavity modes may be significantly enhanced. However, in this case a large fraction of the spontaneous emission, at least 70%, may go into the cavity modes.

Chapter 4

General theory for spontaneous emission in active dielectric microstructures: Example of a fiber amplifier

4.1 Introduction

The standard approach to calculation of the rate of spontaneous emission for an atom placed in an empty metallic cavity or in free space is to expand the radiation field in power orthogonal modes normalized to one quantum of energy and use the Fermi golden rule. If the emitter is embedded in a dielectric material, the coupling between matter and radiation field requires a quantum electrodynamics (QED) formulation of Maxwells equations for the dielectric medium in order to calculate the rate of spontaneous emission from the emitter. For passive media without gain or absorption it is possible, as in free space, to expand the radiation field in power orthogonal modes and to use the expansion as a basis for quantization. This is the method that was applied to passive photonic crystals in chapter 3.

If the material is active and has loss and/or gain, the solutions to Maxwells equations cannot be expanded in power orthogonal modes and the concept of modes becomes more subtle. In that case it is convenient to use the electromagnetic fields and generating currents as primary ob-

servables represented by operators that are defined by their commutation relations. The relation between field and current operators is given by a classical electric field Green's tensor. This allows a calculation of spontaneous emission even for extended and dynamically varying structures as for example a modulated laser diode. The studies of QED for dielectric materials have essentially followed two parallel approaches in the physics and the quantum electronics communities, respectively. The physics approach [60–73] has focussed on the material aspects of QED for dielectrics such as the influence of absorption, dispersion and inhomogeneities.

The quantum electronics approach, (see for example the papers [74–85] and references in [80]), has been driven by studies of spontaneous emission in optical waveguides and has explored the effect of the absence of a complete set of power orthogonal modes. In fact, the phenomenon of excess noise in guided modes introduced by Petermann [74] is, as pointed out first by Haus and Kawakami [75], related to the non-existence of a complete set of power orthogonal electromagnetic modes. The analyses of spontaneous emission in active dielectric waveguides in Refs. [74–85] are based on the scalar wave equation for the electromagnetic field. The scalar methods give the rate of spontaneous emission into guided modes, but they do not give the total rate of spontaneous emission. This requires taking into account the coupling to the complete radiation field and not only the guided modes.

In this chapter we extend the analysis of spontaneous emission based on the approximate scalar wave equation to a full vectorial approach valid for general active dielectric microstructures. The total rate of spontaneous emission from an emitter in an active dielectric medium can be expressed in terms of the classical Green's tensor, or to be more precise, the double-transverse part of the tensor. We present a general method for calculating this tensor from complete sets of biorthogonal modes for the vector wave equation. The vectorial nature of the formalism allows calculation of spontaneous emission depending on position, transition frequency and polarization of the emitter in a dielectric microstructure with loss or gain. Vectorial Green's tensor methods for decay of excited molecules have previously been given for the case of homogeneous absorbing dielectric media [68], for an absorbing dielectric surface [71], and in a series of papers by Tomaŝ for absorbing layered structures [86–88].

We exemplify the method by analyzing spontaneous emission in an optical fiber. The step-index fiber is sufficiently simple to allow analytical solutions for the Green's function for both passive and active fibers; the solutions illustrate some subtle issues related to the singularity of the Green's function that are not easily studied by purely numerical methods. We take

into account both position and vector orientation of spatially localized generating currents. Our method allows taking into account spontaneous emission into the radiation modes of the electromagnetic field, and thereby the total rate of spontaneous emission from an emitter embedded in for example an active waveguide may be calculated. Spontaneous emission into radiation modes has previously been considered for passive multilayer dielectric structures [31, 89–92], and decay in the presence of passive dielectric cylindrical structures has been investigated in [93–95]. In the analysis of active fibers the Green's tensor is calculated exemplifying the general formalism for calculating Green's tensors for the vector case. Another example of calculating Green's tensors for active layered structures is given in Ref. [86].

The chapter is organized in the following way. In Sec. 4.2 the model for spontaneous emission in active dielectric microstructures is given. The general principle for obtaining the electric field Green's tensor is given in Sec. 4.3. Using this principle the transverse electric field Green's tensor is derived for the case of active optical fibers in Sec. 4.4. Position-dependence and transition-frequency dependence of spontaneous emission for the passive fiber is given in Sec. 4.5. Radiation patterns obtained using a Poynting vector approach for the active fiber are presented in Sec. 4.6. The conclusion is given in Sec. 4.7.

4.2 Model for spontaneous emission

In this section we present a general Green's tensor model for calculating the rate of spontaneous emission in a material with position dependent dielectric constant $\varepsilon(\mathbf{r})$. The model allows ε to be complex and thus to represent materials with absorption or gain. For simplicity, we treat $\varepsilon(\mathbf{r})$ as a scalar. There is no problem in principle to let $\varepsilon(\mathbf{r})$ represent a tensor, and thus to include the case of birefringent materials, but the notation will of course be less transparent.

The spontaneous emission in the material may be considered as being generated by a distribution of spontaneous currents. The positive frequency part of the current density is represented by an operator $\widehat{\mathbf{j}}(\mathbf{r}, t)$ in the Heisenberg picture. The real current density is therefore $\widehat{\mathbf{j}} + \widehat{\mathbf{j}}^{\dagger}$, where $(\dagger)$ denotes Hermitian conjugation, and where

$$\widehat{\mathbf{j}}(\mathbf{r}, t) = \frac{1}{2\pi} \int_0^{\infty} \widehat{\mathbf{j}}(\mathbf{r}; \omega) e^{-i\omega t} d\omega \,, \tag{4.1}$$

the integration being only over positive angular frequencies ω.

The current density is the sum of two parts $\widehat{\mathbf{j}}_T(\mathbf{r},t)$ and $\widehat{\mathbf{j}}_{GL}(\mathbf{r},t)$ with $\nabla\cdot\widehat{\mathbf{j}}_T=0$ and $\nabla\times(\widehat{\mathbf{j}}_{GL}/\varepsilon)=\mathbf{0}$ [96]. It is actually only the transverse part of the currents $\widehat{\mathbf{j}}_T(\mathbf{r},t)$ which contributes to spontaneous emission; the part $\widehat{\mathbf{j}}_{GL}(\mathbf{r},t)$ contributes to the non-radiative decay rate [68]. For a homogeneous medium with constant ε the component $\widehat{\mathbf{j}}_{GL}$ is simply the longitudinal part, but for non-homogeneous media $\widehat{\mathbf{j}}_{GL}$ is the generalized longitudinal part. Notice, that in splitting the current into $\widehat{\mathbf{j}}_T$ and $\widehat{\mathbf{j}}_{GL}$ the transverse part is also affected by ε, when this is non-uniform.

The average rate of energy dissipation due to spontaneous emission is given in terms of the currents $\widehat{\mathbf{j}}_T$ by

$$\langle P\rangle=-\int\langle\ \widehat{\mathbf{j}}_T^{\dagger}(\mathbf{r},t)\cdot\widehat{\mathbf{E}}(\mathbf{r},t)+\widehat{\mathbf{E}}^{\dagger}(\mathbf{r},t)\cdot\widehat{\mathbf{j}}_T(\mathbf{r},t)\rangle d^3r, \tag{4.2}$$

where the angled brackets $\langle\cdots\rangle$ denote ensemble and time averaging, and $\widehat{\mathbf{E}}(\mathbf{r},t)$ is the positive frequency part of the electric field operator. The field is itself generated by the transverse currents and satisfies the inhomogeneous wave equation

$$\Big(-\nabla\times\nabla\times+k_0^2\,\varepsilon(\mathbf{r})\Big)\,\widehat{\mathbf{E}}(\mathbf{r};\omega)=-i\omega\mu_0\,\widehat{\mathbf{j}}_T(\mathbf{r};\omega) \tag{4.3}$$

in the frequency domain. Here $k_0=\omega/c$ is the wavenumber, c is the speed of light, and μ_0 is the permeability, all for vacuum. The solution to (4.3) may be written as

$$\widehat{\mathbf{E}}(\mathbf{r};\omega)=-i\omega\mu_0\int\mathbf{G}(\mathbf{r},\mathbf{r}';\omega)\cdot\widehat{\mathbf{j}}_T(\mathbf{r}';\omega)d^3r' \tag{4.4}$$

in terms of the classical Green's tensor $\mathbf{G}(\mathbf{r},\mathbf{r}';\omega)$. It is defined as a solution to the equation

$$\Big(-\nabla\times\nabla\times+k_0^2\,\varepsilon(\mathbf{r})\Big)\,\mathbf{G}(\mathbf{r},\mathbf{r}';\omega)=\mathbf{I}\,\delta(\mathbf{r}-\mathbf{r}'), \tag{4.5}$$

where δ is the Dirac delta function, and $\mathbf{I}$ is the unit 3×3 tensor. We shall only deal with the retarded Green's tensor, $\lim_{\epsilon\to0+}\mathbf{G}(\mathbf{r},\mathbf{r}';\omega+i\epsilon)$, which ensures a causal relationship between $\widehat{\mathbf{E}}(\mathbf{r},t)$ and $\widehat{\mathbf{j}}_T(\mathbf{r},t)$.

Insertion of (4.4) in (4.2) leads to

$$\begin{aligned}\langle P\rangle\ =\ &-\frac{i\mu_0}{(2\pi)^2}\int\langle\ \widehat{\mathbf{j}}_T^{\dagger}(\mathbf{r};\omega)\cdot\{\omega'\mathbf{G}(\mathbf{r},\mathbf{r}';\omega')-\\ &\omega\mathbf{G}^{\dagger}(\mathbf{r}',\mathbf{r};\omega)\}\cdot\widehat{\mathbf{j}}_T(\mathbf{r}';\omega')\rangle d^3r\,d^3r'\,d\omega\,d\omega'\,.\end{aligned} \tag{4.6}$$

It is convenient to drop the restriction that the currents have to be transverse by instead using the double-transverse Green's tensor $\mathbf{G}_T$ defined by

$$\mathbf{G}_T(\mathbf{r},\mathbf{r}';\omega) = \int \delta_T^\dagger(\mathbf{r},\mathbf{r}_1)\cdot\mathbf{G}(\mathbf{r}_1,\mathbf{r}_2;\omega)\cdot\delta_T(\mathbf{r}_2,\mathbf{r}')d^3r_1 d^3r_2\,. \tag{4.7}$$

The transverse delta-function $\delta_T(\mathbf{r},\mathbf{r}')$ is the operator which projects an arbitrary vector function into its transverse part [62, 97]. The construction of δ_T is presented in Appendix B.

The spontaneous currents are assumed to be δ-correlated in space and frequency, i.e.

$$\langle\, \widehat{j}_l^\dagger(\mathbf{r};\omega)\widehat{j}_m(\mathbf{r}';\omega')\rangle = 2D_{ml}(\mathbf{r};\omega)\delta(\mathbf{r}-\mathbf{r}')2\pi\delta(\omega-\omega'), \tag{4.8}$$

where $\widehat{j}_l$ is the l-th component of the current density $\widehat{\mathbf{j}}$, and D_{ml} is the element ml of the diffusion tensor $\mathbf{D}$. The optical transitions that contribute to the spontaneous emission, and therefore to the diffusion tensor, will also give a contribution ε_{sp} to the dielectric tensor. The two tensors are related by the fluctuation-dissipation theorem [80]

$$\mathbf{D} = \hbar\omega^2\varepsilon_0 n_{sp}\mathrm{Im}(\varepsilon_{sp}), \tag{4.9}$$

i.e. the diffusion tensor is proportional to the imaginary part of ε_{sp}. The factor n_{sp} is the population inversion factor for the involved quantum states, and ε_0 is the vacuum permittivity.

The rate of spontaneous emission Γ, i.e. the number of spontaneously emitted photons per unit time, can now be obtained from the rate of energy dissipation by introducing (4.8) in (4.6) and dividing the integrand by the photon energy $\hbar\omega$. This results in the following simple expression for Γ:

$$\Gamma = -\frac{2\mu_0}{\hbar 2\pi}\mathrm{Im}\left(\int Tr\{2\mathbf{D}(\mathbf{r};\omega)\cdot\mathbf{G}_T(\mathbf{r},\mathbf{r};\omega)\}d^3r d\omega\right), \tag{4.10}$$

where "Tr" indicates the trace of the matrix product. We will focus on the case where a dipole emitter is localized at $\mathbf{r}_0$, and the transition frequency is ω_0. The diffusion tensor is then given by

$$2\mathbf{D} = {\omega_0}^2\mu\mu^\dagger\delta(\mathbf{r}-\mathbf{r}_0)2\pi\delta(\omega-\omega_0)\,, \tag{4.11}$$

where μ is the dipole vector, and the rate of spontaneous emission becomes [68]

$$\Gamma = -\frac{2\mu_0{\omega_0}^2}{\hbar}\mathrm{Im}(\mu^\dagger\cdot\mathbf{G}_T(\mathbf{r}_0,\mathbf{r}_0;\omega_0)\cdot\mu). \tag{4.12}$$

The expression (4.12) allows us to calculate the rate of spontaneous emission from dipoles even if the dielectric material is a gain medium at the transition frequency ω_0. In that case, the radiation observed outside the material consists of amplified spontaneous emission from the dipole as well as amplified spontaneous emission from the gain medium, and the spontaneous emission rate Γ cannot be determined by simply counting the emitted photons. However, if the dipole radiation is due to different processes than the processes that provide the gain, it may nevertheless be possible to verify the expression (4.12) experimentally. In the following we present a theoretical method for calculating Γ, and we demonstrate the method for the example of an optical fiber.

4.3 Construction of the electric field transverse Green's tensor

This section concerns the general principles for construction of the electric field Green's tensor $\mathbf{G}(\mathbf{r}, \mathbf{r}'; \omega)$ defined by Eq. (4.5). Instead of dealing with the wave equation in the form (4.3), it is convenient to introduce the vector function [62]

$$\mathbf{g}(\mathbf{r}) = \sqrt{\varepsilon(\mathbf{r})}\mathbf{E}(\mathbf{r}), \tag{4.13}$$

and to rewrite the wave equation (4.3) in terms of $\mathbf{g}(\mathbf{r})$:

$$-\frac{1}{\sqrt{\varepsilon(\mathbf{r})}}\nabla \times \nabla \times \frac{\mathbf{g}(\mathbf{r})}{\sqrt{\varepsilon(\mathbf{r})}} + k_0^2 \mathbf{g}(\mathbf{r}) = -i\omega\mu_0 \frac{\mathbf{j}_T(\mathbf{r})}{\sqrt{\varepsilon(\mathbf{r})}} \; . \tag{4.14}$$

The argument ω has been suppressed for simplicity. We will first derive the Green's tensor $\mathbf{G}_g(\mathbf{r}, \mathbf{r}')$ for $\mathbf{g}(\mathbf{r})$; by (4.13) the Green's tensor $\mathbf{G}(\mathbf{r}, \mathbf{r}')$ for the electric field is then obtained from the relation

$$\mathbf{G}_g(\mathbf{r}, \mathbf{r}') = \sqrt{\varepsilon(\mathbf{r})}\mathbf{G}(\mathbf{r}, \mathbf{r}')\sqrt{\varepsilon(\mathbf{r}')} \; . \tag{4.15}$$

We define an operator $\mathcal{H}$ acting on $\mathbf{g}(\mathbf{r})$ by writing the left-hand side of (4.14) as $\mathcal{H}\mathbf{g}$. The equation for the Green's tensor $\mathbf{G}_g(\mathbf{r}, \mathbf{r}')$ may then be written as

$$\mathcal{H}\mathbf{G}_g(\mathbf{r}, \mathbf{r}') = \mathbf{I}\,\delta(\mathbf{r} - \mathbf{r}') \; . \tag{4.16}$$

The operator $\mathcal{H}$ was introduced by Glauber and Lewenstein in their theory of quantum electrodynamics of dielectric media [62]. For passive dielectric media with real $\varepsilon(\mathbf{r})$ the operator is Hermitian, but it is non-Hermitian if $\varepsilon(\mathbf{r})$ is complex. The Hermitian conjugate $\mathcal{H}^\dagger$ is obtained from $\mathcal{H}$ by replacing

$\varepsilon(\mathbf{r})$ by its complex conjugate. In both cases we can assume, that for each set $(\mathbf{g}_n, \lambda_n)$ of eigensolutions to $\mathcal{H}\mathbf{g}_n = \lambda_n \mathbf{g}_n$, there exists a set of eigensolutions $(\widetilde{\mathbf{g}}_n, \lambda_n^*)$ to $\mathcal{H}^\dagger \widetilde{\mathbf{g}}_n = \lambda_n^* \widetilde{\mathbf{g}}_n$ such that the biorthogonality condition

$$\int (\widetilde{\mathbf{g}}_n(\mathbf{r}))^* \cdot \mathbf{g}_m(\mathbf{r}) d^3r = N_n \delta_{nm} \tag{4.17}$$

and the completeness relation

$$\sum_n \frac{\mathbf{g}_n(\mathbf{r}) \widetilde{\mathbf{g}}_n^*(\mathbf{r}')}{N_n} = \mathbf{I}\, \delta(\mathbf{r} - \mathbf{r}') \tag{4.18}$$

are satified. Here, the asterisk (*) denotes complex conjugation. The eigenfunction $\widetilde{\mathbf{g}}_n(\mathbf{r})$ is denoted the adjoint of $\mathbf{g}_n(\mathbf{r})$. The eigensolutions $\mathbf{g}_n$ are degenerate, so the assignment of the adjoint solution is not unique, but it can be chosen such that (4.17) and (4.18) are fulfilled. The actual choice may be adapted to the specific structure under consideration, as we will demonstrate for the example of an optical fiber. The summation sign in (4.18) represents an integration for the case of a continuum of eigensolutions and a summation for discrete eigensolutions. Similarly, the symbol δ_{nm} in (4.17) represents a Dirac delta-function for eigensolutions in the continuous spectrum of eigenvalues, and a Kronecker delta-function for discrete eigensolutions.

By the completeness relation (4.18) the Green's tensor $\mathbf{G}_g(\mathbf{r}, \mathbf{r}')$ becomes

$$\mathbf{G}_g(\mathbf{r}, \mathbf{r}') = \sum_n \frac{\mathbf{g}_n(\mathbf{r}) \widetilde{\mathbf{g}}_n^*(\mathbf{r}')}{N_n \lambda_n}, \tag{4.19}$$

as can be seen by inserting (4.19) in (4.16). Equation (4.15) finally leads to the expression

$$\mathbf{G}(\mathbf{r}, \mathbf{r}'; \omega) = \sum_n \frac{\mathbf{E}_n(\mathbf{r}) (\widetilde{\mathbf{E}}_n(\mathbf{r}'))^*}{N_n \lambda_n} \tag{4.20}$$

for the Green's tensor for the electric field. The electric field $\mathbf{E}_n = \mathbf{g}_n / \sqrt{\varepsilon}$ is a solution to

$$-\nabla \times \nabla \times \mathbf{E}_n + k_0^2\, \varepsilon(\mathbf{r}) \mathbf{E}_n = \lambda_n \varepsilon(\mathbf{r}) \mathbf{E}_n, \tag{4.21}$$

and $\widetilde{\mathbf{E}}_n = \widetilde{\mathbf{g}}_n / \sqrt{\varepsilon^*}$. The normalization factor N_n is

$$\begin{aligned} N_n &= \int (\widetilde{\mathbf{g}}_n(\mathbf{r}))^* \cdot \mathbf{g}_n(\mathbf{r}) d^3r \\ &= \int \varepsilon(\mathbf{r}) (\widetilde{\mathbf{E}}_n(\mathbf{r}))^* \cdot \mathbf{E}_n(\mathbf{r}) d^3r \ . \end{aligned} \tag{4.22}$$

The solutions to (4.21) must satisfy the equation

$$k_0^2 \ \nabla \cdot (\varepsilon(\mathbf{r})\mathbf{E}_n(\mathbf{r})) = \lambda_n \ \nabla \cdot (\varepsilon(\mathbf{r})\mathbf{E}_n(\mathbf{r})), \tag{4.23}$$

so we have either

$$\nabla \cdot (\varepsilon(\mathbf{r})\mathbf{E}_n(\mathbf{r})) = 0, \tag{4.24}$$

which describes field solutions in the absence of electric charges, or else $\nabla \cdot (\varepsilon(\mathbf{r})\mathbf{E}_n(\mathbf{r})) \neq 0$, and hence $\lambda_n = k_0^2$. In the latter case, the eigenvalue problem reduces to

$$\nabla \times \nabla \times \mathbf{E}_n(\mathbf{r}) = \mathbf{0}, \tag{4.25}$$

which has solutions of the form

$$\mathbf{E}_n(\mathbf{r}) = \nabla \phi_n(\mathbf{r}), \tag{4.26}$$

where $\phi_n(\mathbf{r})$ are scalar functions. They have to fulfil the biorthogonality condition

$$\int \varepsilon(\mathbf{r}) \nabla \phi_n(\mathbf{r}) \cdot \nabla (\widetilde{\phi}_m(\mathbf{r}))^* d^3r = M_n \delta_{nm}, \tag{4.27}$$

and this can be achieved by choosing $(\phi_n(\mathbf{r}), \sigma_n)$ to be a complete set of solutions to the eigenvalue problem for the scalar wave equation

$$\nabla \cdot (\varepsilon(\mathbf{r}) \nabla \phi_n) = \sigma_n \phi_n \ . \tag{4.28}$$

The set $(\widetilde{\phi}_n(\mathbf{r}), \sigma_n^*)$ is the corresponding set of adjoint solutions. It follows from (4.27) and (4.28) that the normalization factor M_n is given by

$$M_n = -\sigma_n \int (\widetilde{\phi}_n(\mathbf{r}))^* \phi_n(\mathbf{r}) d^3r \ . \tag{4.29}$$

These considerations lead to a Green's tensor $\mathbf{G}(\mathbf{r}, \mathbf{r}'; \omega)$ which is the sum of two terms

$$\mathbf{G} = \mathbf{G}_{GT} + \mathbf{G}_L, \tag{4.30}$$

where $\mathbf{G}_{GT}$ is the sum (4.20) over solutions to (4.21) and (4.24). It is therefore generalized transverse, i.e. $\nabla \cdot (\varepsilon \mathbf{G}_{GT}) = 0$. The other part $\mathbf{G}_L$ contains only longitudinal eigenfunctions, i.e.

$$\mathbf{G}_L(\mathbf{r}, \mathbf{r}'; \omega) = \sum_n \frac{\nabla \phi_n(\mathbf{r}) (\nabla \widetilde{\phi}_n(\mathbf{r}'))^*}{M_n k_0^2} \ . \tag{4.31}$$

Here we note that the field obtained by inserting the Green's tensor (4.30) and any current density into Eq. (4.4) can always be split into a generalized

transverse part and a purely longitudinal part. It is then seen using these fields and current densities in Eq. (4.3) that the current density must consist of a purely transverse part $\mathbf{j}_T$ with $\nabla \cdot \mathbf{j}_T = 0$ generating the generalized transverse field, and a part $\mathbf{j}_{GL}$ with $\nabla \times (\mathbf{j}_{GL}/\varepsilon) = \mathbf{0}$ generating the longitudinal field. We also note, that by choosing (ϕ_n, σ_n) to be a complete set of eigensolutions to (4.28) we ensure by construction that a current $\mathbf{j}$ with a longitudinal component in (4.4) will generate an electric field which satisfies the Coulomb equation $\nabla \cdot (\varepsilon \mathbf{E}) = -i\nabla \cdot \mathbf{j}/(\omega\varepsilon_0)$.

We shall only be concerned with the double-transverse Green's tensor (4.7). Inserting (4.30) in (4.7) gives

$$\mathbf{G}_T(\mathbf{r}, \mathbf{r}'; \omega) = \sum_n \frac{\mathbf{E}_n^T(\mathbf{r})(\widetilde{\mathbf{E}}_n^T(\mathbf{r}'))^*}{\lambda_n \int \varepsilon(\mathbf{r})(\widetilde{\mathbf{E}}_n(\mathbf{r}))^* \cdot \mathbf{E}_n(\mathbf{r}) d^3r} \quad + \quad \delta_T^\dagger \mathbf{G}_L \delta_T \quad , \qquad (4.32)$$

where

$$\mathbf{E}_n^T(\mathbf{r}) = \int \delta_T^\dagger(\mathbf{r}, \mathbf{r}') \cdot \mathbf{E}_n(\mathbf{r}') d^3r', \qquad (4.33)$$

and $\mathbf{E}_n$ are the generalized transverse solutions to (21) and (24). The transverse delta-operator δ_T is given in Appendix B. For real ε we have $\mathbf{E}_n^T = \mathbf{E}_n$, $\delta_T^\dagger \mathbf{G}_L \delta_T = \mathbf{0}$ and hence $\mathbf{G}_T = \mathbf{G}_{GT}$, but this does not hold for complex ε. In the next section this general approach to the electric field double-transverse Green's tensor is applied to the case of active optical fibers.

4.4 Transverse Green's tensor for the active optical fiber

In this section the general principles for construction of the electric field Green's tensor given in the previous section is applied to the case of an active optical fiber. The details of the calculation is given in the Appendices.

A schematic of the circular step-index optical fiber is shown in Fig. 4.1. The structure consists of a circular core region with refractive index n_1 surrounded by a cladding region with refractive index n_2. The diameter of the core is denoted $2a$. The extent of the cladding region is assumed to be infinite. A cartesian coordinate system (x,y,z) is introduced with the origin in the center of the fiber core. The fiber is oriented along the z-axis, and the position of a point source is given in cylindrical coordinates by (ρ,ϕ,z). The spontaneous emission depends on both the position and the orientation of the dipole vector μ. In this chapter we will consider spontaneous emission for emitters oriented along the z-axis, and for emitters oriented in the xy-plane. In the latter case we will be interested only in the average emission for

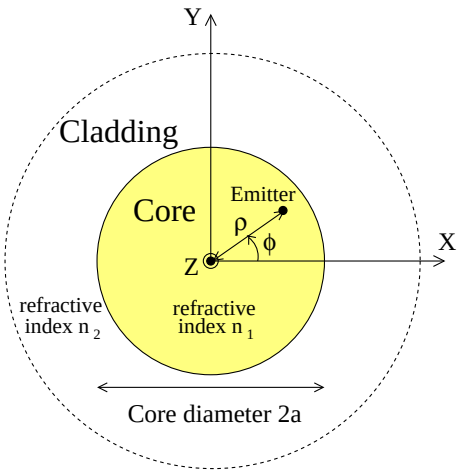

Figure 4.1: Illustration of the circular step-index optical fiber with core refractive index n_1, cladding refractive index n_2 and core diameter $2a$. A cartesian coordinate system (x,y,z) is introduced with the origin placed in the center of the fiber core, and with the fiber oriented along the z-axis. The position of a point source is given by $(\rho_0,\, \phi_0,\, z_0)$.

dipole vectors oriented along the two in-plane directions x and y. The total spontaneous emission for these two types of orientation of the generating currents depends only on the radius ρ due to symmetry considerations.

The formalism developed in Sec. 4.3 for calculating the transverse electric field Green's tensor requires that the generalized transverse eigensolutions $(\lambda_n; \mathbf{E}_n(\mathbf{r}))$ of Eq. (4.21) are obtained.

Taking advantage of the circular symmetry of the problem we will quantize the eigenfunctions $\mathbf{E}_n(\mathbf{r})$ in cylindrical wave functions. Generalized transverse solutions may be constructed by introducing both the electric field $\mathbf{E}_n$ and the magnetic field $\mathbf{H}_n$ given by $\mathbf{H}_n = \nabla \times \mathbf{E}_n/(i\tilde{\omega}_n\mu_0)$, where $\tilde{\omega}_n^2 = \omega^2 - \lambda_n c^2$, and requiring the tangential components of both fields to be constant across the interface between core and cladding.

The eigenmodes $\mathbf{E}_n$ and the corresponding fields $\mathbf{H}_n$ may be quantized in cylindrical wave functions in the form

$$\mathbf{E}_\alpha(\rho, \phi, z) = \mathbf{F}_\alpha(\rho) e^{im\phi} e^{i\beta z}, \tag{4.34}$$

$$\mathbf{H}_\alpha(\rho, \phi, z) = \mathbf{G}_\alpha(\rho) e^{im\phi} e^{i\beta z}, \tag{4.35}$$

where α represents the quantization indices. In a cylindrical coordinate system the vectors $\mathbf{F}_\alpha(\rho)$ and $\mathbf{G}_\alpha(\rho)$ do not depend on the angle ϕ, and

therefore the ϕ-dependence of these vectors has been suppressed. The eigensolutions may be divided into two types of solutions, which we refer to as radiation modes and guided modes, respectively. For radiation modes there are four quantization indices $\alpha = \{m, p, \beta, q\}$, where β is the component of the wave vector along the z-axis, q represents the magnitude of the wave vector perpendicular to the z-axis, m is the angular momentum, and the index p is used to distinguish between two degenerate polarization modes for given m, β, q.

In the first part of this section we will consider the contribution to the Green's tensor related to radiation modes, and then come back to the contribution related to guided modes at the end of the section.

Substitution of (4.34) into the eigenvalue problem (4.21) leads to the following differential equations for the z-component of the electric field for the optical fiber

$$\begin{aligned} &(\kappa\rho)^2 \tfrac{\partial^2 F_{z,\alpha}}{\partial(\kappa\rho)^2} + \kappa\rho \tfrac{\partial F_{z,\alpha}}{\partial(\kappa\rho)} + ((\kappa\rho)^2 - m^2) F_{z,\alpha} = 0 \quad , \rho \le a \\ &(q\rho)^2 \tfrac{\partial^2 F_{z,\alpha}}{\partial(q\rho)^2} + q\rho \tfrac{\partial F_{z,\alpha}}{\partial(q\rho)} + ((q\rho)^2 - m^2) F_{z,\alpha} = 0 \quad , \rho > a \end{aligned} \tag{4.36}$$

where

$$\begin{aligned} \kappa^2 &= ({k_0}^2 - \lambda_\alpha)\varepsilon_1 - \beta^2 \\ q^2 &= ({k_0}^2 - \lambda_\alpha)\varepsilon_2 - \beta^2. \end{aligned} \tag{4.37}$$

Here λ_α is the eigenvalue of the eigensolution with quantization indices α, and $\varepsilon_1 = {n_1}^2$ and $\varepsilon_2 = {n_2}^2$ represent the dielectric constant in the core and cladding of the fiber, respectively.

For radiation modes eigensolutions exist for all combinations of m, β, q. By applying the boundary condition that the field amplitude must remain finite both in the core and cladding the z-component of the two fields $\mathbf{F}_\alpha$ and $\mathbf{G}_\alpha$ may be written in the form

$$F_{z,\alpha}(\rho) = \begin{cases} A_\alpha J_m(\kappa\rho) & , \rho \le a \\ C_\alpha^+ {H^{(1)}}_m(q\rho) + C_\alpha^- {H^{(2)}}_m(q\rho) & , \rho > a \end{cases} \tag{4.38}$$

$$G_{z,\alpha}(\rho) = \begin{cases} B_\alpha J_m(\kappa\rho) & , \rho \le a \\ D_\alpha^+ {H^{(1)}}_m(q\rho) + D_\alpha^- {H^{(2)}}_m(q\rho) & , \rho > a \end{cases} . \tag{4.39}$$

The other components $F_{\rho,\alpha}$, $F_{\phi,\alpha}$, $G_{\rho,\alpha}$ and $G_{\phi,\alpha}$ may be expressed in terms of $F_{z,\alpha}$ and $G_{z,\alpha}$ by using Maxwells equations [1].

In the above equations J_m is the Bessel function of the first kind of order m, and ${H^{(1)}}_m$, ${H^{(2)}}_m$ are the Hankel functions of the first and second

kind of order m. The boundary conditions, which require $F_{z,\alpha}$, $F_{\phi,\alpha}$, $G_{z,\alpha}$ and $G_{\phi,\alpha}$ to be continuous across the core-cladding interface, result in four linear equations from which C_α^+, C_α^-, D_α^+, D_α^- are given in terms of A_α, B_α. For each set of indices β, q, m the polarization index p labels two linearly independent choices of A_α, B_α. A calculation of the relations between the coefficients A_α, B_α, C_α^+, C_α^-, D_α^+, D_α^- and a construction of a biorthogonal set of radiation modes is given in Appendix A.

We define the adjoint solution $\widetilde{\mathbf{E}}_\alpha$ to be $\widetilde{\mathbf{E}}_\alpha = (\mathbf{E}_{\widetilde{\alpha}})^*$, where $\widetilde{\alpha} = \{-m, p, -\beta, q\}$. It is clear that with this definition $\widetilde{\mathbf{E}}_\alpha$ is a solution to the complex conjugate of Eq. (4.21) such that $\mathcal{H}^\dagger \tilde{\mathbf{g}}_\alpha = \lambda_\alpha^* \tilde{\mathbf{g}}_\alpha$ for $\tilde{\mathbf{g}}_\alpha = \sqrt{\varepsilon^*}\widetilde{\mathbf{E}}_\alpha$. The reversion of angular momentum ($m \to -m$) and the direction of propagation ($\beta \to -\beta$) are chosen to satisfy the biorthogonality condition (4.17).

The part of the generalized transverse Green's tensor related to radiation modes may now be constructed, i.e.

$$\mathbf{G}^{(1)}{}_{GT}(\mathbf{r}, \mathbf{r}'; \omega) = \sum_{m,p} \int_{\beta=-\infty}^{\infty} \int_{q=0}^{\infty} \frac{\varepsilon_2 \mathbf{F}_\alpha(\rho) \mathbf{F}_{\widetilde{\alpha}}(\rho') e^{im(\phi-\phi')} e^{i\beta(z-z')}}{N_\alpha({k_0}^2 \varepsilon_2 - \beta^2 - q^2)} d\beta dq, \tag{4.40}$$

where the normalization factor N_α and the biorthogonality of radiation modes are given by

$$\int \varepsilon(\mathbf{r}) \mathbf{E}_\alpha(\mathbf{r}) \cdot \mathbf{E}_{\widetilde{\alpha'}}(\mathbf{r}) d^3 r = N_\alpha \delta_{mm'} \delta_{pp'} \delta(\beta - \beta') \delta(q - q'). \tag{4.41}$$

Here, α' is short-hand notation for $\alpha' = \{m', p', \beta', q'\}$.

The expression (4.40) is valid not only for passive fibers, but may also be used for fibers with gain and/or absorption. The expression may be simplified by introducing two new parameters k and θ related to β and q by

$$\beta = k \cos\theta, \tag{4.42}$$

$$q = k \sin\theta, \tag{4.43}$$

and by taking advantage of the identity

$$\frac{1}{x + i\epsilon} = P\frac{1}{x} - i\pi\delta(x), \tag{4.44}$$

where P refers to the principal value. The corresponding retarded Green's tensor taken at $\mathbf{r} = \mathbf{r}'$ may then be written

$$\begin{aligned} \mathbf{G}^{(1)}{}_{GT}(\mathbf{r}, \mathbf{r}; \omega + i\varepsilon) &= \sum_{m,p} P \left(\int_{k=0}^{\infty} \int_{\theta=0}^{\pi} \frac{\varepsilon_2 \mathbf{F}_\alpha(\rho) \mathbf{F}_{\widetilde{\alpha}}(\rho)}{N_\alpha({k_0}^2 \varepsilon_2 - k^2)} k dk d\theta \right) \\ &\quad - i \int_{\theta=0}^{\pi} I(\theta) \sin\theta d\theta, \end{aligned} \tag{4.45}$$

where

$$I(\theta) = \frac{\pi}{2} \sum_{m,p} \left(\frac{\varepsilon_2 \mathbf{F}_\alpha(\rho) \mathbf{F}_{\widetilde{\alpha}}(\rho)}{N_\alpha \sin\theta} \right)_{k=k_0\sqrt{\varepsilon_2}} . \tag{4.46}$$

For a fiber with absorption or gain in the core region (but not for a passive fiber) the principal value integral taken at $\mathbf{r} = \mathbf{r}'$ does converge, and this is true for both the imaginary part and real part of the integral. Modeling of spontaneous emission in active fibers requires a calculation of the imaginary part of the principal value integral. However, for passive structures the calculation is greatly simplified, since in this case $\varepsilon_2 \mathbf{F}_\alpha(\rho) \mathbf{F}_{\widetilde{\alpha}}(\rho)/N_\alpha$ is real, and the principal value integral does not contribute to $\mathrm{Im}(\mathbf{G}^{(1)}{}_{GT}(\mathbf{r}, \mathbf{r}; \omega + i\epsilon))$, which is the term appearing in the expression (4.12). In the second term of (4.45) the angle θ may be interpreted as the off-axis angle of propagation for light emitted into radiation modes, and accordingly the expression has the form of an integration over an off-axis angular radiation pattern, where the radiation pattern $I(\theta)$ is given by Eq. (4.46). This interpretation is, however, only valid for passive structures, since $I(\theta)$ may become negative for certain angles for active structures. A similar simple calculation of radiation patterns is not possible via Eq. (4.45) for active structures. In this case a calculation of physically meaningful radiation patterns must take into account amplification and absorption, which is possible by calculating radiation patterns using the Poynting vector. Radiation patterns for active structures are considered in Sec. 4.6.

The expressions (4.34), (4.35), (4.36) and (4.37) are also valid for guided modes, where q is now a complex parameter with a positive imaginary part leading to exponential decay in ρ of the amplitude of the eigenfunction. In this case the eigenfunctions are restricted to propagation only along the z-axis, and the degrees of freedom have been reduced relative to radiation modes. Therefore, β and q can no longer be chosen independently of one another, and only three quantization indices $\alpha = \{m, n, \beta\}$ must be summed over. We follow the usual convention and replace q by the variable $\gamma = -iq$. The z-component of a guided mode may then be written as

$$F_{z,\alpha}(\rho) = \begin{cases} A_\alpha J_m(\kappa\rho) & , \rho \le a \\ C_\alpha K_m(\gamma\rho) & , \rho > a \end{cases} , \tag{4.47}$$

$$G_{z,\alpha}(\rho) = \begin{cases} B_\alpha J_m(\kappa\rho) & , \rho \le a \\ D_\alpha K_m(\gamma\rho) & , \rho > a \end{cases} . \tag{4.48}$$

Here K_m is the modified Bessel function of the second kind of order m. As is also the case for radiation modes the coefficients A_α, B_α, C_α and D_α

must be chosen so that the boundary conditions are satisfied. Due to these conditions the allowed values for γ become functions of α, i.e. $\gamma = \gamma_\alpha$. Furthermore, each mode m, n only exists for $\mid \beta \mid \geq \beta_{m,n,c}$, where $\beta_{m,n,c}$ is a cut-off propagation constant such that $\mathrm{Re}(\gamma_\alpha) \geq 0$ for $\mid \beta \mid \geq \beta_{m,n,c}$. Here, we choose to use real propagation constants β, and accordingly the eigenvalues λ_α become complex. We will not here go into a detailed derivation of the guided modes of the fiber, as this is a topic that has been studied extensively in the literature (see for example [98, 99]). The contribution to the Green's tensor from the guided modes may be written

$$\mathbf{G}^{(2)}{}_{GT}(\mathbf{r}, \mathbf{r}'; \omega) = \sum_{m,n} \int_{|\beta| \geq \beta_{mn,c}} \frac{\varepsilon_2 \mathbf{F}_\alpha(\rho) \mathbf{F}_{\widetilde{\alpha}}(\rho') e^{i\beta(z-z')} e^{im(\phi-\phi')}}{N_\alpha ({k_0}^2 \varepsilon_2 + \gamma_\alpha^2 - \beta^2)} d\beta \ , \tag{4.49}$$

where $\widetilde{\alpha} = \{-m, n, -\beta\}$. The normalization factor N_α and biorthogonality relation for guided modes are given by

$$N_\alpha \delta_{mm'} \delta_{nn'} \delta(\beta - \beta') = \int \varepsilon(\mathbf{r}) \mathbf{E}_\alpha(\mathbf{r}) \cdot \mathbf{E}_{\widetilde{\alpha'}}(\mathbf{r}) d^3 r. \tag{4.50}$$

As was also the case for radiation modes the imaginary part may be greatly simplified for passive structures by taking advantage of the identity (4.44), i.e.

$$\mathrm{Im}\left(\mathbf{G}^{(2)}{}_{GT}(\mathbf{r}, \mathbf{r}; \omega + i\epsilon) \right) = -\pi {\sum}'_{m,n} \left(\frac{\varepsilon_2 \mathbf{F}_\alpha(\rho) \mathbf{F}_{\widetilde{\alpha}}(\rho)}{N_\alpha \mid \frac{d}{d\beta} (\beta^2 - {\gamma_\alpha}^2) \mid} \right)_{\beta^2 - {\gamma_\alpha}^2 = {k_0}^2 \varepsilon_2} . \tag{4.51}$$

Here, the prime means that only modes m, n with $\mid \beta_{m,n,c} \mid < k_0 \sqrt{\varepsilon_2}$ should be summed over.

The generalized transverse part of the retarded Green's tensor may now be obtained as the sum of the two contributions given in (4.40) and (4.49). The double-transverse Green's tensor may then be obtained by replacing the generalized transverse fields in the numerators of (4.40) and (4.49) by the transverse part of these fields. A method for calculating the transverse part of the generalized transverse fields is given in Appendix B. For fibers with relatively weak index contrast the difference between the generalized transverse and the usual transverse [62, 97] Green's tensor is almost negligible. However, this may not be the case for dielectric structures with high index contrasts such as those investigated by for example Dodabalapur et al. [100].

4.5 Spontaneous emission in a passive fiber

In this section we will evaluate the spontaneous emission going into radiation modes and bound modes for a passive optical fiber. Only for passive fibers is it really meaningful to consider the fraction of spontaneous emission going into specific modes, due to the existence of a complete set of orthogonal eigenmodes in this case. We will then in the following section consider physically meaningful radiation patterns for active fibers taking into account the effect of gain/absorption.

The passive fiber in concern is defined by a core refractive index $n_1 = 1.45$, a cladding refractive index $n_2 = 1.43$ and a core radius $a = 2\ \mu m$. The emitter is located at $\mathbf{r}_0 = (\rho_0, \phi_0, z_0)$ in the fiber. In order to properly normalize the spontaneous emission we will introduce the spontaneous emission Γ_{hom} from an emitter in a passive homogeneous dielectric material with the same refractive index as the core of the optical fiber, i.e.

$$\Gamma_{hom} = \frac{{\omega_0}^3 \mu^2 n_1}{\hbar \varepsilon_0 c^3 3\pi}, \tag{4.52}$$

where μ is the norm of the dipole vector μ. This expression is easily obtained using (4.12) for the case of a dipole at position $\rho_0 = 0$ and dipole orientation along the z-axis, or by use of the results for homogeneous dielectrics given in [68].

An example of the position-dependence of the spontaneous emission for an emitter with transition wavelength 1560 nm in the core of the fiber is shown in Fig. 4.2 for the case of dipole orientation along the z-axis (Γ_z) and for the average over the two in-plane dipole orientations x and y, i.e. $\Gamma_\perp = (\Gamma_x + \Gamma_y)/2$. The spontaneous emission averaged over all dipole orientations is given by $\Gamma = (\Gamma_x + \Gamma_y + \Gamma_z)/3$. The spontaneous emission into radiation modes clearly shows a modulation with position in the fiber which may be explained as a cavity effect. The periodicity $\Delta\rho_0$ in the spontaneous emission with position in the fiber core due to constructive/destructive interference arising due to reflections at the core-cladding interface should be roughly equal to one half wavelength in the medium, i.e.

$$\frac{\Delta\rho_0}{a} \approx \frac{\lambda_0}{2an_1}. \tag{4.53}$$

From this expression we obtain the periodicity $\Delta\rho_0/a \approx 0.27$. From the total emission for emitters with z-dipole direction (see Fig. 4.2(c)) the distance between local maxima or local minima is in the range from 0.26 to 0.28.

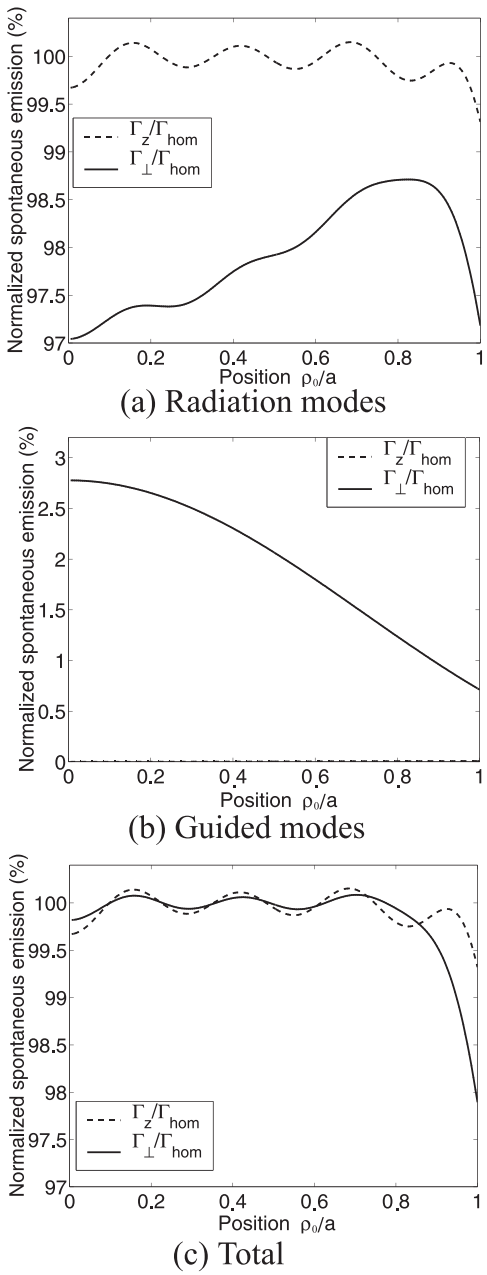

Figure 4.2: Spontaneous emission as a function of position for an emitter in the core of a step-index fiber with core refractive index n_1=1.45, cladding refractive index n_2=1.43 and core radius a=2 μm. The emission wavelength is λ_0=1560 nm.

Almost no spontaneous emission goes into guided modes for the case of dipole orientation along the z-axis. This is due to the electric field of the fundamental guided mode of the optical fiber having a negligible field component along the z-axis, i.e. the electric field is primarily in the xy-plane. Emission into radiation modes for dipole orientation in the xy-plane is clearly lower compared to the case of dipole orientation along the z-axis. This is due to part of the spontaneous emission being captured by the optical waveguide. From the total spontaneous emission into both guided modes and radiation modes we see that the total spontaneous emission is close to Γ_{hom} for all positions. Therefore Fig. 4.2(b) also gives a good estimate for the spontaneous emission factor, i.e. the fraction of the spontaneous emission going into the guided modes of the optical waveguide. The decrease in the total spontaneous emission near the core-cladding interface may be explained from the fact that the spontaneous emission in homogeneous dielectrics scales with the refractive index (see Eq. (4.52)), and emitters close to the core-cladding interface are affected by the presence of a material with a lower refractive index. The total emission near the core-cladding interface is clearly different for the different dipole orientations. This may be explained from the fact that the boundary conditions at the core-cladding interface depend on the field orientation, i.e. tangential electric field components are constant across the interface, whereas normal components differ by the factor ${n_1}^2/{n_2}^2 = 1.03$.

Figure 4.3 shows the spontaneous emission as a function of normalized frequency $V = k_0 a\sqrt{{n_1}^2 - {n_2}^2}$ for an emitter in the center of the fiber core ($\rho_0 = 0$). Also in this case the periodic oscillations seen in the spontaneous emission is due to constructive/destructive interference arising due to reflections at the core-cladding interface. The oscillations in the total spontaneous emission (Fig. 4.3(c)) are clearly larger for emitters oriented along the z-axis. Emitters with this orientation emit primarily in the xy-plane, and interference effects due to reflections from the core-cladding interface are therefore more pronounced. Emitters placed in the center of the waveguide with dipole orientation in the xy-plane are only allowed to interact with modes having angular momentum $m = \pm 1$. The fundamental fiber mode starts to become localized for normalized frequencies V just below 1. There are also guided modes with angular momentum ± 1 that become allowed for $V \geq 4$. Around both frequencies $V = 1$ and $V = 4$ a strong decrease is seen in the spontaneous emission going into radiation modes for in-plane dipoles. This is compensated by a corresponding strong increase in the spontaneous emission into guided modes, and the total rate of spontaneous emission is oscillating with frequency around Γ_{hom}. The spontaneous emission into

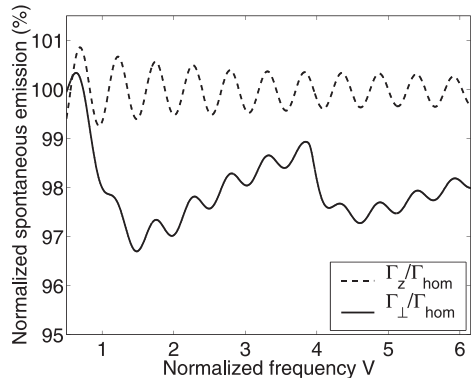

(a) Radiation modes

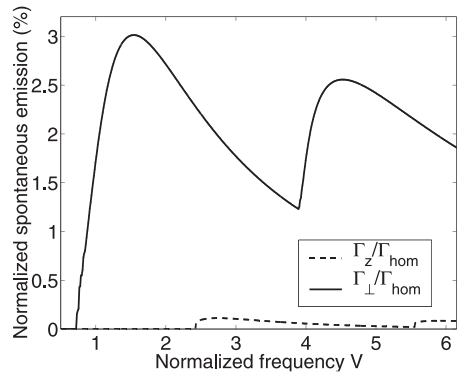

(b) Guided modes

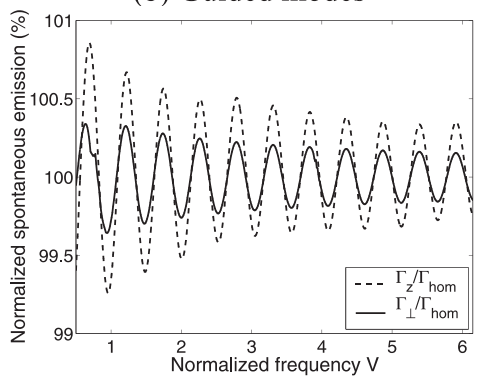

(c) Total

Figure 4.3: Spontaneous emission as a function of normalized frequency for an emitter located in the center of the core of a step-index fiber with n_1=1.45, n_2=1.43, a=2 μm.

guided modes for emitters with dipole orientation along the z-axis starts at normalized frequencies around $V \approx 2.4$. This frequency corresponds to the single-mode cutoff of step-index optical fibers [1].

The spontaneous emission as a function of normalized frequency is shown for two additional positions of the dipole emitter in Fig. 4.4. The spontaneous emission for the case of an emitter located at position $\rho = 0.5a$ is shown in Fig. 4.4(a). Here the spontaneous emission into radiation modes (guided modes) sharply decreases (increases) at a larger number of frequencies for the same frequency range as compared to the case of an emitter located in the center of the fiber core (see Fig. 4.3). This is because emitters located away from the center of a fiber core can couple to modes having a wider range of angular momenta m. Oscillations are also in this case observed in the total emission being the sum of emission into radiation modes and guided modes. The oscillation amplitude is, however, smaller as compared to the case of an emitter in the center of the core. Similar comments apply to Fig. 4.4(b) showing the spontaneous emission for an emitter at the edge of the core. The low amplitude of the oscillations in the total emission in this case is because the cavity effect is not very pronounced for emitters located close to the fiber-core edge.

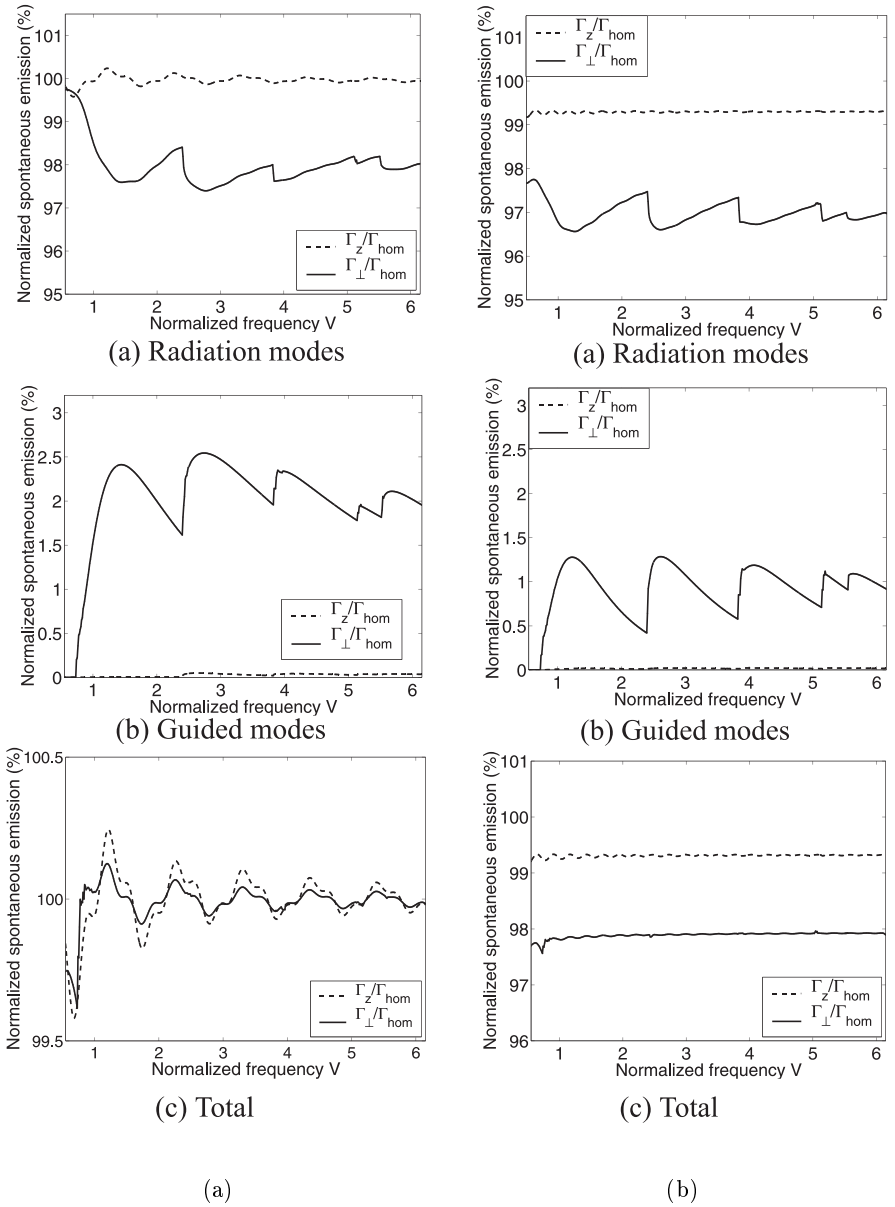

Figure 4.4: (a) Spontaneous emission as a function of normalized frequency for an emitter located mid between the center and the edge of the core ($\rho = 0.5a$) of a step-index fiber with n_1=1.45, n_2=1.43, a=2 μm. (b) emitter located at the edge of the core ($\rho = 1.0a$).

4.6 Spontaneous emission angular radiation patterns

The emission of radiation from active dielectric microstructures will in general differ from the spontaneous emission due to amplification or absorption of light. In this section we will present radiation patterns for active optical fibers taking into account the effect of the active material using a Poynting-vector approach.

In Fig. 4.5 the optical fiber is oriented along the z-axis in a cartesian coordinate system (x,y,z). Two angles θ and ϕ are introduced. The angular radiation pattern is defined as the radial emission per unit solid angle as a function of the direction given by θ and ϕ. For evaluating the angular

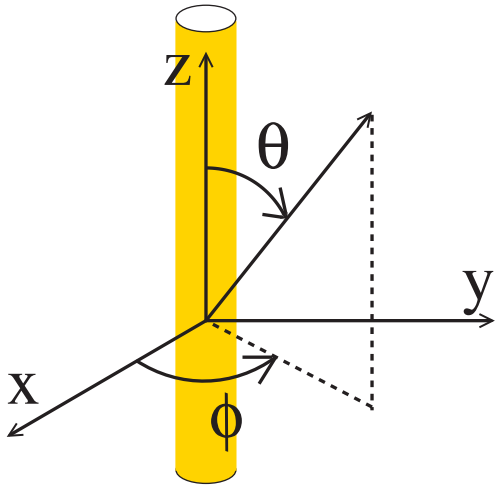

Figure 4.5: Illustration of an optical fiber oriented along the z-axis in a cartesian coordinate system (x,y,z). Two angles θ and ϕ are introduced.

spontaneous emission pattern in a rigorous way we may note that far away from the active fiber the power flux is radial, and the power flux dP per unit solid angle $d\Omega$ may be written in the form

$$\frac{dP}{d\Omega} = R^2 \mid \mathbf{S}(\mathbf{R}) \mid, \tag{4.54}$$

where $\mathbf{R}$ is the position relative to the source, $R = \mid \mathbf{R} \mid$, and $\mathbf{S}$ is the Poynting vector which for large distances R reduces to

$$\mathbf{S} = 2\frac{\mathbf{R}}{R}\varepsilon_0 n_2 c\langle\widehat{\mathbf{E}}^{\dagger}\cdot\widehat{\mathbf{E}}\rangle. \tag{4.55}$$

The emission rate into radiation modes per unit solid angle $d\Omega$ is given by

$$\frac{d\Gamma}{d\Omega} = \lim_{R\to\infty} \frac{1}{\hbar\omega} \mid \mathbf{S}(\mathbf{R}) \mid R^2. \tag{4.56}$$

Note that this expression only equals the *spontaneous* emission for passive structures, since for the case of amplifying or absorbing structures the spontaneously emitted light has been amplified or attenuated by the active medium.

The electric field at large distances is given in terms of the Green's tensor and generating currents by

$$\widehat{\mathbf{E}}(\mathbf{R}) = \int\int \mathbf{G}(\mathbf{R}, \mathbf{r}'; \omega + i\epsilon) \cdot (-i\mu_0\omega\widehat{\mathbf{j}}_T(\mathbf{r}'))d^3r'. \tag{4.57}$$

For the case of delta-correlated currents the amplitude of the electric field squared at position $\mathbf{R}$ generated by the transverse part of a dipole current at position $\mathbf{r}_0$ with dipole orientation $\mathbf{e}_i$ is given by

$$\langle \widehat{\mathbf{E}}(\mathbf{R})^\dagger \cdot \widehat{\mathbf{E}}(\mathbf{R}) \rangle = \mu_0^2\omega^4\mu^2 \mid \int \mathbf{G}(\mathbf{R}, \mathbf{r}'; \omega) \cdot \delta_T(\mathbf{r}', \mathbf{r}_0) \cdot \mathbf{e}_i \; d^3r' \mid^2, \tag{4.58}$$

and the spontaneous emission per unit solid angle in the direction given by $\mathbf{R}$ may in the limit of large distances $R =\mid \mathbf{R} \mid$ be written

$$\frac{d\Gamma}{d\Omega} = \frac{\omega^3\mu^2\sqrt{\varepsilon_2}}{\hbar\varepsilon_0 c^3} 2 \lim_{R\to\infty} \mid \int \mathbf{G}(\mathbf{R}, \mathbf{r}'; \omega) \cdot \delta_T(\mathbf{r}', \mathbf{r}_0) \cdot \mathbf{e}_i \; d^3r' \mid^2 . \tag{4.59}$$

For a gain medium the expression (4.59) only gives the amplified emission from the dipole at $\mathbf{r}_0$. We ignore the amplified spontaneous emission from the gain medium itself. The latter can be included by calculating $\langle \widehat{\mathbf{E}}^\dagger \cdot \widehat{\mathbf{E}} \rangle$, using (4.57) and the correlation relation (4.8).

For large R the electromagnetic field behaves as a plane wave with the wavenumber $k_0\sqrt{\varepsilon_2} = \sqrt{\beta^2 + q^2}$, and the magnitude of β and q is determined from the off-axis angle θ of the vector $\mathbf{R}$, i.e. $\beta = k_0\sqrt{\varepsilon_2}\cos\theta$ and $q = k_0\sqrt{\varepsilon_2}\sin\theta$. With this restriction imposed on β, q and using the notation for radiation modes in Sec. 4.4 a general expression for the angular emission pattern for active fibers generated by currents at position (ρ_0, ϕ_0, z_0) is given by

$$\frac{d\Gamma}{d\Omega} = \frac{\omega^3\mu^2\sqrt{\varepsilon_2}}{\hbar\varepsilon_0 c^3} 2 \frac{(2\pi)^2}{{k_0}^2\varepsilon_2 \sin^4\theta} \times$$

$$\left(\left| \sum_{m,p} C_\alpha^+ e^{-i\frac{m\pi}{2}} \frac{F_{i,\widetilde{\alpha}}^T(\rho_0) e^{im(\phi-\phi_0)}}{N_\alpha} \right|^2 + \right.$$

$$\left. \left| \sum_{m,p} \sqrt{\frac{\mu_0}{\varepsilon_0 \varepsilon_2}} D_\alpha^+ e^{-i\frac{m\pi}{2}} \frac{F_{i,\widetilde{\alpha}}^T(\rho_0) e^{im(\phi-\phi_0)}}{N_\alpha} \right|^2 \right). \qquad (4.60)$$

Here, $F_{i,\widetilde{\alpha}}^T(\rho_0) e^{-im\phi_0} e^{-i\beta z_0}$ is the component of the field $\mathbf{E}_{\widetilde{\alpha}}^T(\mathbf{r}_0)$ in the direction $\mathbf{e}_i$ corresponding to the orientation of the dipole vector. Note that the emission per unit solid angle Eq. (4.60) depends on both angles θ and ϕ, whereas the radiation pattern Eq. (4.46) does not depend on ϕ.

Figure 4.6 shows a calculation of the off-axis angular spontaneous emission pattern Eq. (4.60) averaged over the angle ϕ for an emitter in the center of the fiber core and at the edge of the fiber core, respectively, for a passive step-index fiber with core refractive index 1.45, cladding refractive index 1.43 and core radius 2 μm. The results presented in this figure may also be obtained directly using the off-axis angular radiation pattern given in Eq. (4.46). In fact, for a passive fiber the sum of expression (4.60) integrated over all solid angles and the corresponding contribution from guided modes will equal the expression (4.12). The transition wavelength of the emitter is 1560 nm. The radiation pattern for emitters oriented along the

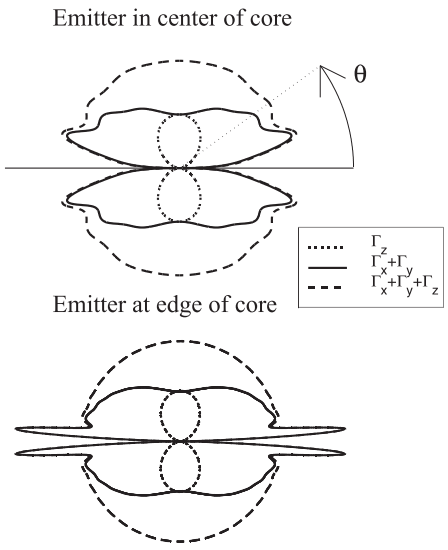

Figure 4.6: Spontaneous emission as a function of the off-axis angle for an emitter in the center of the core and an emitter at the edge of the core of a step-index fiber with n_1=1.45, n_2=1.43, a=2 μm, and for λ_0=1560 nm.

z-axis (Γ_z) closely resembles a figure eight ($\Gamma_z \propto \sin^2\theta$), which is the radiation pattern generated by a dipole in a homogeneous dielectric medium. Part of the radiation generated by emitters oriented in the xy-plane is captured by the optical waveguide, and for small off-axis angles θ the radiation pattern is clearly modified relative to the case of a homogeneous dielectric medium ($\Gamma_x + \Gamma_y \propto 1 + \cos^2\theta$). The radiation patterns shown in Fig. 4.6 are characterized by a peak for a small off-axis angle θ. As the transition wavelength decreases and approaches the cut-off wavelength for the next guided mode, the peaks will grow larger and the peak angle will move toward 0. As the wavelength drops below the cut-off wavelength the peaks being nearly parallel to the z-axis will disappear, and a new guided mode will appear. This explains that although abrupt changes with frequency is possible for the emission into radiation modes and guided modes, a similar abrupt change should not be expected in the sum of emission into radiation modes and guided modes. This is also in agreement with the results shown in Fig. 4.3 and Fig. 4.4.

Figure 4.7 shows a similar calculation of the angular emission patterns averaged over the angle ϕ for the case of emitters at the edge of the fiber core for the cases of fibers with amplification and absorption. Clearly, by

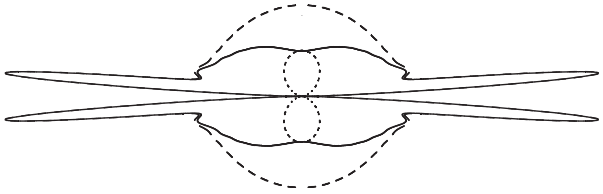

(a) n_1=1.45-i0.003

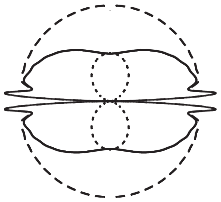

(b) n_1=1.45+i0.003

Figure 4.7: Spontaneous emission as a function of the off-axis angle for an emitter at the edge of the core of a step-index fiber with a=2 μm, n_2=1.43 and (a) $n_1 = 1.45 - i0.003$, (b) $n_1 = 1.45 + i0.003$, and for λ_0=1560 nm.

comparing Figs. 4.6 and 4.7 the effect from absorption in the fiber is a reduction in the peaks seen for small angles in Fig. 4.6, and the effect of gain is that these peaks are enhanced. The effect of an active medium will be most pronounced for small off-axis angles θ, where the emitted light will interact with the active material for a longer time and over longer lengths. Consequently, the amplification of spontaneous emission from in-plane emitters ($\Gamma_x + \Gamma_y$) will be more efficient compared to the case of emitters directed along the z-axis (Γ_z). The spontaneous emission as a function of position into radiation modes for a passive structure was given in Fig. 4.2(a). In this case the emission for in-plane emitters ($\Gamma_\perp = (\Gamma_x + \Gamma_y)/2$) is clearly lower for all positions $\rho_0 \leq a$ compared to the case of z-directed emitters (Γ_z). Fig. 4.2(a) may be obtained by integrating Eq. (4.60) over all solid angles. The physically measurable emission into radiation modes must reflect the effect of amplification or absorption for structures with an active medium. Figure 4.8 shows the measurable emission into radiation modes as a function of position ρ_0 for a fiber with gain. The emission for both the

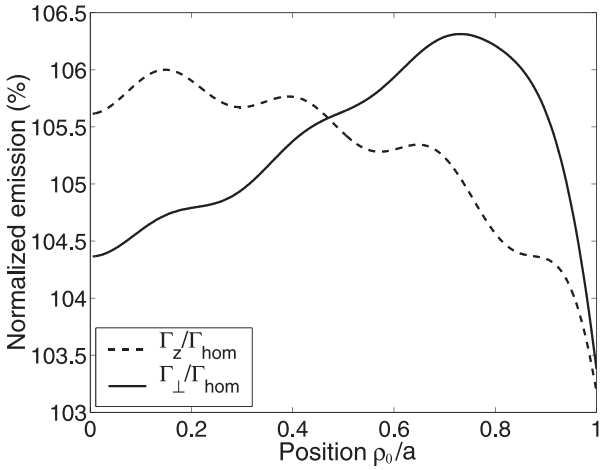

Figure 4.8: Emission into radiation modes as a function of position for an active fiber with n_1=1.45-i0.003 (gain), n_2=1.43, a=2 μm, and for λ_0=1560 nm.

considered orientations of the currents has increased relative to the spontaneous emission in the corresponding passive fiber, and the emission from in-plane oriented emitters ($\Gamma_\perp$) has been amplified more relative to the case of z-directed emitters (Γ_z). For both orientations of the emitter the amplification is clearly larger for emitters in the center of the core ($\rho_0 = 0$) relative to emitters at the edge of the core ($\rho_0 = a$).

For active fibers, where the distribution of active material is a function of the radius ρ only, averaging over the angle ϕ is reasonable. However, the Poynting vector approach does allow the dependence on the angle ϕ relative to the angle ϕ_0 related to the position of the emitter to be taken into account in the radiation patterns. An example is given for $\phi - \phi_0 = 0$, π in Fig. 4.9 for a fiber with absorption, a passive fiber, and a fiber with gain. The emitter is placed at the edge of the core. The radiation patterns are

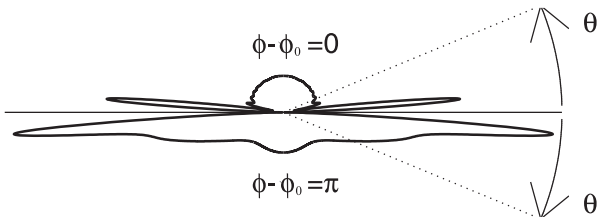

(a) n_1=1.45-i0.003

(b) n_1=1.45-i0.000 (c) n_1=1.45+i0.003

Figure 4.9: Emission versus off-axis angle for an emitter at the edge of the core of a step-index fiber with a=2 μm, n_2=1.43, (a) $n_1 = 1.45 - i0.003$, (b) $n_1 = 1.45 + i0.000$, (c) n_1=1.45+i0.003, and for λ_0=1560 nm.

clearly asymmetric due to the asymmetric position of the emitter ($\rho_0 \neq 0$). The effect of amplification or absorption is strongest for $\phi - \phi_0 = \pi$, since this direction corresponds to the opposite side of the active fiber relative to the emitter. Also in this case the peaks observed for small off-axis angles θ for a passive fiber increases (decreases) for a fiber with gain (absorption).

4.7 Conclusion

In conclusion, a general method has been developed for modeling of spontaneous emission in active dielectric microstructures. The fully vectorial method is based on the classical retarded electric field Green's tensor giving the relation between the quantum mechanical operators for the electric field and the generating currents. Taking advantage of the currents related to spontaneous radiative decay being transverse currents, allows a formalism,

where only the double-transverse Green's tensor needs to be calculated. The double-transverse part of the Green's tensor thus becomes a key ingredient in the model for spontaneous emission. A general approach was given for the construction of the Green's tensor for active dielectric microstructures. This approach does not rely on the existence of a complete power orthogonal set of electromagnetic modes, and is therefore valid for dielectric structures with absorption and/or amplification.

The method for spontaneous emission was applied to a fiber amplifier, and as a first step the Green's tensor for this structure was calculated. One of the terms in the calculated expression for the electric field Green's tensor was interpreted as an integration over an off-axis angular radiation pattern, and agreement has been found with this interpretation and radiation patterns calculated using the Poynting vector. A similar interpretation of the expression for the Green's tensor for fibers with gain or absorption is not possible, since a physically measurable radiation pattern must take into account the amplification or absorption of spontaneously emitted light due to the presence of an active medium. A Poynting vector approach has the advantage that radiation patterns that depend on both the off-axis angle and the azimuthal angle may be obtained.

For a passive fiber the expressions for the relevant parts of the Green's tensor become particularly simple, and for passive fibers the spontaneous emission going into radiation modes and guided modes was studied. Although the emission into these two types of modes is clearly different, and also depend on the orientation of the generating currents, the sum of these two contributions oscillates closely around the rate of spontaneous emission for a homogeneous dielectric medium with the same refractive index as the fiber core. The oscillations observed with position and frequency are explained as a consequence of destructive/constructive interference due to reflections from the interface between the fiber core and cladding. Abrupt changes with frequency in the emission into radiation modes and guided modes were observed at frequencies where new guided modes appear. Similar abrupt changes with frequency are not observed in the sum of these two contributions. This was explained from radiation patterns calculated using the Poynting vector approach, where strong peaks, being nearly parallel to the fiber axis, exist just before the next guided mode appears. The peaks disappear as the new guided mode appears.

The effect of an active medium on the radiation pattern is strongest for emission propagating at small off-axis angles. In particular the peaks transforming into a new guided mode as the frequency increases are enhanced (attenuated) for a core region with gain (absorption).

Chapter 5

Lippmann-Schwinger integral equation approach to the emission of radiation by sources located inside finite-sized dielectric structures

5.1 Introduction

A Lippmann-Schwinger type integral equation has been used in astrophysics to model the scattering of light incident on dielectric grains and particles of various shapes in three dimensions [101–105]. This type of integral equations has also been used to calculate the near fields in a situation where a plane wave or a laser beam is incident on a microstructured dielectric surface [106, 107]. By measuring the near fields in such a situation images can be created of the microstructure itself, and images can also be made of the fields in the microstructure [108–110].

In near field optics a typical situation is to illuminate a dielectric structure from the outside and investigate the scattered field in a plane above the structure [106]. In this case the light source is located outside the dielectric structure of interest. In this chapter the structures are not illuminated from the outside. Instead we further develop the existing in-

tegral equation methods to be capable of calculating the fields generated by sources located inside finite-sized dielectric structures. The introduction of sources in the integral equation formalism opens up for applying this method to the study of fields generated by current sources in antennas and optical components such as light-emitting-diodes (LED's) and vertical cavity surface emitting lasers (VCSEL's). The method may also have prospective uses for modelling of the quantum electrodynamic properties of dielectric media. The study of the emission of radiation from an electric dipole source has been widely used to model enhancement and reduction in the rate of spontaneos emission from e.g. an excited two-level atom [24, 27, 31, 37, 39, 50, 53, 68, 71, 86, 89, 90, 92, 93, 95, 111, 111]. For an electric dipole emitter located in a passive dielectric environment the total rate of emission is revealed both from the near field at the dipole position and from the integrated Poynting vector flux in the far field [39]. It was suggested already in 1946 by Purcell [20] that the rate of spontaneous emission can be modified indirectly via the electromagnetic properties of the structure in which the emitter is placed. An explanation is that a dielectric environment can modify the strength and distribution of electromagnetic modes with which the emitter can interact. The method presented in this chapter provides an additional method for approaching the calculation of (spontaneous) emission of radiation for emitters located inside general finite-sized dielectric structures.

In previous work a model was introduced for calculating near fields and far fields generated by sources located outside dielectric structures with cylindrical symmetry [40]. In that method a dipole source could not be placed inside the dielectric structure, and instead a dipole source in the center of a dielectric ring was considered. The reason for placing the dipole outside the dielectric material was that the numerical method required that we assumed constant fields within the elements in which the structure was discretized. This assumption is problematic for highly singular fields such as the dipole field. However, in this chapter we show how the singularity of the dipole field can be removed from the integral equation formalism. The procedure for removing the singularity adds some complexity to the numerical method but makes feasible the treatment of near fields and far fields generated by singular sources placed inside a dielectric structure. This new approach will be exemplified for a dipole source placed inside a dielectric disk with finite radius. The dielectric disk is a basic building block in e.g. the vertical cavity surface emitting laser and the microdisk laser [24, 27]. Singular electromagnetic fields and sources have previously been considered by van Bladel [112].

The method can generally be applied to all kinds of finite-sized dielectric structures. However, we will consider dielectric structures with cylindrical symmetry. The integral equation formalism will be formulated in a form where cylindrical symmetry is taken advantage of. Essentially the numerical problem is reduced from one problem, where the fields and the structure are discretized in three dimensions, to several problems, one for each angular momentum component of the field, where the fields and the structure are discretized in only two dimensions. In this case the structure is discretized into ring volume elements. A number of tests of the method for cylindrically symmetric structures will be presented so that the method can be compared to previous methods [102, 113] based on discretizing into cubic volume elements.

The chapter is organized in the following way. In section 5.2 the method is given for calculating near fields and far fields generated by sources located inside finite-sized dielectric structures, and it is shown how the numerical task can be reduced in the case of structures with cylindrical symmetry. The method for cylindrically symmetric structures is tested against analytic and numerical results in Sec. 5.3. The method is applied to the case of a dipole source located inside a cylindrically symmetric dielectric disk in Sec. 5.4. The conclusion is given in Sec. 5.5.

5.2 Method for calculating near fields and far fields generated by sources located inside dielectric structures

In this section a full-vectorial integral equation method is presented for calculating near fields and far fields generated by current sources placed inside finite-sized dielectric structures. The finite-sized dielectric structures are placed in a reference medium with known properties described by a Green's tensor. The finite-sized dielectric structure can be thought of as a scattering object in the reference system.

Scattering of light by dielectric structures with general geometries may be calculated using a Lippmann-Schwinger type integral equation of the form

$$\mathbf{E}(\mathbf{r}) = \mathbf{E}^0(\mathbf{r}) + \int \mathbf{G}(\mathbf{r}, \mathbf{r}'; 1) \cdot {k_0}^2 \left(\varepsilon(\mathbf{r}') - \mathbf{I}\right) \cdot \mathbf{E}(\mathbf{r}') d^3 r' \ , \qquad (5.1)$$

where $\mathbf{I}$ is the unit tensor, $\mathbf{r}$ and $\mathbf{r}'$ are position coordinates, and $\mathbf{E}^0$ is a field solution in the case without the scattering object. The scattering object is introduced via the dielectric tensor $\varepsilon(\mathbf{r})$, and since we consider free space

as the reference medium $\varepsilon(\mathbf{r}) - \mathbf{I}$ represents the change introduced in the reference medium by the presence of the scattering object. The retarded dyadic Green's tensor $\mathbf{G}(\mathbf{r}, \mathbf{r}'; 1)$ describes the scattering properties of the reference medium free space, and k_0 is the free space wave number. The field $\mathbf{E}$ is a field solution for the case where the scattering object is present in the reference medium.

In previous work (see e.g. Refs. [101–103, 113]) the incident wave is a plane wave or another beam of light incident upon the scattering object from the outside. The incident waves are typically solutions to the homogeneous wave equation without sources involved. However, it is also possible to consider scattering of fields generated by sources, and in that case $\mathbf{E}^0$ is the field that these sources would have generated if the scattering object was not present, i.e.

$$\mathbf{E}^0(\mathbf{r}) = i\omega\mu \int \mathbf{G}(\mathbf{r}, \mathbf{r}'; 1) \cdot \mathbf{J}(\mathbf{r}') d^3 r' \ , \tag{5.2}$$

where $\mathbf{J}(\mathbf{r})$ is the distribution of currents generating the field, ω is the angular frequency, and μ is the vacuum permittivity. The use of fields generated by a distribution of currents is interesting for modelling of antennas and various types of light-emitting optical components.

In the numerical procedure used for solving the Lippmann-Schwinger type integral equation (5.1) it is common to discretize the structure in a number of volume elements and assume constant fields within each volume element [101–103, 113]. The necessary assumption of constant fields within discretization elements was the main reason for placing a dipole source outside the dielectric structure in previous work [40], as this assumption is problematic for highly singular fields. In this chapter we will show how the integral equation (5.1) can be rewritten in a form where the singularity of the dipole field is removed. By removing the singularity from the integral equation it becomes feasible to calculate near and far fields generated by highly localized current disctributions, such as dipole currents, when the currents are located inside the scattering object.

The electric field $\mathbf{E}(\mathbf{r})$ generated by a dipole source at position $\mathbf{r}_0$ in a dielectric structure with dielectric constant $\varepsilon(\mathbf{r})$ is given in terms of the dyadic Green's tensor $\mathbf{G}(\mathbf{r}, \mathbf{r}_0)$ of the structure, i.e.

$$\mathbf{E}(\mathbf{r}) = \omega^2 \mu \mathbf{G}(\mathbf{r}, \mathbf{r}_0) \cdot \mathbf{d} \ , \tag{5.3}$$

where $\mathbf{d}$ is the dipole moment of the dipole source. The Green's tensor $\mathbf{G}(\mathbf{r}, \mathbf{r}_0)$ contains all scattering properties of the combined system of scattering object and reference system in which the dipole is placed. The Green's

tensor is a solution to the following integral equation

$$\mathbf{G}(\mathbf{r},\mathbf{r}_0) = \mathbf{G}(\mathbf{r},\mathbf{r}_0;1) + \int \mathbf{G}(\mathbf{r},\mathbf{r}';1)\cdot {k_0}^2(\varepsilon(\mathbf{r}')-\mathbf{I})\cdot\mathbf{G}(\mathbf{r}',\mathbf{r}_0)d^3r' \quad . \quad (5.4)$$

Also in this case, if we discretize the structure we cannot assume that $\mathbf{G}(\mathbf{r},\mathbf{r}_0)$ is constant within each discretization element due to the singularity of the Green's tensor at $\mathbf{r}=\mathbf{r}_0$. However, if the position $\mathbf{r}_0$ corresponds to a position with dielectric constant $\varepsilon = n^2$, and the dielectric constant is constant in the immediate vicinity of $\mathbf{r}_0$, then the Green's tensor can conveniently be written as the sum of two terms, where the first term is the Green's tensor for a homogeneous medium with refractive index n, and the second term $\mathbf{G}^{sc}$ is a scattering term that does not contain singularities, i.e.

$$\mathbf{G}(\mathbf{r},\mathbf{r}_0) = \mathbf{G}(\mathbf{r},\mathbf{r}_0;n) + \mathbf{G}^{sc}(\mathbf{r},\mathbf{r}_0) \quad . \quad (5.5)$$

By inserting the expression (5.5) into Eq. (5.4) we obtain an integral equation for the scattering term, i.e.

$$\mathbf{G}^{sc}(\mathbf{r},\mathbf{r}_0) = \mathbf{G}^{b}(\mathbf{r},\mathbf{r}_0) + \int \mathbf{G}(\mathbf{r},\mathbf{r}';1)\cdot {k_0}^2(\varepsilon(\mathbf{r}')-\mathbf{I})\cdot\mathbf{G}^{sc}(\mathbf{r}',\mathbf{r}_0)d^3r' \quad , \quad (5.6)$$

where

$$\begin{aligned}\mathbf{G}^{b}(\mathbf{r},\mathbf{r}_0) &= \mathbf{G}(\mathbf{r},\mathbf{r}_0;1) - \mathbf{G}(\mathbf{r},\mathbf{r}_0;n) \\ &+ \int \mathbf{G}(\mathbf{r},\mathbf{r}';1)\cdot {k_0}^2(\varepsilon(\mathbf{r}')-\mathbf{I})\cdot\mathbf{G}(\mathbf{r}',\mathbf{r}_0;n)d^3r' \quad . \quad (5.7)\end{aligned}$$

The electric field generated by a dipole source can similarly be written in the form

$$\mathbf{E}(\mathbf{r}) = \omega^2\mu\mathbf{G}(\mathbf{r},\mathbf{r}_0;n)\cdot\mathbf{d} + \mathbf{E}^{sc}(\mathbf{r}) \quad , \quad (5.8)$$

and the corresponding integral equation for the scattered electric field becomes

$$\mathbf{E}^{sc}(\mathbf{r}) = \mathbf{E}^{b}(\mathbf{r}) + \int \mathbf{G}(\mathbf{r},\mathbf{r}';1)\cdot {k_0}^2(\varepsilon(\mathbf{r}')-\mathbf{I})\cdot\mathbf{E}^{sc}(\mathbf{r}')d^3r' \quad , \quad (5.9)$$

where

$$\mathbf{E}^{b}(\mathbf{r}) = \omega^2\mu\mathbf{G}^{b}(\mathbf{r},\mathbf{r}_0)\cdot\mathbf{d} \quad . \quad (5.10)$$

The advantage of the integral equation (5.9) for the scattering term $\mathbf{E}^{sc}$ as compared to Eq. (5.1) is that $\mathbf{E}^{sc}$ is not singular, and consequently the assumption of constant scattered fields $\mathbf{E}^{sc}$ within small discretization elements is not problematic.

Before the new integral equation approach can be used it is necessary to first calculate the driving terms $\mathbf{G}^b$ and $\mathbf{E}^b$ which involve a volume overlap integral between two Green's tensors. The volume integral may involve integrating over a Green's tensor singularity at both positions $\mathbf{r}$ and $\mathbf{r}_0$. If these positions are far apart directly performing the volume integral is not problematic, but when $\mathbf{r} \approx \mathbf{r}_0$ performing directly the volume integral numerically requires a very high sampling density near the two singularities. Note that although there are several singular terms in the above expression (5.7) for $\mathbf{G}^b$ at $\mathbf{r} = \mathbf{r}_0$ the driving term $\mathbf{G}^b$ is not singular.

An appropriate method of handling the singularities in the driving terms is to transform the volume overlap integral Eq. (5.7) into a surface integral away from the singular points $\mathbf{r}$ and $\mathbf{r}_0$. A further advantage is that the calculation of the surface integral is much faster than the calculation of the volume integral. Consider a dielectric structure of the form

$$\varepsilon(\mathbf{r}) = n^2 \quad , \quad \mathbf{r} \in V \tag{5.11}$$

$$\varepsilon(\mathbf{r}) = 1 \quad , \quad \mathbf{r} \notin V \tag{5.12}$$

We will also consider the case of a dipole placed at a position $\mathbf{r}_0$ inside the volume V, where the refractive index is n. All structures considered in this chapter are of the form (5.11) and (5.12). In this case the term $\mathbf{G}^b$ can be written in the form

$$\mathbf{G}^b(\mathbf{r}, \mathbf{r}_0) = \mathbf{G}^{\partial V}(\mathbf{r}, \mathbf{r}_0) \qquad , \mathbf{r} \in V \tag{5.13}$$

$$\mathbf{G}^b(\mathbf{r}, \mathbf{r}_0) = \mathbf{G}^{\partial V}(\mathbf{r}, \mathbf{r}_0) - \mathbf{G}(\mathbf{r}, \mathbf{r}_0; n) \qquad , \mathbf{r} \notin V \tag{5.14}$$

where

$$\begin{aligned} \mathbf{G}^{\partial V} \quad = \quad & \frac{n^2 - 1}{{k_0}^2 n^2} \int_{\partial V} (\hat{n} \nabla' g_1 \cdot \nabla' \nabla' g_n - (\hat{n} \cdot \nabla' g_1) \nabla' \nabla' g_n - \\ & \frac{n^2}{n^2 - 1} (\hat{n} \cdot \nabla' g_n) \nabla' \nabla' g_1 + \frac{n^2}{n^2 - 1} g_n (\hat{n} \cdot \nabla') \nabla' \nabla' g_1 - \\ & \mathbf{I} {k_0}^2 \frac{n^2}{n^2 - 1} (g_1 \hat{n} \cdot \nabla' g_n - g_n \hat{n} \cdot \nabla' g_1)) dS' \ . \end{aligned} \tag{5.15}$$

Here ∂V refers to the surface of the volume V, $\hat{n}$ is the surface outward normal-vector, the prime ' denotes differentiation or integration with respect to the primed coordinates, and g_1, g_n are shorthand notation for the scalar

Green's functions $g_1 = g(\mathbf{r}, \mathbf{r}'; 1)$ and $g_n = g(\mathbf{r}', \mathbf{r}_0; n)$. The scalar Green's function is defined by

$$g(\mathbf{r}, \mathbf{r}'; n) = \frac{e^{ik_0 n|\mathbf{r}-\mathbf{r}'|}}{4\pi \mid \mathbf{r} - \mathbf{r}' \mid} \quad . \tag{5.16}$$

A derivation of the expressions (5.13)-(5.15), which is also valid for gain materials, is rather lengthy and involves converting a number of volume integrals into surface integrals by use of the Green theorems. A derivation is given in appendix C.

For general three-dimensional scattering objects a large number of discretization elements is typically required in the numerical procedure. Scattering of light by general three-dimensional objects has previously been investigated by e.g. Purcell and Pennypacker [101], Draine [102], Martin et al. [113] and Hoekstra et al. [103] by discretizing the dielectric structure of interest into cubic volume elements. However, for scattering objects with cylindrical symmetry it is possible to use another discretization scheme where the structure is discretized into ring volume elements [40]. The numerical task of calculating the field at all points inside the three-dimensional object can be replaced by a series of tasks where the field is calculated in two-dimensional planes. One calculation must be performed for each angular momentum component of the field. The field at all other points than those of the planes is obtained using symmetry considerations. For sources placed near the axis of cylindrical symmetry it is sufficient to consider a very small number of angular momentum components.

For cylindrically symmetric structures it is convenient to expand the fields $\mathbf{E}$ and $\mathbf{E}^0$ in angular momentum components in the form

$$\mathbf{E}^m(\mathbf{r}) = \left[\hat{z}E_z{}^m(\rho, z) + \hat{\rho}E_\rho{}^m(\rho, z) + \hat{\phi}E_\phi{}^m(\rho, z)\right] \exp(im\phi) \ , \tag{5.17}$$

where $\hat{\rho}$, $\hat{\phi}$, $\hat{z}$ are the coordinate unit vectors, and ρ, ϕ, z are the coordinates in a cylindrical coordinate system. For structures with cylindrical symmetry there can be no coupling between field components with different angular momentum, and therefore only the component of $\mathbf{E}^0$ with a given angular momentum component m is needed for calculating the component of the total field $\mathbf{E}$ with the same angular momentum.

For a given angular momentum m it is sufficient to discretize the field components $E_\rho{}^m$, $E_\phi{}^m$, $E_z{}^m$ in ρ and z. In this case the cylindrically symmetric structure is correspondingly also discretized in ρ and z. Here the structure is therefore discretized into ring volume elements. The Lippmann-Schwinger type integral equation (5.1) discretized into ring volume elements

may then be written

$$E_{p,i}{}^{m} - \sum_{j} \sum_{q,s=\rho,\phi,z} G_{pq,ij}{}^{m} k_0{}^{2} \left(\varepsilon_{qs} - \delta_{qs}\right) E_{s,j}{}^{m} = E_{s,j}{}^{0,m} \ , \tag{5.18}$$

where the indices i, j refer to ring elements, the indices p, q, s refer to the field components in a cylindrical coordinate system, and

$$G_{pq,ij}{}^{m} = \int_{ring\ \ j} \hat{p} \cdot \mathbf{G}(\mathbf{r}_i, \mathbf{r}'; 1) \cdot \hat{q}' e^{im(\phi' - \phi_i)} d^3 r' \ , \tag{5.19}$$

where the coordinate ϕ_i, which also affects $\mathbf{r}_i$ and $\hat{p}$, can be arbitrary. A similar integral equation for the scattering term $\mathbf{E}^{sc}$ for cylindrically symmetric structures is obtained by replacing $E_{p,i}{}^{m}$ by $E_{p,i}{}^{sc,m}$ and replacing $E_{p,i}{}^{0,m}$ by $E_{p,i}{}^{b,m}$ in Eq. (5.18), where $E_{p,i}{}^{b,m}$ represents the angular momentum components of $\mathbf{E}^{b}$, and $E_{p,i}{}^{sc,m}$ is the angular momentum components of $\mathbf{E}^{sc}$.

In this chapter we will consider dipoles located at the axis of cylindrical symmetry, the z-axis, and the orientation of the dipoles will be along the x-axis, i.e. $\mathbf{d} = d\hat{x}$ ($\hat{x} = \hat{\rho}$ when $\phi = 0$). In this case there are only two non-zero angular momentum components ($m = \pm 1$) of the fields. The components $E_{\rho,i}{}^{b,\pm 1}$, $E_{z,i}{}^{b,\pm 1}$ are in this case directly related to $\mathbf{E}^{b}(\mathbf{r})$ when $\mathbf{r}$ is in the xz-plane. The components $E_{\phi,i}{}^{b,\pm 1}$ are correspondingly related to $\mathbf{E}^{b}(\mathbf{r})$ when $\mathbf{r}$ is in the yz-plane.

The integrand in (5.19) is for $i = j$ integrated over the Green's tensor singularity. A convenient method of handling the singularity is again to convert the volume integral into a surface integral away from the singularity [114], i.e.

$$\begin{aligned} k_0{}^{2} G_{pq,ii}{}^{m} = \ & k_0{}^{2} \textstyle\int_{ring\ \ i} \hat{p} \cdot \mathbf{G}(\mathbf{r}_i, \mathbf{r}'; 1) \cdot \left(\hat{q}' e^{im(\phi' - \phi_i)} - \hat{q}\right) d^3 r' \\ - \ & \delta_{pq} + \textstyle\int_{\partial(ring\ \ i)} \hat{p} \cdot (-\mathbf{I}(\nabla' g(\mathbf{r}_i, \mathbf{r}'; 1) \cdot \hat{n}) \\ + \ & \hat{n} \nabla' g(\mathbf{r}_i, \mathbf{r}'; 1)) \cdot \hat{q} dS' \ , \end{aligned} \tag{5.20}$$

where the gradient is taken with respect to the primed coordinates, $\partial(ring\ \ i)$ refers to the surface of ring discretization element i, and $\hat{n}$ is the outward surface normal-vector. Again the angle ϕ_i can be chosen arbitrarily when it is kept in mind that ϕ_i also affects $\mathbf{r}_i$, $\hat{p}$ and $\hat{q}$.

In the limit of ring elements with very small height and width the Green's tensor elements Eq. (5.20) can be approximated by analytic results

of Yaghjian [115]. Using heights and widths that are so small that Yaghjian's results can be used directly is not practical. However, these analytic results are very useful for testing the calculation of $G_{pq,ii}$.

A strength of the Lippmann-Schwinger type integral equation methods is that the unknowns that have to be calculated to begin with can be restricted to the domain of the scattering object. After the field inside the scattering object is calculated the field outside the scattering object is directly given from the field inside by use of the Lippmann-Schwinger type integral equation.

5.3 Numerical tests of the method

In this section the integral equation method for structures with cylindrical symmetry will be tested against numerical results for scattering of a plane wave from a dielectric ring calculated by discretizing the ring in cubic volume elements. The case of cubic volume elements has e.g. been treated by Purcell and Pennypacker [101], Martin et al. [113], Draine [102] and Hoekstra et al. [103]. The method will also be tested against analytic results from Mie scattering theory. A similar comparison with Mie theory was presented by Draine [102] for cubic volume elements. We make a rough estimate of the reduction in the required number of discretization elements by comparing a calculation based on ring volume elements to the work of Draine based on cubic volume elements.

For the case of a plane wave incident on a dielectric sphere Mie scattering theory allows the calculation of e.g. extinction and absorption efficiency factors Q_{ext}, Q_{abs}. These factors are defined by

$$Q_{ext} = \frac{k_0}{\mid \mathbf{E}^0 \mid^2} \int \mathrm{Imag}\left(\mathbf{E}^{0*}(\mathbf{r}) \cdot (\varepsilon(\mathbf{r}) - \mathbf{I}) \cdot \mathbf{E}(\mathbf{r})\right) d^3r/\pi a^2 \ , \qquad (5.21)$$

$$Q_{abs} = \frac{k_0}{\mid \mathbf{E}^0 \mid^2} \int \mathrm{Imag}\left(\mathbf{E}^{*}(\mathbf{r}) \cdot (\varepsilon(\mathbf{r}) - \mathbf{I}) \cdot \mathbf{E}(\mathbf{r})\right) d^3r/\pi a^2 \ , \qquad (5.22)$$

where the incident plane wave is given by $\mathbf{E}^0(\mathbf{r})$, $*$ represents the complex conjugate operation, and the resulting total electric field is given by $\mathbf{E}(\mathbf{r})$. The dielectric sphere, which is the scattering object, is introduced via the dielectric constant $\varepsilon(\mathbf{r})$. The radius of the sphere is given by a. The extinction and absorption efficiencies are measures of how efficiently light is lost from the incident beam of light due to scattering and absorption. For the

case of a plane wave propagating along the z-axis only $m = +1$ and $m = -1$ needs to be considered for the angular momentum because

$$\mathbf{E}^0(\mathbf{r}) = \hat{x}E^0 e^{ik_0 z} = \left[\frac{1}{2}e^{i\phi}(\hat{\rho} + i\hat{\phi}) + \frac{1}{2}e^{-i\phi}(\hat{\rho} - i\hat{\phi})\right] E^0 e^{ik_0 z} \quad . \tag{5.23}$$

The numerical task is further simplified by the fact that the solution for the m=-1 field component can be obtained directly from the solution for the m=1 component by symmetry considerations. Therefore a numerical calculation is here only necessary for a single angular momentum component. Similarly, in the case of a dipole placed on the z-axis and polarized along the x-axis the field can be calculated by first solving for m=1 and then obtaining the corresponding solution for m=-1 by use of symmetry considerations.

Figure 5.1 shows the calculated extinction and absorption efficiencies for a plane wave incident on an absorbing dielectric sphere with refractive index 1.7+i0.1 obtained using 30, 66 and 112 ring discretization elements. Effective medium theory has been applied to the boundary of the sphere to improve the representation of the dielectric sphere when the sphere is discretized. This figure can be directly compared to a similar figure in Draine's work [102]

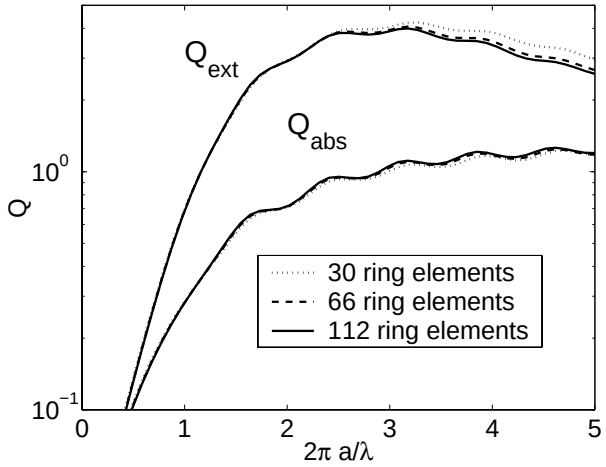

Figure 5.1: Extinction and absorption efficiencies for a plane wave incident on a dielectric sphere with radius a and refractive index 1.7+i0.1

where the sphere is discretized into cubic volume elements. By comparison we obtain similar convergence using typically 20 times less discretization elements. It can be checked that the solid curves in Fig. 5.1 are very close to analytically calculated extinction and absorption efficiency factors obtained

from Mie scattering theory. A ring element with a large radius will naturally replace more cubic volume elements than a ring element with a small radius. Because the volume elements are relatively close to the z-axis the difference in required discretization elements is *only* on the order of a factor 20. We will now consider another example, namely a dielectric ring, where the reduction in the number of discretization elements is significantly larger.

Consider a dielectric ring with height 15nm, outer diameter 100nm and inner diameter 70nm. The refractive index of the ring placed in free space is 3.6. This refractive index is representative of semiconductor materials such as GaAs at optical frequencies. The structure is cylindrically symmetric about the z-axis. The ring is illuminated by a plane wave propagating along the z-axis with the electric field polarized along the x-axis. The wavelength of the incident field is 1000nm. In Fig. 5.2 a contour plot is shown for the amplitude of the total field, being the sum of incident and scattered field, in a plane 20 nm below the dielectric ring. The shaded region in Fig. 5.2 shows the ring in the xy-plane. Figure 5.2 was calculated using 9 ring resolution

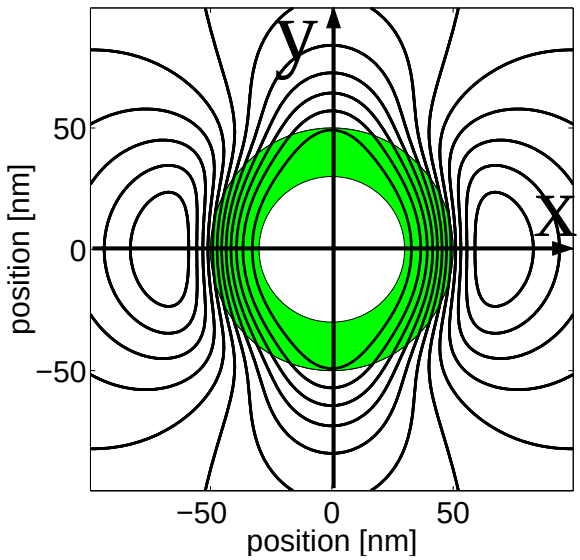

Figure 5.2: Contour plot of the amplitude of the electric field 20nm below a dielectric ring normalized to the amplitude of the incident plane wave. The dielectric ring has outer diameter 100nm, inner diameter 70nm and height 15nm. The refractive index of the ring placed in free space is 3.6.

elements. The resolution in the ρz-plane is therefore 5nm×5nm.

From symmetry considerations the field in the entire xy-plane 20nm below the dielectric ring can in fact be constructed from the field along the positive x-axis and positive y-axis in this plane. When the field is known along these two lines the field can be constructed at all other points in the plane by symmetry considerations. The amplitude of the field along the x-axis and the y-axis calculated using 9 ring resolution elements is shown as the solid curve in Fig. 5.3. Although Fig. 5.2 does not show directly where the intensity is low or high this can easily be seen from Fig. 5.3. Having both Fig. 5.2 and Fig. 5.3 it is an easy task to interpret the contour lines in Fig. 5.2. The boundaries of the dielectric ring in the xy-plane are indicated with vertical dotted lines. The dashed curve in Fig. 5.3 shows a similar

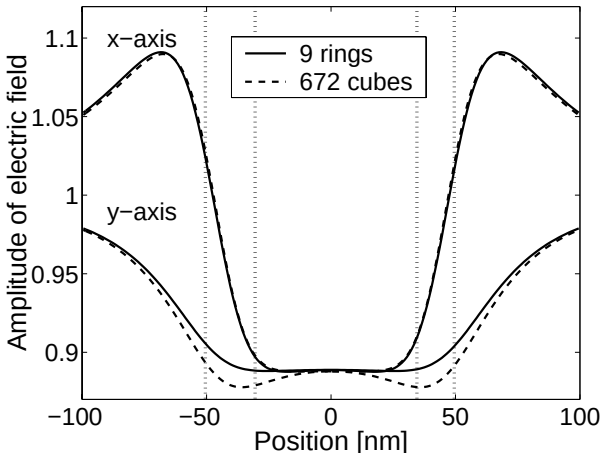

Figure 5.3: Amplitude of the electric field 20nm below a dielectric ring along the x-axis and y-axis. The ring is illuminated by a plane wave with unity electric field amplitude propagating along the z-axis. The ring has outer diameter 100nm, inner diameter 70nm and height 15nm. The refractive index of the ring placed in free space is 3.6. The ring boundaries along the x-axis and y-axis are indicated with vertical dotted lines.

calculation obtained by use of cubic volume elements with a corresponding resolution of 5nm×5nm×5nm. In this case 672 volume elements were required for resolving the dielectric ring. This corresponds to more than 70 times the number of used ring resolution elements. For the ring elements increasing the resolution to 36 points resulted in a difference of less than 0.001 for all positions in the xy-plane. This difference would hardly be visible in Fig. 5.3. The agreement between using cubic volume elements and ring elements is very good along the x-axis, and reasonable along the y-axis. In

the present case the convergence obtained using ring volume elements is far better compared to cubic volume elements because the circular boundary of the ring is treated exactly with ring elements. When cubic volume elements are used it is more difficult to obtain a good representation of the cylindrical boundaries. However, as the number of cubic volume elements is increased the result will converge to the result of the solid curve in Fig. 5.3.

5.4 Results for sources placed inside the dielectric disk

In this section the method for calculating near fields and far fields from sources located inside finite-sized dielectric structures will be applied to the case of a dipole source in the center of a cylindrically symmetric dielectric disk placed in free space. The axis of symmetry is the z-axis. The dipole source is polarized along the x-axis. The refractive index of the disk is 3.6. The height of the dielectric disk is $h = 150$nm. The emission wavelength is 1000nm, and the emission of radiation will be investigated for various choices of the disk radius.

For a passive dielectric structure there are two methods for calculating the total emission of radiation from the dipole source. The first method is to integrate the Poynting vector flux through a closed surface surrounding the emitter. A convenient approach is then to integrate the emission per unit solid angle in the far field over all directions. The power flux of emitted light dP per unit solid angle $d\Omega$ in the far field is given by

$$\frac{dP}{d\Omega} = \Gamma(\theta, \phi) = \lim_{r \to \infty} r^2 \mid \mathbf{S}(\mathbf{r}) \mid \ , \tag{5.24}$$

where θ and ϕ are angles that define the direction of the radius vector $\mathbf{r}$, and $\mathbf{S}$ is the Poynting vector, which for large distances $r = \mid \mathbf{r} \mid$ reduces to

$$\mathbf{S} = 2\frac{\mathbf{r}}{r}\varepsilon_0 c \mid \mathbf{E}(\mathbf{r}) \mid^2 \quad . \tag{5.25}$$

Here c is the vacuum speed of light. The total emission of electromagnetic radiation per unit time from the dipole source can be obtained by integrating the emission per unit solid angle over all directions, i.e.

$$\Gamma_{tot} = \int_{\phi=0}^{2\pi} \int_{\theta=0}^{\pi} \Gamma(\theta, \phi) \sin(\theta) d\theta d\phi \ . \tag{5.26}$$

Another method for obtaining the total emission of radiation from the dipole source in a passive dielectric structure is given by (see e.g. [39])

$$\Gamma_{tot} = 2\omega \mathbf{Imag}\left(\mathbf{d} \cdot \mathbf{E}(\mathbf{0})\right) \ , \tag{5.27}$$

i.e. the total emission is proportional to the imaginary component of the electric field along the dipole orientation at the position of the dipole. The expression (5.27) is not valid for active structures with absorption and gain [39]. Notice that the real part of the electric field along the direction of the dipole is highly singular at the dipole position. The expression (5.27) can be evaluated by calculating the near field inside the dielectric structure at the position of the dipole. The method presented in this chapter can be used for calculating the total emission by use of both Eqs. (5.26) and (5.27). The total emission from the dipole source calculated by use of Eq. (5.26) as a function of the radius of the disk is shown in Fig. 5.4 as the solid curve. The corresponding result obtained by instead using Eq. (5.27) is shown as the dashed curve. In both cases the total emission has been normalized relative to Γ_0 being the emission from the same dipole source when it is located in free space. From Fig. 5.4 it is clear that the emission rate peaks

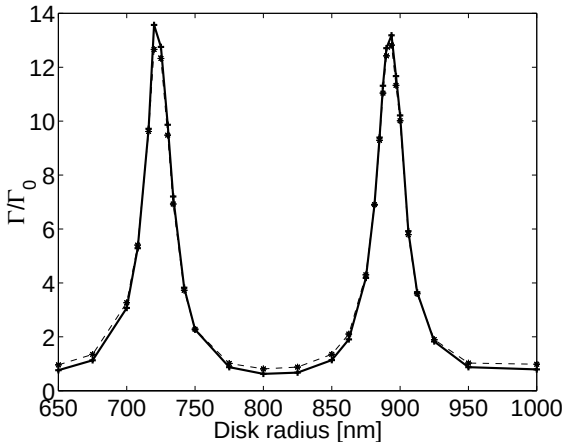

Figure 5.4: Emission rate from a dipole source located in the center of a dielectric disk. The disk is placed in free space. The refractive index of the disk is 3.6, and the height is 150nm. The emission wavelength is 1000nm.

for certain choices of the disk radius. The figure shows peaks in the emission rate around disk radii of 720nm and 894nm. The difference in disk radius for the two neighbouring peaks corresponds roughly to half a wavelength in the media for the fundamental mode propagating in a slab waveguide with same height and refractive index as the dielectric disk. Relative to the free space emission rate the total emission on resonance is enhanced by a factor of at least 13. In this calculation the dielectric disc has been discretized in ring elements with a height of app. 17nm and a width of 12.5nm or smaller. The

enhancement factor of 13 is not large compared to e.g. factors of around 300 found for dielectric microspheres (see e.g. [50, 53]). An increase by a factor 5 has been measured for spontaneous emission from quantum dots in GaAs-based pillar microcavities, and an increase by a factor 15 has been measured for a microdisk [32, 37, 116, 117].

In general, wether or not a resonance condition is fulfilled resulting in a large rate of emission depends on both position, emission wavelength, and orientation of the dipole emitter in the dielectric structure. The large difference in total emission on and off resonance also leads us to conclude that the emission can be very different for disks with a finite radius compared to the disks with infinite radius investigated by other authors [31, 71, 86, 89, 90, 92, 111, 118].

Differences in near fields on and off resonance are illustrated in Figs. 5.5 and 5.6. In Fig. 5.5 the amplitude of the electric field is shown for the disk

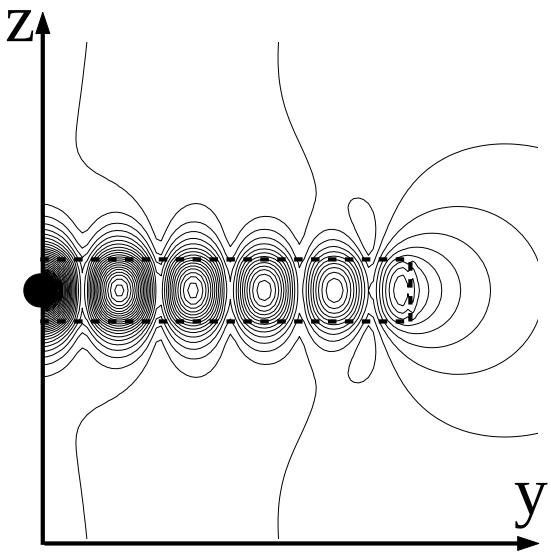

Figure 5.5: Amplitude of electric field in the zy-plane generated by an electric dipole in the center of a cylindrically symmetric dielectric disk with height 150nm, radius 894nm, and refractive index 3.6. The boundary of the dielectric disk in the yz-plane is indicated with a dashed line. The axis of cylindrical symmetry is the z-axis. The emission wavelength is 1000nm, and the dipole indicated with a black filled circle is oriented along the x-axis.

radius 894nm, where a resonance is seen in the total emission. The dashed curve indicates the boundary of the dielectric disk. The near field contour

plot shows that there are standing wave type resonances both along the z-axis and along the y-axis in the disk. Along the z-axis the height of the disk corresponds roughly to half a wavelength in the medium resulting in a half-wavelength type standing wave along the z-axis. The diameter of the disk is several wavelengths in the medium, and standing waves with nodes and antinodes along the y-axis are observed. The dipole is positioned exactly at the position of an antinode resulting in efficient coupling to the radiation field leading to the large emission rate. When making the contour plot a small region was excluded around the dipole, indicated with a black filled circle, because the dipole field amplitude becomes singular at the dipole position. From the near field image at resonance (Fig. 5.5) we can from the periodicity of the standing wave pattern along the y-axis estimate that half a wavelength in the media corresponds roughly to 175nm, which is roughly equivalent to the distance between the two peaks in Fig. 5.4.

The similar situation is shown in Fig. 5.6 for the disk radius 800nm. For

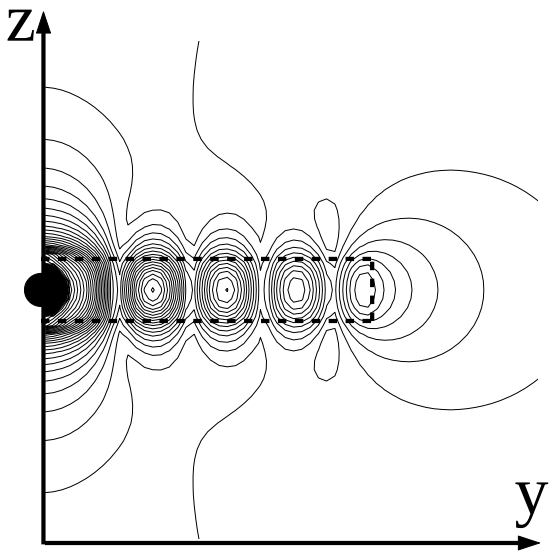

Figure 5.6: Amplitude of electric field in the zy-plane generated by an electric dipole in the center of a cylindrically symmetric dielectric disk with height 150nm, radius 800nm, and refractive index 3.6. The boundary of the dielectric disk in the yz-plane is indicated with a dashed line. The axis of cylindrical symmetry is the z-axis. The emission wavelength is 1000nm, and the dipole indicated with a black filled circle is oriented along the x-axis.

this choice of disk radius we again observe a standing wave pattern in the

near field both along the z-axis and along the y-axis. In this case, however, the dipole is not positioned at an antinode for the standing waves along the y-axis. The intensity still peaks in the center of the disk at the position of the dipole because the dipole field here is singular. Notice that compared to Fig. 5.5 the radius of the disk has been reduced by roughly one quarter wavelength in the media.

Some examples of far field radiation patterns are shown in Fig. 5.7 for four different choices of disk radius. The patterns show the emission per

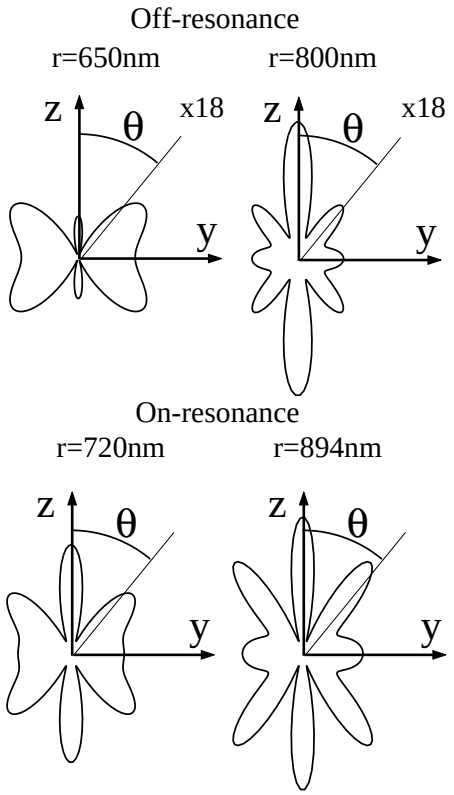

Figure 5.7: Far field angular emission patterns from a dipole source in the center of a cylindrically symmetric dielectric disk with height 150nm, and refractive index 3.6. The axis of cylindrical symmetry for the structure is the z-axis. The dipole is oriented along the x-axis. The emission pattern is shown for the disk radii $r = 650$nm, 720nm, 800nm and 894nm.

unit solid angle $\Gamma(\theta, \phi)$ as a function of the off-axis angle θ for a fixed azimuthal angle ϕ. In this case we consider the zy-plane $\phi = \pi/2$ as this is the plane in which the shape of the radiation patterns is most strongly af-

fected by the presence of the dielectric disk. The similar radiation patterns for the zx-plane all resemble a figure 8, which would also be the shape of the radiation pattern for the dipole in free space for the zx-plane. The free space radiation pattern for the zy-plane is a circle, and it is therefore clear that the shapes of the radiation patterns in Fig. 5.7 are very different compared to the free space radiation pattern. The four far field patterns can be compared in magnitude when it is taken into account that the amplitude of the far field plots for the radius 650nm and 800nm have been multiplied with a factor 18 as compared to the results for radii 720nm and 894nm. Consider for example the far field emission pattern for the radius 800nm. In this emission pattern there are certain preferred directions for emission of radiation. These preferred directions of emission are not easily recognized from a near field image such as Fig. 5.6. A clear correspondence between the near field image and the far field emission pattern becomes apparent when the near field image is extended to show the fields in distances of several free space wavelengths away from the dielectric disk. In Fig. 5.8 the near field for the radius 800nm is shown for a large spatial region. In this case we obtain

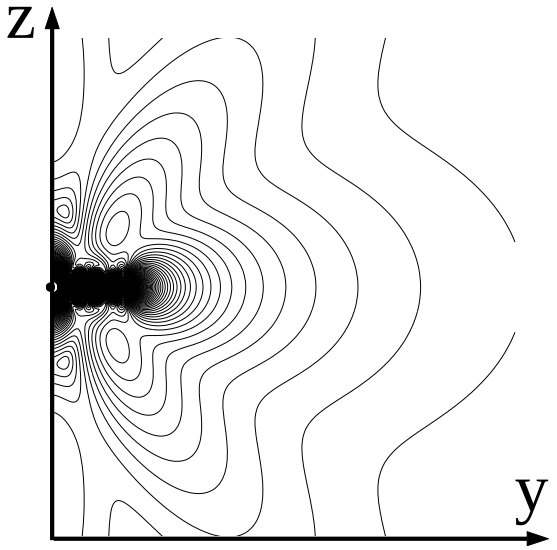

Figure 5.8: Amplitude of electric field in the zy-plane generated by an electric dipole in the center of a cylindrically symmetric dielectric disk with height 150nm, radius 800nm, and refractive index 3.6. The axis of cylindrical symmetry for the disk is the z-axis. The emission wavelength is 1000nm, and the dipole is oriented along the x-axis.

a clear correspondence between the preferred directions of propagation in both near field and far field images.

5.5 Conclusion

In conclusion, an integral equation method has been presented for calculating the emission of radiation generated by sources located inside finite-sized dielectric structures. The integral equations were formulated in a way that removes the singularity in the dipole field from the equations that are going to be solved. It was shown how integral equations can be formulated to take advantage of cylindrical symmetry. In the method for cylindrically symmetric dielectric structures the structure is discretized in ring volume elements. The method based on ring volume elements was tested and compared to a previous method that does not take advantage of cylindrical symmetry based on discretizing into cubic volume elements. Depending on the choice of dielectric structure we observed large reductions in the required number of discretization elements. For a dielectric sphere the reduction was on the order of a factor 20, and for a dielectric ring the reduction was on the order of a factor 70.

The method for sources located inside dielectric structures was exemplified for a dipole source located in the center of a dielectric disk. The total rate of emission from the dipole source was investigated for various choices of the disk radius. The total emission was enhanced relative to the corresponding rate for the dipole in free space by a factor 13. Certain disk radii resulted in a resonance condition to be fulfilled leading to efficient coupling of the dipole to the radiation field. Near fields and far fields were presented for choices of disk radius resulting in high and low emission of radiation. In the case of high emission (resonance) the dipole was shown to be located at an antinode of a standing wave pattern in the field inside the disk.

Part II

Planar photonic crystal waveguides

Chapter 6

Introduction - part II

The chapters 7-10 are devoted to the topic of planar photonic crystal waveguides (PCW's). The general idea behind PCW's is to create a waveguide by introducing a line defect in a photonic crystal. Both the choice of photonic crystal and line defect design can have a significant influence on the optical properties of the waveguide. There is a significant task in understanding what are the optical properties of planar photonic crystal waveguides, and more importantly in understanding how such waveguides can be designed or engineered to have optical properties that are interesting for making novel or more efficient optical components for e.g. telecommunications applications. From the work presented we will obtain some understanding of what are the appropriate designs of planar photonic crystal waveguides. Attention will be given to designs of PCW's characterized by leakage-free guidance of light and a large bandwidth.

Only our imagination and time sets a limit for the number of possible choices of PCW designs that we can make. The number of possibilities may be narrowed down a bit by choosing photonic crystals and waveguide designs that can be realized experimentally within a reasonable time. Photonic crystal waveguides are characterized by characteristic dimensions that are comparable to the wavelengths of the photonic bandgap wavelength range of the photonic crystal. For a PCW based on periodically arranged air-holes in silicon and operated at a wavelength of 1500nm the photonic crystal lattice constant may be on the order of 400nm [119]. The diameter of the air-holes might be on the order of 300nm such that walls between air-holes are only 100nm thick. Experimental realization of such structures is a formidable task but a task that presently receives significant attention, and experimentally fabricated PCW's with these small dimensions have ap-

peared [119–131].

The initial theoretical work on PCW's was to a large extent fundamental research for two-dimensional PCW's [18, 19, 132–137]. In these structures e.g. high-refractive-index rods placed in air are assumed to be infinitely high or air-holes in a high-refractive-index material are assumed infinitely deep. In the two-dimensional picture there is perfect confinement of light to the waveguide region. The chapter 7 contains fundamental research on the electromagnetic energy flow in two-dimensional planar PCW's. The waveguides considered in chapter 7 are based on a photonic crystal consisting of high-refractive-index rods arranged on a triangular lattice. The rods are assumed to be infinitely high such that the structure and fields can be treated in a two-dimensional approach. An interesting type of waveguide may be created by removing a row of rods in the photonic crystal. This type of waveguide is interesting from a fundamental point of view because light may be confined to a region with *low* refractive index, an air line-defect. The section gives an account of how the number of guided modes, the Poynting vector distribution of the modes and their dispersion properties depend on the wavelength for a range of waveguides. The examples illustrate that the complex electrodynamics of planar PCW's can be very different compared to conventional waveguides. Chapter 7 is based on plane-wave-expansion results from Ref. [19].

Any real planar waveguide does not have infinitely high rods or infinitely deep holes such that the structures are two-dimensional. In two-dimensional PCW's there can be perfect confinement of light to the waveguide region. Natural questions to raise are what will be the influence of the finite height of real PCW's, and to what extent are calculations for two-dimensional structures valid. An important issue to address is how finite-height PCW's can be designed such that light does not leak out of the waveguide channel, or such that losses due to leakage of light are low. In chapter 8 it is shown how two-dimensional calculations can be used to address the design of leakage-free finite-height planar PCW's. Design guidelines are obtained for finite-height structures by comparing two-dimensional calculations with dispersion relations for the media above and below the finite-height structure. Leakage-free guidance of light can be achieved with a high vertical index contrast when also the waveguiding region has a high refractive index. Chapter 8 is based on results from Ref. [138] and excerpts from Ref. [139].

Waveguides with a small vertical refractive index contrast operated at frequencies in the bandgap are inherently lossy because the vertical refractive-index contrast is not sufficiently high to completely confine the light vertically. However, the propagation losses can be low. Experimentally losses as

low as 11dB/mm and 20dB/mm have been reported [122, 126]. Modelling of these losses is pursued by a number of authors [140, 141]. Leakage-free guidance of light is not possible for a small vertical refractive-index contrast.

Obtaining leakage-free guidance of light in planar PCW's requires first of all a sufficiently high vertical refractive-index contrast between a finite-height PCW and the material above and below the finite-height PCW. The highest vertical refractive-index contrast is achieved when the PCW is suspended in air or free space. Photonic crystal slabs suspended in air have been investigated experimentally both for making lasers [142] and for making waveguides [120, 123, 127, 143, 144].

A sufficient vertical refractive-index contrast can also be achieved by using the semiconductor-on-insulator materials system [119, 121, 128, 129, 145]. Due to the smaller vertical index contrast the part of the photonic bandgap region, in which leakage-free bandgap guidance of light is possible, is smaller compared to the case of a photonic crystal slab suspended in air. On the other hand the waveguide design is more robust [119].

Although a careful interpretation of two-dimensional calculations can be used to provide design guidelines for finite-height structures this method cannot generally be used for calculating the exact dispersion properties and exact frequency ranges of guidance for finite-height PCW's. Furthermore, three-dimensional calculations can be used to address the vertical localization of light which is not possible with two-dimensional calculations. In order to obtain good agreement between experiments and theory it is therefore necessary in some cases to use three-dimensional calculations. In chapter 9 both two-dimensional and three-dimensional calculations are presented for a finite-height planar PCW that has been experimentally realized [119, 130]. The theoretical work presented in chapter 9 for frequency ranges with leakage-free guidance of light and localization of guided electromagnetic modes is in reasonable agreement with experimental transmission measurements [130, 146]. Chapter 9 is based on Ref. [146].

The theoretical work by the author [138, 139, 146] and by other researchers [128,145,147] for finite-height PCW's shows that leakage-free waveguides with a high refractive index in the waveguiding region have very flat dispersion curves that only cover narrow frequency intervals. Consequently such waveguides are characterized by narrow bandwidth and very low group velocity for guided modes resulting in a large modal dispersion mismatch between the PCW's and more conventional planar waveguides or fibers that might be used for coupling light into the planar PCW's. In chapter 10 general design principles are presented for obtaining both a large bandwidth and leakage-free guidance of light. Chapter 10 is based on Ref. [148].

Chapter 7

Energy flow in planar photonic crystal waveguides

7.1 Introduction

This chapter contains fundamental research on the electromagnetic energy flow in planar photonic crystal waveguides (PCW's). The waveguides considered are created by introducing a line defect in a photonic crystal with high-refractive-index rods arranged on a triangular lattice. Two possible orientations of the line defect in the photonic crystal material are considered. The rods are assumed to be infinitely high such that the structure and fields can be treated in a two-dimensional approach. The chapter gives an account of how the number of guided modes, the Poynting vector distribution of the modes and their energy velocity and dispersion depend on the wavelength and waveguide width. The work illustrates that geometric parameters such as the line defect orientation and the defect width have a significant influence on the electrodynamics.

In section 7.2 a description is given of the banddiagram representation of the properties of PCW's, and the method used for calculating fields and banddiagrams is described. An analysis of straight PCW's including the analysis of two possible line defect orientations is given in section 7.3. A conclusion is given in section 7.4. In this thesis only straight planar PCW's will be considered. Further work on the flow of energy at branching points calculated using the finite-difference-time-domain (FDTD) method can be found in Ref. [19].

7.2 Supercell method to planar photonic crystal waveguides

The fields and banddiagrams for planar PCW's presented in this thesis have all been calculated by the plane-wave-expansion method and a supercell approach. The plane-wave-expansion method for calculating the electromagnetic fields and frequencies of Bloch modes in periodic structures has already been introduced in chapter 3. In chapter 3 the supercell method was applied to a cavity such that the cavity was approximated by periodically repeated cavities. In a similar way a planar PCW can be approximated by a structure with periodically repeated waveguides. This approach is illustrated in Fig. 7.1(a), where we consider a planar PCW created by first removing a row of rods in a photonic crystal structure with high-refractive-index rods (dielectric constant $\varepsilon = 11.4$) arranged periodically on a triangular lattice in air (dielectric constant $\varepsilon = 1$), and then adjusting the width to W. The diameter of the circular dielectric rods is in chapter 7 given by $D = 0.4\Lambda$, where Λ is the lattice constant of the photonic crystal. For this choice of diameter the photonic crystal has a large photonic bandgap for TM-polarized light (electric field oriented along the z-axis) [2].

The waveguide is approximated by a periodic structure described by the supercell indicated in Fig. 7.1(a) with a dashed line. In the approximate structure used in the calculations the super cell is repeated periodically. The height of the supercell H determines the distance between neighbouring waveguides in the periodic approximation. The electromagnetic fields in the periodic structure defined by the super cell may be written as an expansion of Bloch modes in the form

$$\mathbf{E}_{\mathbf{k},n}(\mathbf{r}) = \mathbf{U}_{\mathbf{k},n}(\mathbf{r})e^{i\mathbf{k}\cdot\mathbf{r}} \ , \tag{7.1}$$

where $\mathbf{U}_{\mathbf{k},n}$ is a function with the same spatial periodicity as the structure, $\mathbf{k}$ is the Bloch wave vector which we restrict to the 1. Brillouin zone shown in Fig. 7.1(b), and n represents different discrete solutions for the same Bloch wave vector. For the choice of supercell shown in Fig. 7.1 there are five rows of rods between neighbouring waveguides. As we increase the number of rows of rods between neighbouring waveguides, and thereby increase H, the corresponding decrease in the size of the Brillouin zone is compensated by a corresponding increase in the number of modes n when light is not localized to the line defect. In the limit where the height H is increased to infinity the Brillouin zone reduces to a line interval, and the direction of $\mathbf{k}$ is then fixed to the direction of the waveguide, in this case the x-axis. The field

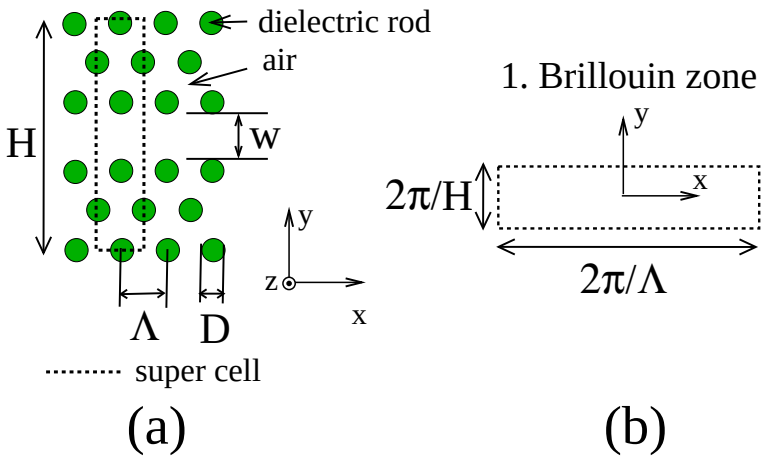

Figure 7.1: (a) Two-dimensional photonic crystal waveguide made by introducing a line defect in a photonic crystal consisting of high-refractive-index rods arranged on a triangular lattice. The width of the waveguide is denoted by W. A supercell is shown with a dashed line. (b) Dimensions of the 1. Brillouin zone corresponding to the supercell shown in (a).

solutions in this limit may be written in the form

$$\mathbf{E}_{k,n}(\mathbf{r}) = \mathbf{U}_{k,n}(\mathbf{r})e^{ikx} \quad , \tag{7.2}$$

where we now consider a scalar wave number k, and the index n now represents both a continuum of solutions for modes that are not localized to the line defect and a number of discrete solutions for modes localized to the line defect. In practice the height H is increased to a finite but appropriate level that is large enough to make the coupling between neighbouring waveguides negligible for the localized modes. In the forthcoming sections we will show diagrams of the allowed frequencies versus the scalar wave number k to describe the dispersion properties of planar PCW's.

7.3 Straight photonic crystal waveguides

Photonic crystal waveguides are created by introducing line defects in photonic crystals, and there are several possible orientations of the line defect. Two orientations will be considered. We will refer to the orientation of the line defect in Fig. 7.1 as *first orientation*. In this case the line defect is created along the x-axis which gives a short spatial periodicity in the direction of the waveguide that equals the lattice constant Λ. The length of

the Brillouin zone in this case is $2\pi/\Lambda$. It is also possible to orient the line defect along the y-axis giving the spatial periodicity $\sqrt{3}\Lambda$ in the direction of the waveguide. This case is referred to as *second orientation*. For second orientation the size of the Brillouin zone is $2\pi/\sqrt{3}\Lambda$ and is correspondingly smaller compared to first orientation.

7.3.1 Waveguides with first orientation

Fig. 7.2 shows a TM banddiagram for in-plane propagating Bloch modes in the two-dimensional PCW with first orientation for four values of the waveguide width W. The diagram shows the allowed combinations of normalized wave number $k\Lambda/2\pi$ and normalized mode frequency Λ/λ, where λ is the free-space wavelength. The continuum regions in the figure repre-

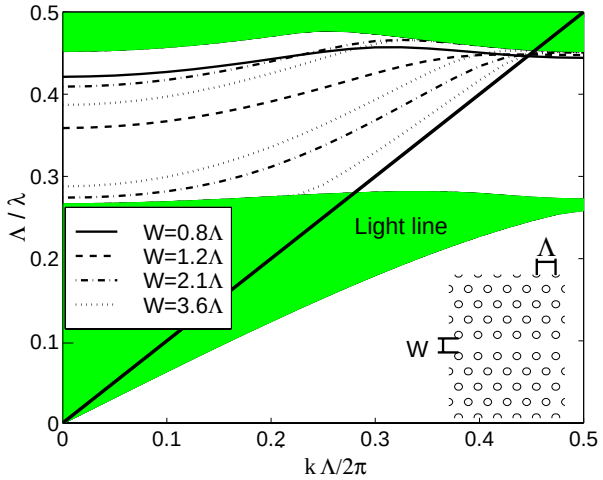

Figure 7.2: Allowed frequencies for TM polarized modes in the straight photonic crystal waveguide (shown as an inset) for four different values of the width W.

sent a continuum of modes that are not localized to the region of the line defect. These modes will be referred to as cladding modes. The discrete bands in Fig. 7.2 represent modes that are localized to the region of the line defect, and these modes are guided modes. A TM bandgap exists for the photonic crystal cladding in the interval from $\Lambda/\lambda \approx 0.27$ to 0.45 where no cladding modes are allowed. The existence of TM polarized Bloch modes in this frequency range is only possible due to the line defect in the photonic crystal.

Fig. 7.2 shows that only one defect band exists for the widths $W = 0.8\Lambda$ and $W = 1.2\Lambda$. As the width of the waveguide is increased to $W = 2.1\Lambda$, two defect bands are allowed, and for $W = 3.6\Lambda$ three defect bands appear. Defect bands appear to break away from the continuum of modes at the top of the cladding bandgap. For the width $W = 0.8\Lambda$ the discrete band covers only a narrow frequency interval, and consequently the waveguide only supports guidance for a small bandwidth. As the width of the waveguide increases the discrete bands approach the dispersion relation of free space shown as the light line $\Lambda/\lambda = k\Lambda/2\pi$ in Fig. 7.2. This results in waveguides that support guidance over a large bandwidth. For very large widths W, however, the waveguide will be multi-moded (more than one guided mode at the same frequency). Although three defect bands exist for the waveguide of width $W = 3.6\Lambda$, there is a frequency interval with only one defect band, and consequently single-mode guidance of light is possible for frequencies within this interval ($\Lambda/\lambda < 0.29$). A similar observation is valid for $W = 2.1\Lambda$, for which single mode operation is possible for $\Lambda/\lambda < 0.41$ although two defect bands are present within the cladding bandgap.

A clearer picture of the single-mode/multi-mode behavior can be obtained by considering Fig. 7.3, where the number of modes localized to the line defect is shown as a function of the waveguide width and the frequency. The number assigned to different areas in the $(\Lambda/\lambda, W/\Lambda)$ plot represents

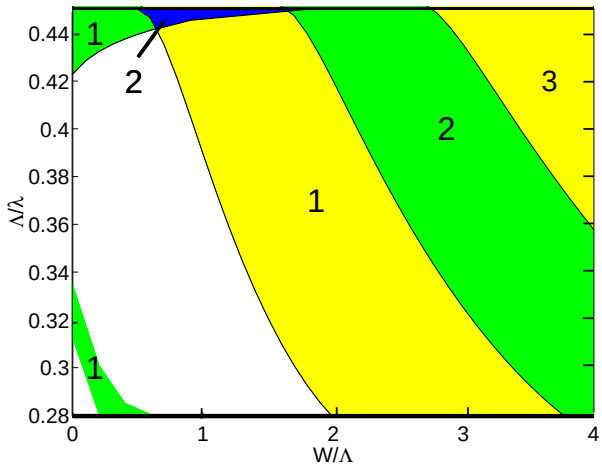

Figure 7.3: Number of guided modes in the straight triangular-lattice photonic crystal waveguide (first orientation) as a function of the waveguide width and the frequency.

the number of guided modes as a function of normalized width W/Λ be-

tween 0 and 4, and as a function of normalized frequency in the bandgap of the photonic crystal cladding. The number of modes observed varies between zero and three. For widths larger than approximately 3.8Λ, there are no frequency intervals within which only one defect mode is guided by the line defect. It appears that single-mode guidance is only possible for waveguide widths being on the order of, or smaller than, a free-space wavelength. The white area represents a region in the bandgap of the cladding where no guided modes are allowed. Note that the domain with two guided modes for $W < 1.8\Lambda$ is not due to two separate defect bands overlapping in frequency. It is the same defect band that covers the same frequency for two different Bloch wave numbers. This is illustrated by considering the defect band for $W = 0.8\Lambda$ in Fig. 7.2, where there may be two allowed values for $k\Lambda/2\pi$ for the same frequency Λ/λ.

Consider the defect band corresponding to $W = 1.2\Lambda$ in Fig. 7.2. Modes corresponding to different $(\Lambda/\lambda, k\Lambda/2\pi)$ solutions on this defect band may behave quite differently in terms of their flow of energy in the waveguide. Fig. 7.4 shows the real part of the complex Poynting vector, $\mathbf{P} = \mathbf{E} \times \mathbf{H}^*$, for $k\Lambda/2\pi = 0.100$, where $\mathbf{E} = \frac{1}{i\omega\varepsilon(\mathbf{r})\varepsilon_0}\nabla \times \mathbf{H}$, $i = \sqrt{-1}$, * denotes complex conjugation, and ε_0 is the vacuum permittivity. The inset shows an example

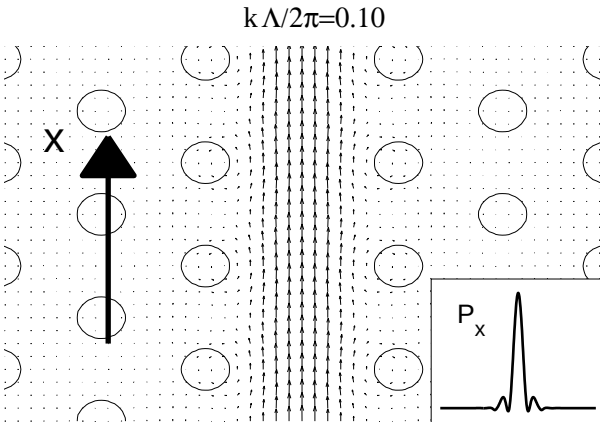

Figure 7.4: The real part of the complex Poynting vector $\mathbf{P} = \mathbf{E} \times \mathbf{H}^*$ for a guided Bloch mode, where the Bloch wave number k is given by $k\Lambda/2\pi = 0.10$. The inset shows an example of the x component of the Poynting vector across the waveguide.

of the x component of the Poynting vector. The figure shows that the energy flows primarily in the x direction. The inset for the Poynting vector profile

resembles to some extent the Gaussian-like profile found for the fundamental mode in e.g. a slab waveguide.

The energy flow picture changes dramatically when $k\Lambda/2\pi$ is chosen closer to 0.5. For both cases $k\Lambda/2\pi = 0$ and $k\Lambda/2\pi = 0.5$ no energy is allowed to propagate, and in these two limits light is localized but there is no net flow of energy along the waveguide. The situation for $k\Lambda/2\pi = 0.450$ is illustrated in Fig. 7.5. The inset shows an example of the x component of

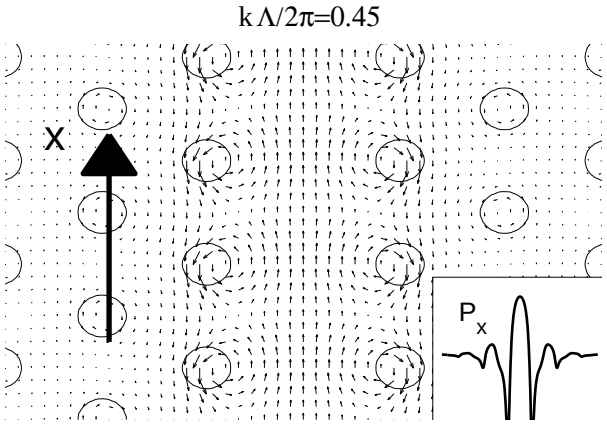

Figure 7.5: The real part of the complex Poynting vector $\mathbf{P} = \mathbf{E} \times \mathbf{H}^*$ for a guided Bloch mode with wave number k given by $k\Lambda/2\pi = 0.45$. The inset shows an example of the x component of the Poynting vector across the waveguide.

the Poynting vector across the waveguide. The figure indicates that energy is no longer flowing primarily in the x direction, and vortices of energy flow appear near the dielectric rods, i.e. energy moves circularly near the dielectric rods closest to the waveguiding region, and energy appears to be coupled backwards. The net energy flow is practically zero across the waveguide section.

The energy flow profile observed in Fig. 7.5 is very different from energy flow profiles of more conventional optical waveguides such as optical fibers and planar ridge waveguides. In those waveguides there are no large scattering objects along the waveguide (such as dielectric rods) that can e.g. result in vortices in the energy flow.

For $W = 3.6\Lambda$ there are three defect bands (see Fig. 7.2). Poynting vector plots for three defect modes belonging to three different defect bands are shown in Fig. 7.6 for low values of $k\Lambda/2\pi$ on each individual defect

band. For all three cases the energy flows primarily in the x direction. The

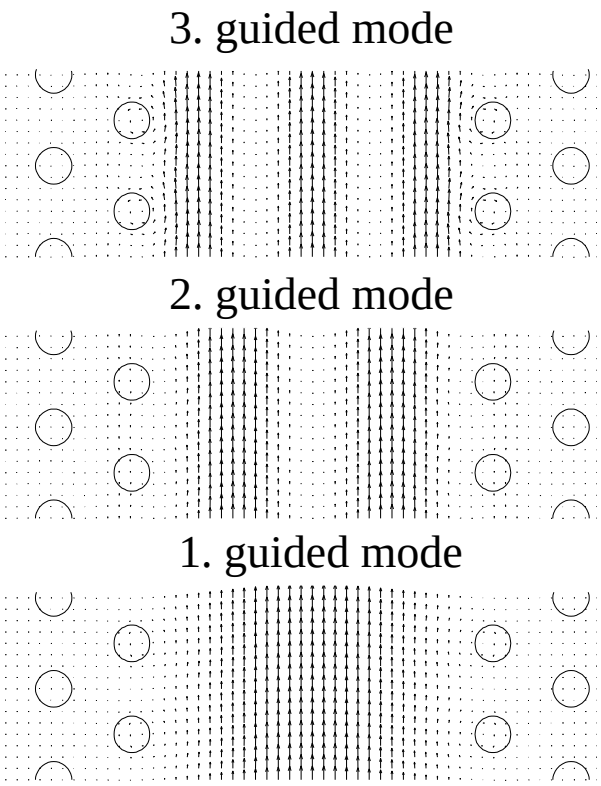

Figure 7.6: The real part of the complex Poynting vector $\mathbf{P} = \mathbf{E} \times \mathbf{H}^*$ for the first-order, second-order and third-order guided modes in the photonic crystal waveguide. $W = 3.6\Lambda$.

profiles indicate that the pattern of the modes resembles that of standing waves along the y axis, which is what could have been expected for modes guided between two parallel metallic plates. In this case the photonic crystal material on either side of the waveguide acts similarly to metallic reflectors for microwave frequencies. A key difference between the PCW and a metallic parallel plate waveguide is that whereas a metallic parallel plate waveguide has a lower cutoff-frequency, a photonic crystal line defect waveguide may have both a lower and a higher cutoff-frequency. This difference means that in photonic crystal line defect waveguides both strong positive and strong negative dispersion are possible.

The effective energy propagation velocity v relative to the vacuum speed of light c may be determined as the time average net energy flow in the x

direction through a line parallel to the y-axis divided by the time and space average energy storage [51], i.e.

$$\frac{v}{c} = \frac{\int_{y=-\infty}^{+\infty} P_x dy}{\frac{1}{\Lambda}\int_{y=-\infty}^{+\infty}\int_{x=0}^{\Lambda} \varepsilon_0\varepsilon_r(\mathbf{r}) \mid \mathbf{E} \mid^2 + \mu_0 \mid \mathbf{H} \mid^2 dxdy}. \tag{7.3}$$

Note that $\int_{-\infty}^{+\infty} P_x(x,y)dy$ is independent of x (which has been checked numerically). A calculation of this velocity is shown in Fig. 7.7 for two choices of the waveguide width W. The circles and crosses on the smooth curves show results for the flow velocity obtained by use of Eq. (7.3), whereas the smooth curves were obtained by calculating $d\omega/dk$, i.e., the smooth curves may be obtained directly from the slope of the defect bands shown in Fig. 7.2. The narrow waveguide with $W = 1.2\Lambda$ has only one defect band

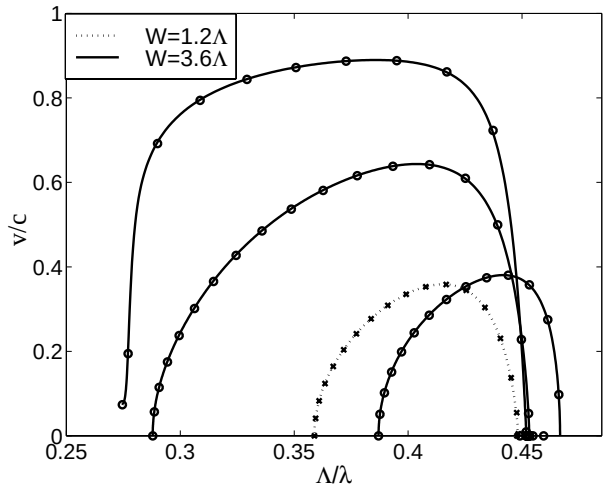

Figure 7.7: Energy propagation velocity for guided modes in the two-dimensional photonic crystal waveguide for two choices of the waveguide width W. The smooth curves were obtained directly from the dispersion relations by calculating $d\omega/dk$, whereas the discrete points were obtained using equation (7.3).

(see Fig. 7.2). Its band frequency edges are seen at the two edges of the dashed curve, where the energy propagation velocity drops to zero. From the lower band edge the velocity increases with frequency, whereas the velocity decreases with frequency closer to the higher band edge. Consequently, both strong positive and negative dispersion are possible. Furthermore, there is a frequency where the slope of the dashed curve is zero, indicating that

zero dispersion is possible around the center frequency with the maximal effective flow velocity $v/c \approx 0.36$ for this defect band. The wider waveguide with $W = 3.6\Lambda$ has three defect bands (see Fig. 7.2). The third-order band ($0.39 < \Lambda/\lambda < 0.465$) is breaking away from the continuum of cladding modes (from higher frequencies to lower ones) with a maximal effective flow velocity of $v/c \approx 0.38$ for this band in the bandgap of the cladding (this third order defect band does not have all its spectrum inside the complete TM bandgap). The second-order defect band ($0.29 < \Lambda/\lambda < 0.45$) is wider and is inside the bandgap of the cladding. More modes have small dispersion in this band than what was the case for the third-order band. The maximal effective flow velocity for this band is $v/c \approx 0.63$. The first-order band has a dispersion relation that approaches that of free-space propagation. It is the widest of the three defect bands for $W = 3.6\Lambda$, and more modes have small dispersion compared to the higher-order bands. The maximal effective flow velocity for the first-order band is $v/c \approx 0.87$.

7.3.2 Waveguides with second orientation

Fig. 7.8 shows the banddiagram for the PCW with second orientation for three different waveguide widths W. The waveguide is shown as an inset. The dispersion relations are in this case quite different from those of the previous line defect orientation (see Fig. 7.2). It is important to note that the line defect with the orientation of Fig. 7.8 has a cladding boundary with a $\sqrt{3}\Lambda$ periodicity, whereas the line defect with the orientation of Fig. 7.2 has a cladding boundary with a Λ periodicity. Due to this difference in periodicity the light line is positioned almost entirely below the bandgap in the case of the second orientation. From Fig. 7.8 we observe that only one defect band exists for $W = 0.87\Lambda$, and it appears to be rather flat with a narrow bandwidth. For $W = 1.73\Lambda$ and $W = 2.6\Lambda$ three and five defect bands are allowed, respectively. As W is increased, defect bands appear to break away from the upper cladding bandgap edge at the right, gaining in bandwidth until they detach themselves completely from the upper cladding bandgap edge at the left (in contrary to Fig. 7.2), the normalized frequency of the defect band being a descending function of $k\sqrt{3}\Lambda/2\pi$. The defect bands subsequently have their bandwidths reduced as W is increased further, and they appear flat as they reach the middle of the cladding bandgap. As the defect width increases further, the bandwidth of the defect bands increases once again, and the normalized frequency of the defect band becomes an ascending function of $k\sqrt{3}\Lambda/2\pi$, with defect bands finally reaching the lower edge of the cladding bandgap on the left side of Fig. 7.8. Both negative and

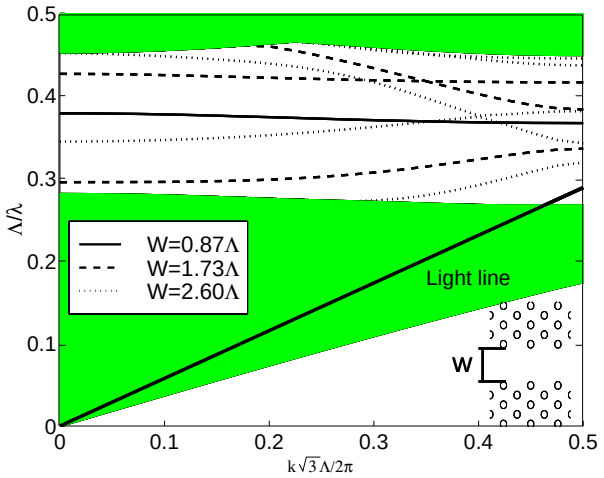

Figure 7.8: Allowed frequencies for TM polarized modes in the straight photonic crystal waveguide (shown as an inset) for three different values of the width W.

positive dispersion are also achievable with this type of waveguide. Note that for the second orientation the defect bands also converge toward the light line as the width W increases. The large difference between defect band dispersion relations for the two waveguide orientations can partly be attributed to the different positions of the light line relative to the bandgap.

Fig. 7.9 shows the number of guided modes in the straight PCW with second orientation as a function of the waveguide width and frequency. A comparison with the previous orientation (see Fig. 7.3) again shows a completely different distribution of guided modes. A comparison between the results for waveguides with first orientation and second orientation shows that the characteristics of PCW's are highly dependent on the orientation of the line defect.

7.4 Conclusion

In conclusion, fundamental research has been presented for the electromagnetic energy flow in planar photonic crystal waveguides designed by introducing a line defect in a photonic crystal material. The photonic crystal consisted of high-refractive-index rods arranged on a triangular lattice in a background of air. Two possible orientations for the line defect in the photonic crystal were considered leading to waveguides with either a long

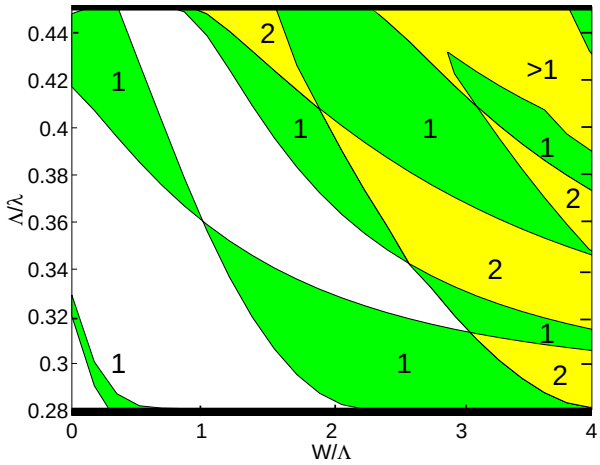

Figure 7.9: Number of guided modes in the straight triangular-lattice photonic crystal waveguide (second orientation) as a function of the waveguide width and the frequency.

or short periodicity in the direction of propagation for guided modes. The energy flow was illustrated for different frequencies by plotting the Poynting vector, and for a frequency with a low energy velocity vortices were observed in the Poynting vector plot. The waveguides may have both a lower and a higher cutoff-frequency for guidance of light, and this results in the possibility of creating waveguides with strong positive, strong negative and zero dispersion. This was illustrated by showing the modal energy velocity versus frequency. Banddiagram calculations were used to investigate how the number of guided modes depends on frequency and waveguide width. The dispersion properties and the number of modes are very different for different orientations of the waveguide in the photonic crystal material.

Chapter 8

Designing leakage-free finite height photonic crystal waveguides

8.1 Introduction

A number of papers in the literature have focused on two-dimensional photonic crystals with dielectric pillars of infinite height or infinitely deep air-holes in a dielectric substrate [18, 19, 132, 133]. The work presented in the previous chapter 7 was for infinite-height or two-dimensional structures. Following the work on two-dimensional structures an important question had to be addressed, namely the question of how to avoid losses due to light leaking out of the waveguides when the waveguide structures have a finite height. This is the question that will be adressed in this chapter. Any realistic realization of a photonic crystal or photonic crystal waveguide (PCW) cannot be of infinite height. Some theoretical papers have addressed the finite height by taking into account in a rigorous way the finite height in realistic photonic crystals [41,149–152] and photonic crystal waveguides [143, 145, 147, 153, 154] in their calculations. The investigations given in the papers [41, 143, 145, 149–154] are based on full-vectorial numerical calculations of electromagnetic waves for three-dimensional structures. Their numerical calculations are very computer-intensive. The approach that will be used in this section to address finite-height PCW's is based on comparing dispersion relations for two-dimensional structures with dispersion relations for the media above and below the finite-height PCW. Compared to the three-dimensional calculations given in Refs. [41, 143, 145, 149–154]

the approach presented in this chapter is not computer-intensive, and it furthermore has the advantage that it can be applied to a large number of diagrams of bandgaps and dispersion relations that are already available in the literature [2, 43, 155–157]. Thereby design guidelines are straightforwardly obtained for a large number of photonic crystal structures. In these approximate considerations we neglect some features of the scattering taking place at the boundaries between the photonic crystal waveguide and the media above and below the waveguide. The scattering here results in coupling between TE and TM polarized electromagnetic modes, and the resulting modes are sometimes referred to instead as TE-like and TM-like [41]. Imperfections at these interfaces may also result in light losses due to scattering. However, for finite-height waveguides without imperfections leakage-free guidance of light is possible (see e.g. Refs. [143, 145, 154]).

In Sec. 8.2 guidelines will be presented for the choice of photonic crystal structure, line-defect effective refractive index, and waveguide orientation, for the design of leakage-free finite-height PCW's. In Sec. 8.3 a method will be given for estimating the appropriate structural parameters of a photonic crystal. The appropriate diameter of air-holes in a photonic crystal with air-holes in silicon is determined depending on the choice of substrate on which the finite-height PCW is placed. A conclusion is given in Sec. 8.4.

8.2 General comments concerning the refractive index of the line defect and the waveguide orientation

Consider the case of a waveguide with first orientation based on silicon rods (dielectric constant $\varepsilon = 12$) in air ($\varepsilon = 1$), where the rod diameter is $D = 0.4\Lambda$ (Λ is the lattice constant). The structure is shown in the inset of Fig. 8.1.

The in-plane TM-banddiagram for the infinite height or two-dimensional PCW is shown for a narrow waveguide with width $W = 0.3\Lambda$ and a wide waveguide with width $W = 2.3\Lambda$ in Fig. 8.1. In the case of the narrow waveguide there is a high concentration of high-refractive-index material in the waveguiding region, whereas the case of a wide waveguide corresponds to a waveguide with primarily low-refractive-index material in the waveguiding region. The two cases are very different which is clear from the behaviour of the defect band dispersion relations in Fig. 8.1.

Consider the same arrangement of dielectric rods, where the rods are now finite-height rods placed on a substrate with the same refractive index

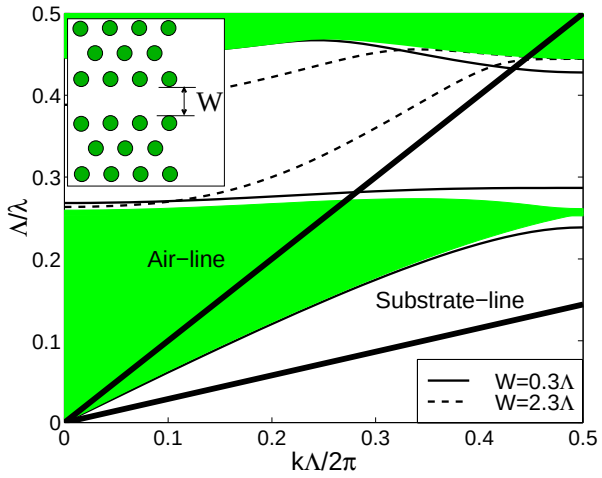

Figure 8.1: TM-banddiagram for a photonic crystal waveguide (first orientation) created by introducing a line-defect in a two-dimensional photonic crystal with dielectric silicon rods arranged on a triangular lattice. The waveguide is shown in the inset. Defect bands are shown for two waveguide widths $W = 0.3\Lambda$ and $W = 2.3\Lambda$, where Λ is the crystal lattice constant.

as the rods. The material above the pillars is assumed to be air. The air-dispersion relation is shown in Fig. 8.1 as the *air-line*. All combinations of Bloch wave number and frequency above the air-line are allowed in free space. Indeed, for the infinite-height waveguide with $W = 0.3\Lambda$ there are guided modes with $(k\Lambda/2\pi, \Lambda/\lambda)$ that are not allowed in free space. For a Bloch wave with a combination of wave vector and frequency below the light line energy cannot leak into the air-region above the finite-height PCW. Light can, however, leak into the air-region when the considered Bloch wave solution has a combination of wave number and frequency above the air-line. This might seem complicated at first, but consider a plane wave propagating in a homogeneous high-refractive-index material being incident on a plane interface between the high-refractive-index material and a material with a lower refrative index. Also in this case total internal reflection of the wave at the interface occurs exactly in the case where the combination of wave vector component parallel to the interface and the mode frequency is not allowed in the low-index material, and when this combination is allowed part of the energy will leak into the material with a lower refractive index. In a similar way, when the finite-height planar PCW is operated below the light line light will be confined vertically without radiation losses by the

mechanism of total internal reflection.

In the case where the rods are placed on a high-refractive-index substrate we should not only consider the air-line but also the corresponding dispersion line for the substrate material. The dispersion line for a substrate material with the same refractive index as the rods is shown as the *substrate-line* in Fig. 8.1, and we note that all allowed combinations of $(k\Lambda/2\pi, \Lambda/\lambda)$ for the infinite-height PCW are also allowed in the high-index substrate. Consequently, the finite-height waveguide may suffer from severe losses due to scattering of light into the substrate. For the narrow width waveguide these losses might be overcome by choosing a low-index substrate. However, for waveguides with large W (the case of $W = 2.3\Lambda$ is shown in Fig. 8.1), where light is confined to an air line-defect, the $(k\Lambda/2\pi, \Lambda/\lambda)$ of the discrete bands tend to stay above the air-line. Several examples of this behaviour was also given for similar structures in chapter 7. Even though the case of rods and light propagating in an air line-defect (large W) is interesting from a physical point of view (the in-plane guidance mechanism is not total internal reflection), the simplest of such finite-height waveguides will not only suffer from severe losses due to scattering into the substrate but also from losses due to scattering into the air-region above the photonic crystal slab. Banddiagrams for waveguides based on creating a wide air line-defect in photonic crystals with rods arranged on a square lattice may be found in Ref. [133], and by including the air-line in these diagrams a similar conclusion is reached. Leakage-free guidance of light in finite height PCW's based on high-refractive-index rods does appear to be possible in the case where the waveguide width is narrow such that the effective refractive index of the waveguiding region is high.

A more natural way to obtain waveguides with a high-refractive-index waveguiding region is to consider waveguides based on photonic crystal structures with air-holes arranged periodically in a high-refractive-index substrate. Waveguides created by introducing a line defect with first and second orientation, respectively, in a photonic crystal with periodically arranged holes in silicon are shown in Fig. 8.2. We will consider the hole-diameter $D = 0.81\Lambda$, where the crystal exhibits a reasonable bandgap for TE polarized light (electric field in the xy plane). A TE-banddiagram for the first orientation waveguide is shown in Fig. 8.3 for the waveguide widths $W = 0.25\Lambda$ and $W = 0.75\Lambda$. The small width $W = 0.25\Lambda$ was chosen to illustrate a situation with a limited number of defect bands. As the width increases to $W = 0.75\Lambda$ the number of defect bands in the bandgap increases, and the bands are also shifted in frequency. Indeed for the discrete bands there are electromagnetic modes with $(k\Lambda/2\pi, \Lambda/\lambda)$ below the air-line, and photonic

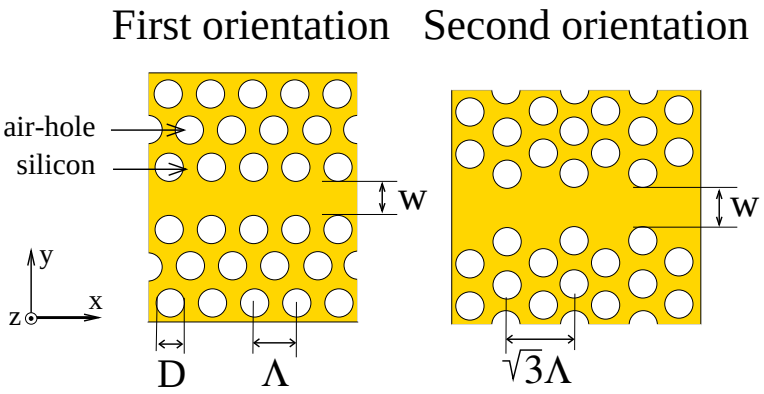

Figure 8.2: The figure illustrates two possible line defect orientations in a photonic crystal with air-holes arranged on a triangular lattice in silicon.

crystal waveguide slabs (as the one reported in [120]) with air above and below the slab may support leakage-free guided modes. A design, where the material below the slab is not air, may be more convenient from a fabrication point of view.

The *substrate2-line* in Fig. 8.3 corresponds to the dispersion line of a substrate which is homogeneous silica (refractive index 1.45). Wafers of high quality with a layer of silicon on top of silica are available commercially. The remaining task in making the waveguides is to etch the air-holes. Clearly, in this case leakage-free guidance of light cannot be obtained over the whole frequency range of the TE-bandgap. The substrate2-line hits the edge of the banddiagram at the normalized frequency $\Lambda/\lambda = 0.5/1.45 = 0.345$, and the requirement of staying below the substrate2-line can only be fulfilled below this frequency limit. We will refer to the limit $\Lambda/\lambda = 0.345$ as the *silica limit*. The corresponding limit $\Lambda/\lambda = 0.5$ for the case of air above and below the finite-height PCW will be referred to as the *air-limit*. In Ref. [121], measurements were carried out for this type of waveguide (substrate 2 below the silicon slab and air above) using normalized frequencies $\Lambda/\lambda > 0.5$, and high losses were observed. High losses are in agreement with the fact that frequencies $\Lambda/\lambda > 0.5$ are above the air-line (and certainly above the substrate2-line).

Alternatively, the holes in the silicon layer might extend further into the silica substrate. The *substrate1-line* in Fig. 8.3 represents the lowest allowed frequency for a given k in a silica photonic-crystal-substrate, which is similar to the infinite-height PCW with first orientation in Fig. 8.2 with the exception that the silicon should be replaced by silica (dielectric constant

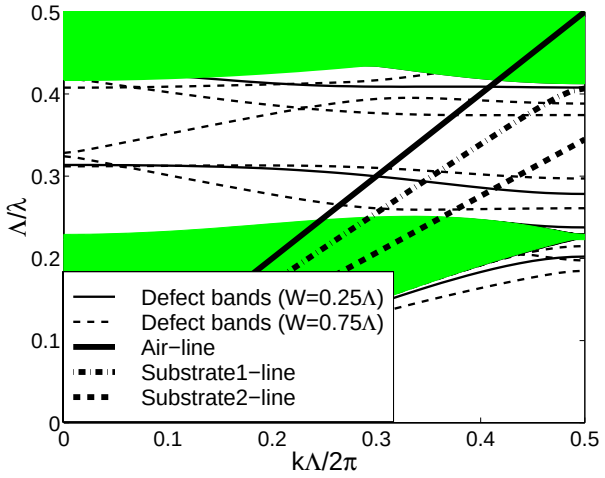

Figure 8.3: TE-banddiagram for a photonic crystal waveguide created by introducing a line-defect (first orientation) in a two-dimensional crystal with air-holes arranged on a triangular lattice in silicon.

$\varepsilon = 2.1$). The dispersion line for this type of substrate will depend on the width of the waveguide, and for wide waveguides this substrate-line will be close to the substrate2-line. However, for relatively narrow waveguides and large holes the presence of air-holes in the silica material will effectively lower the refractive index. The substrate1-line shown in Fig. 8.3 corresponds to the width $W = 0.25\Lambda$ and is positioned mid between the air-line and the substrate2-line. In this case leakage-free guidance of light is possible for practically the whole frequency range of the TE-bandgap, but the available range of k-vectors is still rather restricted near the upper frequency of the substrate1-line.

A TE-banddiagram for the case of second line-defect orientation (width $W = 0.2\Lambda$) is shown in Figure 8.4. The important observation in this case is that since the crystal periodicity for second orientation is larger than for first orientation the available k-space is consequently smaller. The air-line therefore hits the edge of the banddiagram at a frequency which is a factor $\sqrt{3}$ lower compared to the case of a waveguide with first orientation. The upper frequency limit for leakage-free guidance is thereby reduced to $\Lambda/\lambda = 0.5/\sqrt{3} = 0.29$. The range of frequencies where leakage-free guidance can be obtained is therefore much more restricted for waveguides with second orientation as compared to waveguides with first orientation.

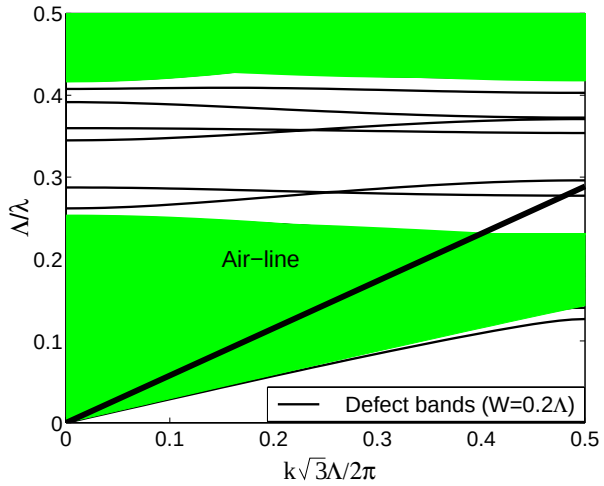

Figure 8.4: TE-banddiagram for a photonic crystal waveguide created by introducing a line-defect (second orientation) in a two-dimensional crystal with air-holes arranged on a triangular lattice in silicon.

8.3 Guideline for photonic crystal structural parameters

In this section we will obtain guidelines for the hole-diameter D and lattice constant Λ of the finite-height PCW based on air-holes in silicon (see Fig. 8.2). An appropriate choice of parameters will be determined by introducing fundamental upper frequency limits for leakage-free guidance of light in diagrams of bandgaps versus structure parameters for the two-dimensional photonic crystal. Although we consider a specific photonic crystal the approach used to estimate appropriate structure parameters is general and can be applied to a large number of diagrams of band gaps versus structure parameters that are already available in the literature [2, 43, 155–157]. In this way design guidelines can be straightforwardly obtained for a wide range of photonic crystal structures.

From the discussions above we have learned that there is a fundamental upper frequency limit for leakage-free guidance of light in finite-height PCW's, and the frequency limit depends on the choice of media above and below the finite-height PCW. For the case of a finite-height PCW suspended in air the upper frequency limit, which will be referred to as the *air-limit*, is $\Lambda/\lambda = 0.5$, where Λ is the periodicity of the structure in the direction of the waveguide. If the finite height PCW is placed on a silica substrate we

instead have to consider the *silica limit* $\Lambda/\lambda = 0.345$. If the air-holes penetrate the silica substrate we can have a somewhat higher upper frequency limit particularly for narrow waveguides as was shown in Sec. 8.2.

In Fig. 8.5 we have introduced the *air limit* and *silica limit* in a diagram of TE and TM bandgaps versus hole diameter D for the photonic crystal with air-holes arranged on a triangular lattice in silicon. The bandgaps have been calculated for in-plane propagation in an infinite-height or two-dimensional photonic crystal. The bandgaps shown in Fig. 8.5 are complete bandgaps

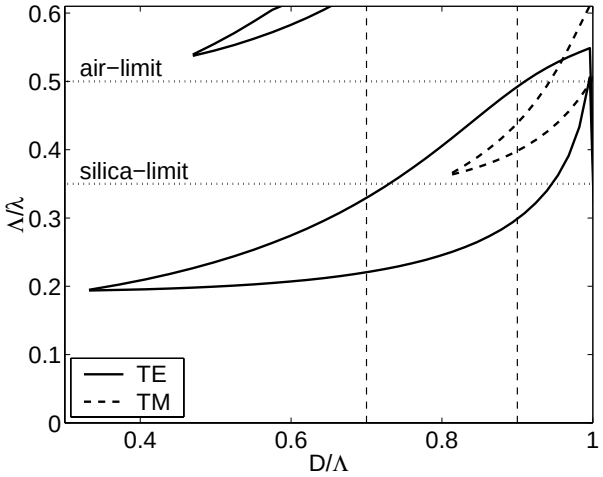

Figure 8.5: The figure shows in-plane TE and TM photonic bandgaps as a function of the diameter D of the air-holes in a two-dimensional photonic crystal with air-holes arranged on a triangular lattice in silicon. Λ is the crystal lattice constant, and λ is the free-space wavelength. Two limiting frequencies are introduced, namely the air-limit and silica-limit, above which leakage-free guidance of light is not possible for finite-height waveguides surrounded by air and silica, respectively.

in the sense that in-plane propagation in the photonic crystal structure is not allowed for any direction for the TE or the TM polarization. Bandgaps for TE polarized light are shown with solid lines and the bandgap for TM polarized light is shown with a dashed line.

Confinement of light to a PCW by use of a complete photonic bandgap requires that the hole diameter D and lattice constant Λ are chosen in such a way that a bandgap is available for the photonic crystal at the wavelength of interest λ. Obtaining leakage-free guidance of light requires that the PCW must also be operated at frequencies below the air-limit, silica-limit or other

equivalent limits depending on the choice of media above and below the finite-height structure.

From Fig. 8.5 it is clear that for finite-height PCW's only the TE-bandgap can be below the silica-limit, and therefore leakage-free bandgap guidance of light will only be possible for one polarisation when the PCW is placed on a silica substrate. For the case of a slab suspended in air it is, however, possible to choose the diameter of the air-holes so large that a bandgap for both polarisations exist below the air-limit, and in this case leakage-free guidance of light may be possible for two polarisations of the light. The bandgaps tend to move up in frequency as D/Λ increases, and if D/Λ is chosen too large the bandgaps will no longer be below the silica-limit. On the other hand, if D/Λ is chosen too small there is no bandgap. For a finite-height PCW placed on a silica-substrate a good choice of D/Λ between these extremes corresponds to obtaining the largest possible photonic bandgap below the silica-limit, and in the present case the ratio $D/\Lambda = 0.7$ is a reasonable choice. An operating frequency near the center of the bandgap is in this case $\Lambda/\lambda = 0.27$. For the optical wavelength 1550nm this results in the lattice constant Λ=419nm and the hole diameter D=293nm.

For PCW's suspended in air we may attempt to use larger air-holes given by for example $D/\Lambda = 0.9$, and in this case we may consider making use of both polarisations of the light for waveguiding using the photonic bandgap effect.

From Fig. 8.5 we may conclude that for finite-height waveguides placed on a silica substrate leakage-free guidance of TM polarized light is not possible using a complete TM bandgap. However, a closer analysis of the band-structure for TM polarisation reveals the existence of a large incomplete TM bandgap that might be used for guidance of TM polarized light. The continuum of modes for TM polarized light in the photonic crystal with $D = 0.9\Lambda$ is shown in Fig. 8.6. In Fig. 8.6 an omni-directional bandgap is seen for normalized frequencies in the range Λ/λ=0.4 to 0.45, and an almost complete bandgap is seen around the frequency Λ/λ=0.28. If the finite-height PCW is suspended in air we can make use of both types of bandgap since both these bandgaps are found below the air-line. However, if the waveguide slab is placed on silica we see that we can no longer obtain leakage-free guidance of light using the complete bandgap (it is above the silica-line), and in this case the almost complete bandgap (it is below the silica-line) gives the only possibility of leakage-free bandgap guidance of TM polarized light. The existence and usefulness of almost complete bandgaps for guidance of light in PCW's has previously been overlooked. This type of bandgaps may open up for bandgap guidance of light for polarizations

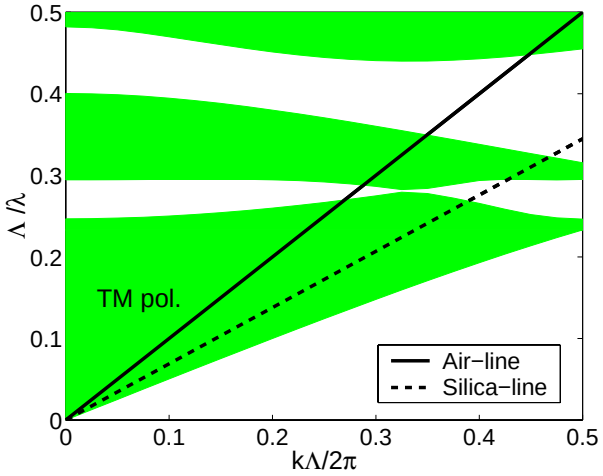

Figure 8.6: Omni-directional and almost omni-directional in-plane photonic bandgaps for TM-polarized light. The air-line represents the dispersion relation for light in free-space. The silica-line represents the corresponding dispersion line for light in silica.

and frequency ranges that would not even be considered from an analysis restricted to only complete photonic bandgaps. In Fig. 8.7 an example is given for dispersion relations of TM polarized guided modes in the planar PCW with combinations of wave number and frequency within the almost complete TM bandgap. The example illustrates that it is possible to obtain guidance by use of incomplete bandgaps.

8.4 Conclusion

In conclusion, a range of guidelines have been presented for the design of leakage-free finite-height planar PCW's. The design guidelines were obtained by comparing calculations for two-dimensional or infinite-height structures with the dispersion relations for the media above and below the finite-height structure. The approach can be applied to a large number of diagrams already available in the literature giving straightforward design guidelines for a large number of finite-height planar PCW's.

The first type of waveguides investigated was based on introducing a line defect in a photonic crystal with high-refractive-index rods arranged on a triangular lattice in air. In the case of a large air line-defect in the photonic crystal the dispersion relations for guided modes in the two-dimensional

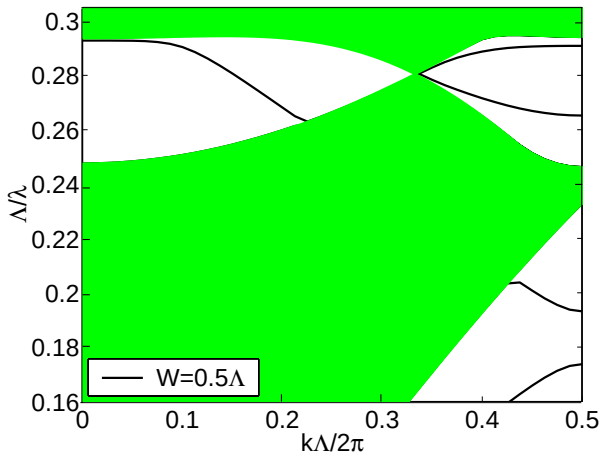

Figure 8.7: Dispersion relations (TM polarisation) for the first orientation photonic crystal waveguide based on a photonic crystal with air-holes arranged on a triangular lattice in silicon. The width of the waveguide is $W = 0.5\Lambda$ and the air-hole diameter is $D = 0.9\Lambda$.

calculation tend to stay above the air-line, and consequently we can expect that the finite height waveguide will be leaky. In the case of waveguides with a high concentration of high-refractive-index material in the waveguiding region part of the dispersion relations of guided modes are found below the air-line, and leakage-free guidance is possible for a waveguide based on rods when the material above and below the finite-height rods has a sufficiently low refractive index.

A more natural approach to obtain PCW's with a high concentration of high-refractive-index material in the waveguiding region is to use photonic crystals with air-holes arranged on e.g. a triangular lattice in a high-refractive-index material such as silicon. A waveguide based on this type of photonic crystal might be suspended in free space or it may be placed on e.g. a silica substrate. The higher the effective index of the substrate the more restricted is the range of frequencies where leakage-free guidance of light is possible. It is therefore advantageous when using a silica substrate that the air-holes in the photonic crystal also extend into the silica substrate in order to lower the effective substrate index.

An example was given that illustrated that line defects should be introduced along directions with short spatial periodicity. A large periodicity in real space results in a small available reciprocal space for the Bloch wave number, which further results in a severely limited useful range of frequen-

cies because for e.g. free space the largest useful frequency is proportional to the largest Bloch wave number within the 1. Brillouin zone.

By introducing fundamental upper frequency limits in a diagram of bandgaps versus the hole-diameter for holes arranged on a triangular lattice in silicon it was possible to evaluate the proper choice of hole-diameters depending on the media above and below the finite-height waveguides. For the photonic crystal with air-holes arranged on a triangular lattice in silicon the existence of an omni-directional bandgap for both polarisations of the light requires air-holes with a large diameter. In this case, however, leakage-free guidance of light by taking advantage of a complete bandgap is not possible with a finite-height version of the investigated PCW's if they are placed on e.g. a silica substrate (the bandgaps have moved to frequencies higher than the fundamental limit related to silica). In this case the finite-height waveguide must be suspended in air to have a medium above and below the waveguide with a sufficiently low refractive index. Waveguides placed on silica supporting leakage-free guidance of light by use of a complete bandgap can, however, be designed for one polarisation of the light, but not for both polarisations, by using a smaller air-hole diameter. Taking advantage of an almost omni-directional bandgap for TM polarisation it is also possible to obtain bandgap guidance of light using both polarizations in the case where the finite height waveguide is placed on silica.

For the interested reader one of the papers (Ref. [139]) on which this section was based contains a further number of dispersion relations for the cases of waveguides with large and small holes arranged in silicon to form photonic crystal waveguides.

Chapter 9

Theoretical analysis of finite-height semiconductor-on-insulator based planar photonic crystal waveguides

9.1 Introduction

In this chapter a specific finite-height photonic crystal waveguide (PCW) design based on the semiconductor-on-insulator (SOI) materials system is theoretically analyzed. Modelling of the guidance properties of this finite-height PCW is interesting because the PCW has been experimentally fabricated and to some extent characterized [119, 130]. This opens up for a comparison between theoretical and experimental work on finite-height PCW's. In this chapter the theoretical work for the PCW will be presented. The theoretically predicted frequency ranges for leakage-free guidance of light are in agreement with recent experimental observations [130, 146].

In the SOI materials system a slab of silicon is placed on top of silica. By etching air-holes in the silicon layer and possibly etching further into the silica a finite-height PCW may be created. The structure can furthermore be made more symmetric by using thermal oxidation to convert part of the silicon into silica such that a layer of silica is found both above and below the finite-height PCW. Waveguides where one seeks to confine light by use of a

similar vertical index step have been explored experimentally by Tokushima, Chow and Notomi [121, 128, 129].

We have previously in chapter 8 developed a technique for obtaining design guidelines for finite-height PCW's, where the guidelines are based on two-dimensional calculations [138, 139]. In section 9.2 this technique is used for obtaining design guidelines for the photonic crystal waveguide based on the SOI materials system. Three-dimensional calculations are given in section 9.3 for the dispersion relations and field profiles. The three-dimensional analysis is compared to the two-dimensional calculations. The consequences on confinement of light due to the waveguide design being vertically asymmetric are obtained from an analysis of the vertical confinement of the electromagnetic mode fields. The conclusion is presented in section 9.4.

9.2 Design guidelines based on two-dimensional calculations

In this section design guidelines will be given for the photonic crystal waveguide illustrated in Fig. 9.1. The structure of interest is the finite-height waveguide shown in Fig. 9.1(b). All calculations presented in this section will, however, be for the two-dimensional structure shown in Fig. 9.1(a). Design guidelines are obtained for the finite-height structure by comparing the two-dimensional calculations with dispersion relations for the media above and below the finite-height waveguide structure.

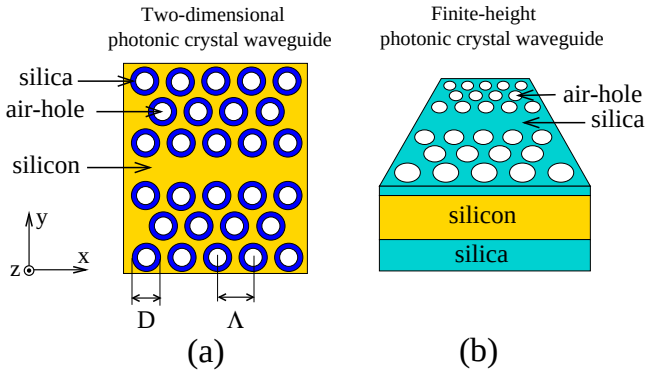

Figure 9.1: Illustration of (a) two-dimensional planar photonic crystal waveguide, and (b) the finite-height planar photonic crystal waveguide.

Consider the two-dimensional PCW shown in Fig. 9.1(a), where air-holes are arranged on a triangular lattice in silicon (dielectric constant 12). We will

further assume that there is a layer of silica (dielectric constant 2.1) on the inside of the walls of the air-holes with a thickness of 0.125Λ, where Λ is the lattice constant of the photonic crystal material. A linedefect or a waveguide has been created in the photonic crystal material by removing a row of air-holes. The banddiagram in Fig. 9.2 shows the allowed combinations of Bloch

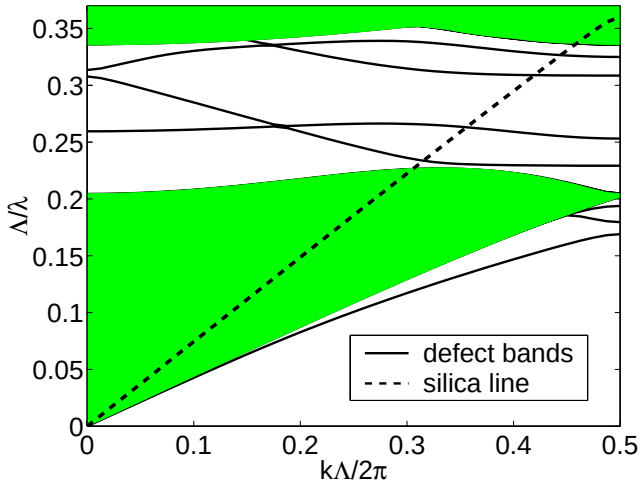

Figure 9.2: Banddiagram for the two-dimensional planar photonic crystal waveguide.

wave number and frequency for TE-polarized light for a waveguide with the size of holes given by $D = 0.75\Lambda$. A bandgap in the continuum of modes related to the photonic crystal material surrounding the waveguide exists for the frequency range from Λ/λ =0.227 to 0.336.

A real PCW such as the one shown in Fig. 9.1(b) is not a two-dimensional structure, and it is necessary to take into account the effect of a real PCW being a finite-height structure. In the finite-height PCW (Fig. 9.1(b)) a slab of the two-dimensional PCW is placed on silica. The air-holes also extend into the silica. For the experimental structure [119, 130] silica is grown on top of the structure by thermal oxidation. In this process part of the silicon is converted into silica. This makes the structure more symmetric in the vertical dimension. Thermal oxidation also gives the silica on the inside of the air-holes. Information on the finite-height structure can be obtained from the banddiagram Fig. 9.2 by plotting the dispersion curve, the silica-line, for the silica material with air-holes below the slab. All combinations of frequency and wavevector above this line are allowed in the silica material. Consequently, as was described in chapter 8 light can only be confined to the

silicon slab in the vertical dimension if the waveguide structure is operated at a frequency and wave number below the silica line. Fortunately, in our case there are four defect bands or guided modes that are below the silica line, and we can expect that leakage-free guidance of light is possible for the finite-height waveguide design for an appropriately chosen height of the silicon slab.

The position in frequency of the photonic bandgap is important, and this position depends on the size of the air-holes D. Note that the silica line hits the edge of the banddiagram at a normalized frequency of $\Lambda/\lambda = 0.36$, and this frequency may be interpreted as an upper frequency limit for leakage-free bandgap guidance of light. The frequency limit is slightly higher than the *silica limit* in chapter 8 because the air-holes in the silica effectively lowers the refractive index. In this section *silica limit* will refer to the frequency limit $\Lambda/\lambda = 0.36$. By using the fixed value $\Lambda/\lambda = 0.36$ for the silica limit it is ignored that the silica limit varies slightly with D/Λ. In Fig. 9.3 the silica limit has been plotted together with the TE bandgap as a function of the diameter of the holes D, and we can see that a large bandgap below the silica limit can be obtained by choosing $D = 0.75\Lambda$. Note that in the calculation shown in Fig. 9.3 we have taken into account the presence of the layer of glass on the inside of the air-holes with a thickness of 0.125Λ. For structures where there is no layer of glass on the inside of the air-holes

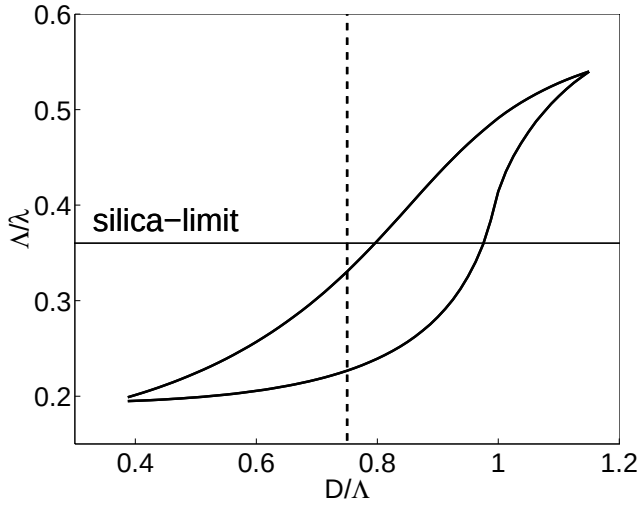

Figure 9.3: TE bandgap for the two-dimensional photonic crystal as a function of the diameter D of the holes in the crystal.

the air-holes would overlap for $D > \Lambda$, and in that case the bandgap for TE-polarized light would break down almost immediately as the hole-diameter becomes $D = \Lambda$ (see e.g. Fig. 8.5). In the present case a bandgap exists for somewhat larger values of D because there is a layer of glass on the inner walls of the holes.

The size of the air-holes D=0.75Λ obtained from the two-dimensional calculations gives a design guideline for the experimental realization of finite-height waveguides.

In order to be able to compare two-dimensional and three-dimensional calculations we have also for the two-dimensional photonic crystal waveguide calculated the amplitude of the magnetic field squared for the four bandgap guided modes at $k\Lambda/2\pi = 0.46$. These field profiles are shown as contour plots in Fig. 9.4.

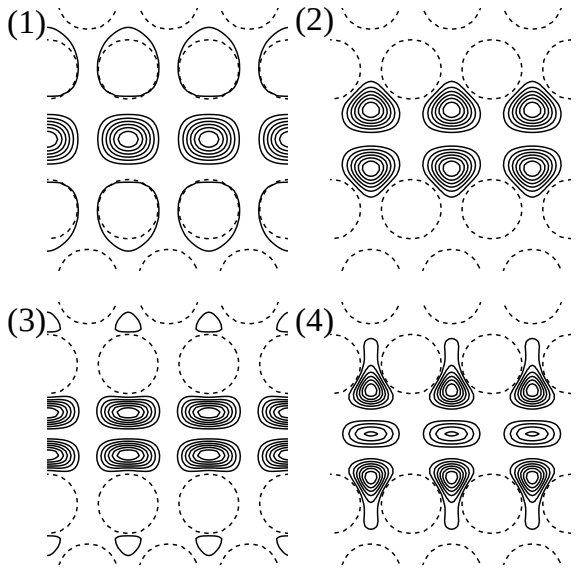

Figure 9.4: Amplitude of magnetic field squared for the four bandgap guided modes in a two-dimensional planar photonic crystal waveguide ($k\Lambda/2\pi = 0.46$).

9.3 Three-dimensional theoretical analysis

In this section the finite-height PCW (Fig. 9.1(b)) is analyzed by three-dimensional calculations. The size of holes, height of silicon slab etc. used for

the theoretical three-dimensional calculations have all been obtained from an experimentally fabricated structure [130]. This leaves no free parameters, and therefore when theory is compared to experimental propagation loss measurements there are no parameters that can be tuned or fitted to obtain a better agreement. The height of the silicon slab is h=0.6Λ (240nm), the size of the holes is D=0.75Λ (300nm), and the thickness of the glass layer on the inside of the holes is 0.125Λ (50nm). The dimensions for the holes and the thickness of the glass layer on the inside of the holes are the same as for the two-dimensional calculations presented in the previous section 9.3.

The banddiagram for the finite-height photonic crystal slab without a linedefect or a waveguide introduced is shown in Fig. 9.5. Here the bandstructure is investigated for those Bloch wave vectors that are on the boundary of the irreducible Brillouin zone shown as an inset in Fig. 9.5. The shaded region is the light cone for the silica material above and below the finite-height photonic crystal slab. All combinations of wavevector and frequency

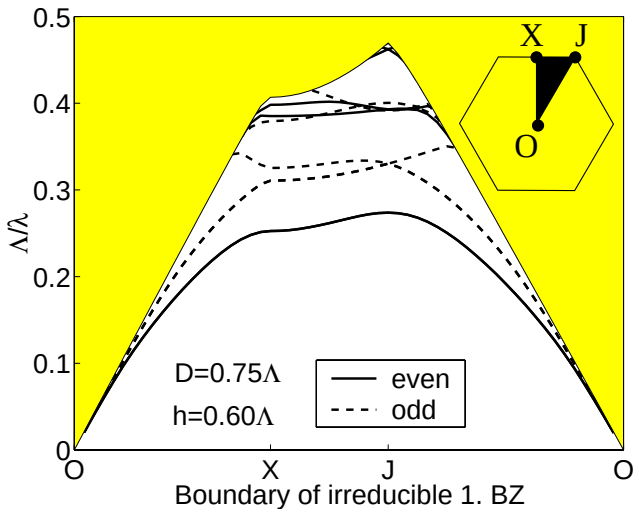

Figure 9.5: Banddiagram for the finite-height photonic crystal slab.

in the shaded region are allowed in the silica material. Confinement of light to the slab requires that we are below the light cone. The modes below the light cone have been divided into even modes (solid lines) and odd modes (dashed lines). In the center plane of the slab the even modes are polarized in the same way as TE modes for two-dimensional photonic crystals (the electric field is in the symmetry plane and the magnetic field is perpendicular to the symmetry plane). The odd modes correspond to TM polarization

for the two-dimensional case. Outside this symmetry plane there is polarization mixing so that in the three-dimensional case we often refer to TE-like modes (even) and TM-like modes (odd) instead of TE and TM as was appropriate in the two-dimensional case. Compared to the two-dimensional bandgap shown in Fig. 9.3 for $D = 0.75\Lambda$ the bandgap has moved up in frequency. For example the lower edge of the TE gap in Fig. 9.3 is app. $0.227\Lambda/\lambda$, and in Fig. 9.5 the lower edge of the gap in even modes is app. $0.274\Lambda/\lambda$. Due to the finite height the fields will be affected by the presence of a material with a lower refractive index above and below the slab. A variational principle can be used to explain that bands and bandgaps move up in frequency in such cases [2].

The three-dimensional dispersion curves for the finite-height PCW are shown in Fig. 9.6. The shaded regions now correspond either to a continuum of modes allowed in the photonic crystal slab surrounding the waveguide or to the continuum of modes allowed in the silica material above and below the waveguide. The diagram is similar to Fig. 9.2 if the region above the

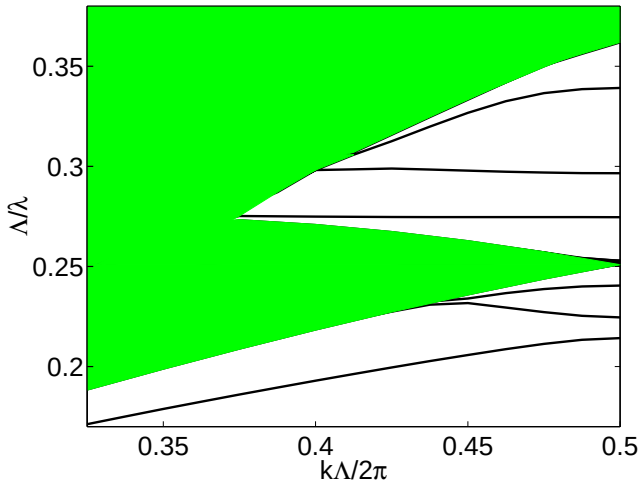

Figure 9.6: Banddiagram for the finite-height photonic crystal waveguide.

silica line is shaded. By comparing with the corresponding two-dimensional calculation Fig. 9.2 we see that there are now only three bandgap guided modes instead of four in the two-dimensional case. The frequencies have also been shifted by on the order of 0.05 in normalized frequency units. The magnetic field squared through the center of the finite-height waveguide is shown for the three bandgap guided modes in Fig. 9.7, and clearly the modes 1 and 2 appear almost identical to the result obtained using two-dimensional

calculations. For the third band, however, some differences are easily seen

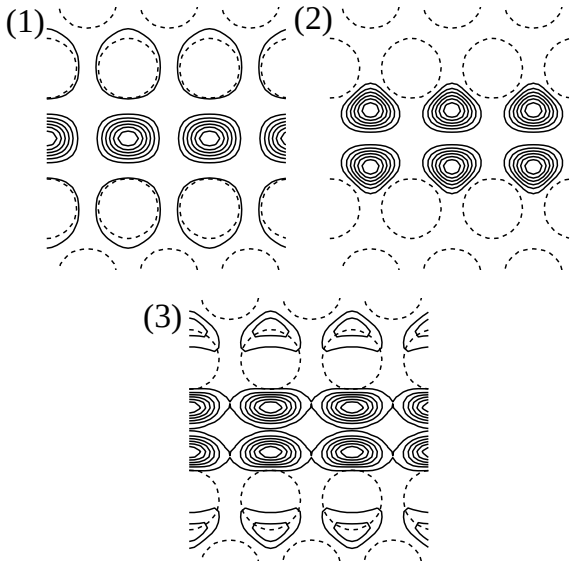

Figure 9.7: Amplitude of magnetic field squared for the three bandgap guided modes in the finite-height photonic crystal waveguide ($k\Lambda/2\pi = 0.46$).

by comparison but the overall symmetry has been maintained. Of course the change in the number of bandgap guided modes from 4 to 3 and the shift in frequency are significant differences between the two-dimensional and three-dimensional analysis. Two-dimensional calculations are useful for making design guidelines and have the advantage of being computationally more manageable. Because of the differences between the two- and three-dimensional calculations, the three-dimensional calculations are necessary when comparing theoretical predictions with experiments to obtain good agreement. Two-dimensional calculations may be sufficient for structures with a low vertical index contrast.

From the banddiagram Fig. 9.6 we will expect low-loss guidance (in theory leakage-free guidance) of light for the frequency ranges covered by the three defect bands related to bandgap guided modes. Recently experimental measurements of propagation losses per unit length have been performed for the finite-height PCW with the same structure parameters as used in the calculations here [130, 146]. Low-loss propagation has been observed for the frequency ranges of the two lowest frequency bands in the bandgap in good agreement with the theoretical prediction. A decrease in the losses was also

observed for the frequency range of the third band in the bandgap. In this case, however, the observed losses are not low.

In order to understand why the measured propagation losses for the third defect band are not low the vertical localization of the fields in the photonic crystal waveguide was analyzed. The localization of the electric field squared is illustrated for the three bands in Fig. 9.8. The fields have been plotted for a plane defined by the waveguide axis and the out-of-plane direction or z direction (see Fig. 9.1). We prefer to use the electric field here instead of the magnetic field because the field for all three bands have high electric field intensity in the center of the waveguide, whereas this is not the case for the magnetic fields (see fig. 9.7).

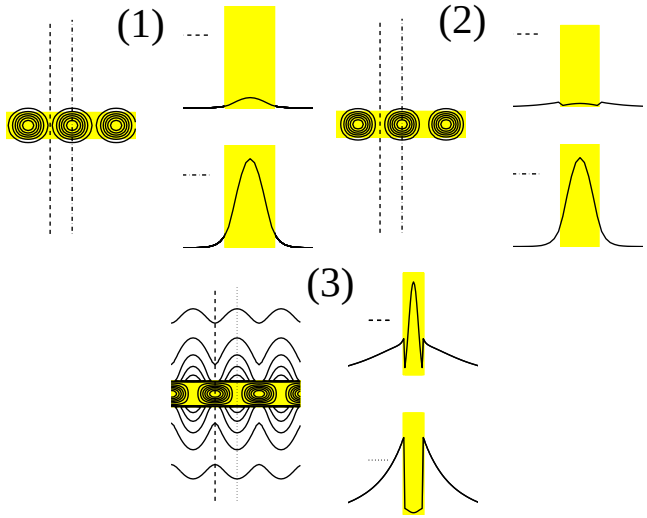

Figure 9.8: Vertical cross section of the amplitude of electric field squared through the center of the finite-height photonic crystal waveguide for the three bandgap guided modes ($k\Lambda/2\pi = 0.46$).

The localization of the first band in the bandgap is illustrated to the left in Fig. 9.8 (at the label (1)). The shaded region indicates the finite-height silicon slab. Outside the shaded region is the silica-material above and below the silicon photonic crystal waveguide slab. From the contour plot we see that the electric field is well localized. The localization is also studied by plotting the field along the dashed line and the dash-dot line, and we see that outside the silicon slab the field decays rapidly. This is also the case for the second band. For the third band, however, the tails of the field extend far into the silica on either side of the silicon slab.

In the theoretical calculation we assume that the silica on either side of the finite-height PCW extends to infinity. It is necessary to assume the structure symmetric in this way because otherwise the bandgap and leakage-free guided modes do not exist in the first place. In the case of vertically symmetric structures the modal solutions can be classified as even modes and odd modes or TE-like and TM-like, and bandgaps and bandgap guided modes can be found for each class of modes separately. For vertically asymmetric structures this classification of the modes into two types with different vertical symmetry is not possible.

For the case of the fields 1 and 2 in Fig. 9.8 we conclude that the silica layer on top of the silicon photonic crystal slab in the experimental structure does not have to be thick compared to the height of the silicon slab. The silica layer on top of the experimental structure has a thickness of app. 50nm, which is roughly 1/5 of the height of the silicon slab. This is barely enough for the fields 1 and 2 to be only weakly affected by the fact that the real experimental structure is not vertically symmetric. The top layer of silica is, however, not thick enough for the case of the field 3 in Fig. 9.8. Thereby we expect that the third band in the bandgap will be stripped off. The theoretical calculations suggest that guidance of light for the frequency range of the third band can be made possible by depositing a thick layer of silica (with air-holes) on top of the structure. This might be worth pursuing because the frequency range covered by the third band is very broad compared to the frequency ranges covered by the bands 1 and 2.

9.4 Conclusion

In conclusion, design guidelines have been obtained for the size of holes in a finite-height two-dimensional photonic crystal waveguide by comparing two-dimensional calculations with dispersion relations for the media surrounding the waveguide. Three-dimensional calculations were compared to the two-dimensional calculations, and we found that the number of guided modes changes, and the frequencies of the modes are shifted. The distributions of the field for three guided modes calculated using two- and three-dimensional calculations were qualitatively similar. The analysis shows that when comparing theory and experimental results three-dimensional calculations are necessary to obtain good agreement. The theoretically predicted frequency ranges, where the waveguide supports guidance of light, are in good agreement with experimental propagation loss measurements for the waveguide [130, 146]. Two out of three calculated frequency ranges coincide

with low measured propagation losses. Poor guidance or high losses for the frequency range of the third calculated band was explained theoretically by evaluating the vertical confinement of light for the bandgap guided modes. The glass layer on top of the experimental structure is presently not thick enough for the structure to support guidance for the third frequency range.

Chapter 10

Large-bandwidth planar photonic crystal waveguides

10.1 Introduction

The dispersion properties of planar photonic crystal waveguides (PCW's) may depend strongly on design parameters such as the size of air-holes in a dielectric material, the width of a waveguide and the type of waveguide [18, 132, 134, 138, 139, 145, 147]. It is important to understand how PCW's can be designed to have desired dispersion properties. The aim in this chapter is to develop the ideas and theory necessary for making PCW's that support leakage-free bandgap guidance of light over large frequency intervals. A two-dimensional analysis is sufficient for understanding some of the physics of planar PCW's. Even the properties of finite-height waveguides can be addressed when two-dimensional calculations are compared with dispersion relations for the media above and below the finite-height waveguides [138]. The two-dimensional approach does not, however, allow the calculation of exact dispersion properties for finite-height structures. The effect of the height of the structure on bandgaps and guided modes is difficult to address by two-dimensional calculations. In this section we will provide a full three-dimensional analysis of large-bandwidth planar PCW's. The three-dimensional analysis allows the calculation of the dispersion properties of a type of realistic finite-height PCW which is within reach with todays fabrication technology. Previous three-dimensional analyses of PCW's that did not focus on obtaining a large bandwidth can be found in Refs. [124, 128, 143, 145, 147, 153, 154].

Obtaining leakage-free guidance of light in planar PCW's requires first of

all a high vertical refractive-index contrast between the finite-height PCW and the media above and below the finite-height structure (see chapter 8). The highest vertical index contrast is achieved when a finite-height PCW is suspended in air. This is the approach that will give the largest frequency range with leakage-free bandgap guidance of light in a planar PCW. In this section we focus on the case of a photonic crystal slab suspended in air. Photonic crystal slabs suspended in air have been investigated experimentally both for making lasers [142] and for making waveguides [120, 123, 127, 143, 144].

The motivation for this work can be understood from the features of a typical banddiagram for finite-height PCW's based on holes in a high-refractive-index material. An example of such a diagram is shown in Fig. 10.1. The waveguide considered is shown as an inset, and consists of a photonic

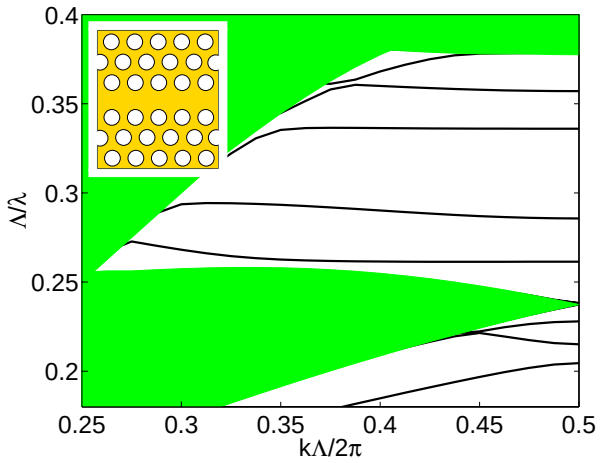

Figure 10.1: Banddiagram for a photonic crystal waveguide based on a silicon slab with air-holes arranged on a triangular lattice. The height of the slab being suspended in air is h=0.76Λ, where Λ is the crystal lattice constant. The diameter of the air-holes is D=0.7Λ. A waveguide has been created by removing a row of air-holes.

crystal structure with air-holes arranged periodically on a triangular lattice in a silicon slab. The diameter of the air-holes is D=0.7Λ, where Λ is the photonic crystal lattice constant. By removing one row of air-holes a line defect or waveguide has been formed. The height of the slab is h=0.76Λ, and we assume that the slab is suspended in air. Because the structure is vertically symmetric it is possible to divide the Bloch mode solutions into two classes of modes that are sometimes referred to as even modes and odd

modes [145]. In the banddiagrams in chapter 10 we consider only the even modes where a complete photonic bandgap exists in the slab modes of the considered finite-height photonic crystal slabs.

Notice the gap in $(\Lambda/\lambda, k\Lambda/2\pi)$-space in the continuum of modes above the frequency $\Lambda/\lambda = 0.26$. In this gap we find a number of discrete dispersion curves corresponding to photonic bandgap guided modes. These bands only cover rather limited frequency intervals and they are flat. The slope of the bands is proportional to the group velocity or energy velocity of the guided modes (see chapter 7), and thereby the flatness of the bands can be interpreted as a very low group velocity. The features concerning the flat bands and the narrow bandwidth of the guided modes that we observe in Fig. 10.1 are common to PCW's with high-refractive-index linedefects. For some applications, e.g. filtering, it may be convenient to have guidance over only narrow frequency intervals. A narrow bandwidth can be achieved to an even larger extent by using coupled cavity PCW's [9, 131, 158, 159]. The aim in this chapter, however, is to design PCW's that support leakage-free guidance of light over large frequency intervals, and preferably single-mode guidance is desired over a large part of the gap.

Previously waveguides based on removing a row of dielectric pillars along a line in a periodic structure of dielectric pillars have also been studied using two-dimensional calculations (see chapter 7 and Refs. [18, 19, 133]). In a two-dimensional analysis where the pillars are assumed infinitely high, and the light is assumed to propagate in the plane of the crystal, a large bandwidth can be obtained. In that case, however, a three-dimensional analysis shows that the waveguides tend to be leaky waveguides. This has been a major reason for instead considering designs such as the one shown in Fig. 10.1 because the high refractive-index contrast between the waveguide slab and the media above and below the slab (in this case free space) is sufficient for providing a guidance mechanism vertically (vertically light is confined by total internal reflection). But as has become clear these waveguides have very different dispersion properties. The designs that will be presented in chapter 10 posses both the vertical confinement of light and the large bandwidth.

The chapter is organized in the following way. In section 10.2 a general design principle is given for making large bandwidth PCW's, and an example is given that illustrates the theoretical idea. In section 10.3 we consider a photonic crystal slab similar to the one in Fig. 10.1 where the line defect will consist of one or more rows of air-holes with various sizes. These large-bandwidth waveguide designs are within reach with todays technology.

10.2 Design principle for obtaining large-bandwidth photonic crystal waveguides

A general design principle is given in this section for making planar photonic crystal waveguides with a large bandwidth. The design principle is based on combining a photonic crystal slab and a slab with appropriate dispersion properties relative to the photonic crystal slab. The design principle will be illustrated in this section for an idealized case. In the forthcoming section examples of large-bandwidth waveguide designs will be given that are within reach with todays fabrication techniques.

The theoretical idea can be illustrated by again looking at the gap in the continuum of modes from Fig. 10.1. This gap is shown in Fig. 10.2 together with the dispersion curve of a slab with the refractive index n=1.5 and the same height (h=0.76Λ) as the photonic crystal slab. Again we assume that

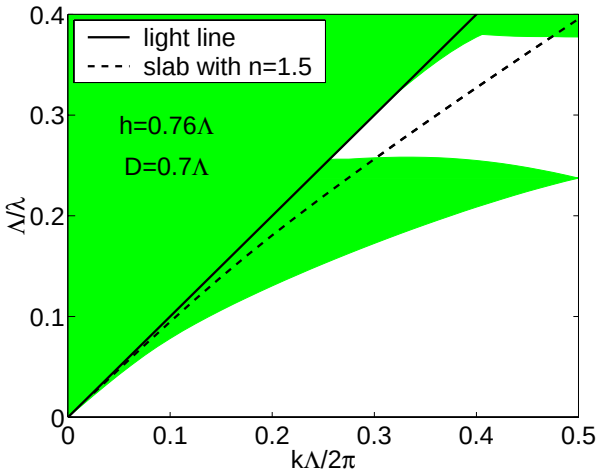

Figure 10.2: Banddiagram for a photonic crystal slab based on a silicon slab with air-holes arranged on a triangular lattice. The height of the slab being suspended in air is h=0.76Λ, where Λ is the crystal lattice constant. The diameter of the air-holes is D=0.7Λ. Also shown is the corresponding dispersion relation for the fundamental mode in a slab with the same height having the refractive index n=1.5.

there is air above and below the slab with refractive index n=1.5. In Fig. 10.2 we also show the free-space dispersion curve known as the light line (which has also been referred to as the air-line in this thesis). Vertical localization of light to the slab requires that the waveguide is operated below the light

line. The refractive index n=1.5 was chosen so that the dispersion curve of the slab with n=1.5 runs through the entire photonic bandgap. We can expect that if we in the photonic crystal slab introduce a wide linedefect region with the refractive index n=1.5 the dispersion curves of the guided modes will to some extent follow the dashed curve in Fig. 10.2, and since this curve runs through the entire bandgap a large bandwidth can be expected. As the line defect increases in width the dispersion curves of guided modes will converge towards the dashed line. Naturally, if the waveguide is made too wide it will become multi-moded, and therefore we will attempt to find a balance between having guidance over a large bandwidth and at the same time have guidance for a single mode only.

A banddiagram for such a waveguide design is shown in Fig. 10.3. The structure is shown as an inset. The size of holes and height of the slab is the

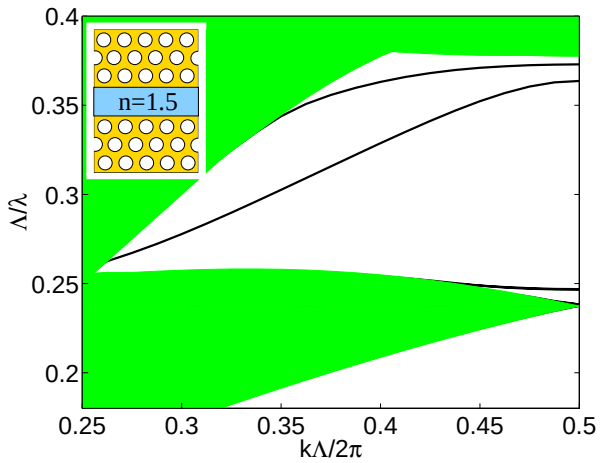

Figure 10.3: Banddiagram for a photonic crystal waveguide based on a silicon slab suspended in air with air-holes arranged on a triangular lattice. A line-defect has been introduced as a slab region with refractive index n=1.5 and width $\sqrt{3}\Lambda$, where Λ is the crystal lattice constant.

same as for Fig. 10.1 and Fig. 10.2. The width of the region with refractive index n=1.5 is $\sqrt{3}\Lambda$. The distance from the edge of the holes to the region with n=1.5 is $(\Lambda - D)/2 = 0.15\Lambda$. In this example we find leakage-free guidance of light for a single mode from the normalized frequency $\Lambda/\lambda \approx 0.26$ to $\Lambda/\lambda \approx 0.34$. This corresponds to app. 60% of the gap. A single guided mode is also found in the interval $\Lambda/\lambda \approx 0.36$ to $\Lambda/\lambda \approx 0.37$. Notice that there are no guided modes below the frequency $\Lambda/\lambda = 0.24$ as is the case for high-refractive index linedefects such as the one considered in Fig. 10.1.

Instead we find a discrete band on the other side of the continuum of photonic crystal slab modes at a frequency slightly below $\Lambda/\lambda = 0.25$. Such a band we commonly find when we are using low-index linedefects and TE polarization. These are signatures of photonic crystal waveguides with line defects having a low effective refractive index.

The design idea employed in this chapter is general. It is not necessary to consider a homogeneous material with refractive index n=1.5. Other materials and microstructures with a dispersion curve that runs through the bandgap of the photonic crystal material can be used. Such a material can for example be a periodic structure with a very large filling fraction of air-holes in a silicon slab. By properly choosing the air-hole filling fraction the effective refractive index may for some frequencies be similar to that of a slab with n=1.5. This idea is pursued in the next section.

10.3 Designs with waveguiding regions consisting of rows of large air-holes

In this section large-bandwidth PCW's based on a silicon-air photonic crystal slab are presented. The waveguide designs are based on introducing a line defect in the photonic crystal slab with one or more rows of large air-holes.

The simplest structure based on using large air-holes is to replace the air-holes along a line in the photonic crystal by larger air-holes. A waveguide structure with a line-defect consisting of one row of large air-holes has previously been considered by Johnson et. al. and Loncar et. al. [145, 147]. As the diameter of those air-holes is increased the effective refractive index of the line-defect region will be lowered. For a sufficiently low, but not too low, effective refractive index we will have a situation similar to that analyzed in section 10.2, with the exception that the width of the waveguide is somewhat limited with only one row of large air-holes. This type of structure is analyzed in Fig. 10.4. Structures with a wider waveguide consisting of two rows and three rows of large air-holes are considered in the figures 10.5-10.6. The insets shows the structure. A line defect consisting of three rows of large air-holes has previously been considered both experimentally and theoretically by Lin et. al. [124].

For the case of one row of large air-holes in Fig. 10.4 we consider three different hole-diameters for the line defect, namely $D_{core} = 0.93\Lambda$, $D_{core} = 0.95\Lambda$ and $D_{core} = 0.97\Lambda$ to illustrate the effect of lowering the effective refractive index of the line defect. We consider the same photonic crystal slab suspended in air as was also considered in Figs. 10.1-10.3. It is only

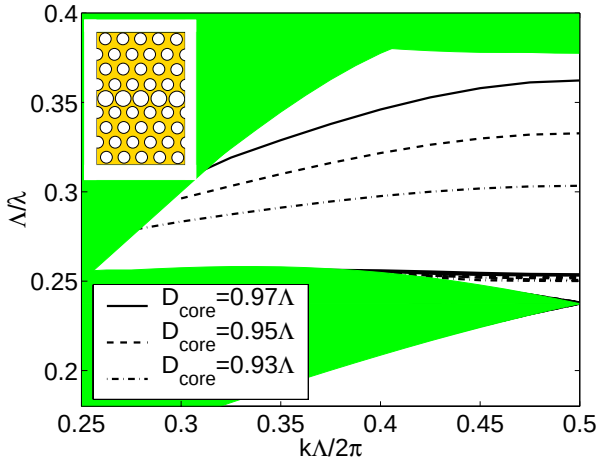

Figure 10.4: Banddiagram for a photonic crystal waveguide based on a silicon slab suspended in air with air-holes arranged on a triangular lattice. The diameter of the photonic crystal air-holes is D=0.7Λ, where Λ is the crystal lattice constant. A line defect has been created by replacing one row of air-holes with larger air-holes having the diameter D_{core}.

the line defect region which is different. Note that to obtain any significant effect the air-holes must be quite large. Also note that the bandstructure is very sensitive to the diameter of the holes. With the largest air-holes ($D_{core} = 0.97\Lambda$) a single guided mode is found from the frequency $\Lambda/\lambda = 0.31$ to $\Lambda/\lambda = 0.36$ which covers 40% of the gap region. This suggests that a reasonably large bandwidth can be obtained with only one row of large air-holes even though the general design idea suggests that the width of the waveguide has to be large. The bandwidth for leakage-free guidance of light achieved by the design shown in Fig. 10.4 is significantly larger compared to the results of Refs. [145, 147], which is in part due to the larger gap in our case.

The idea in our design principle is that the dispersion curves for guided modes will converge towards the dispersion line for the material placed in the line defect when this becomes wide. To explore this further it is natural to show the effect of using not only one row of large air-holes but several rows of large air-holes. In the following three figures we will consider the case of $D_{core} = 0.93\Lambda$. In Fig. 10.5 a linedefect consisting of two rows of large air-holes is considered, and in Fig. 10.6 we consider the case of three rows of large air-holes. Notice how the number of discrete bands in the gap increases with the number of rows of air-holes. For the case of one row the

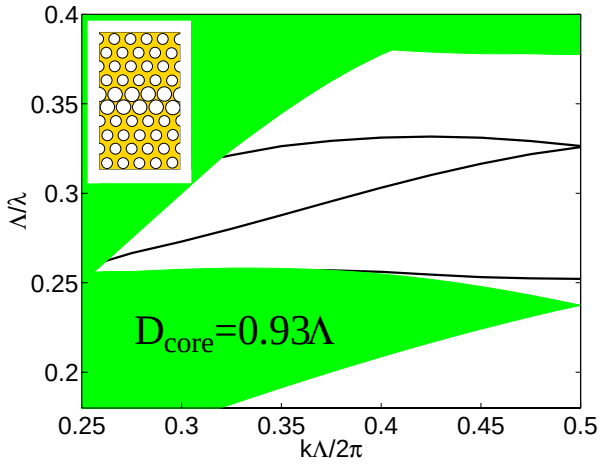

Figure 10.5: Banddiagram for a photonic crystal waveguide based on a silicon slab suspended in air with air-holes arranged on a triangular lattice. The diameter of the photonic crystal air-holes is D=0.7Λ, where Λ is the crystal lattice constant. A line defect has been created by replacing two rows of air-holes with larger air-holes having the diameter D_{core}=0.93Λ.

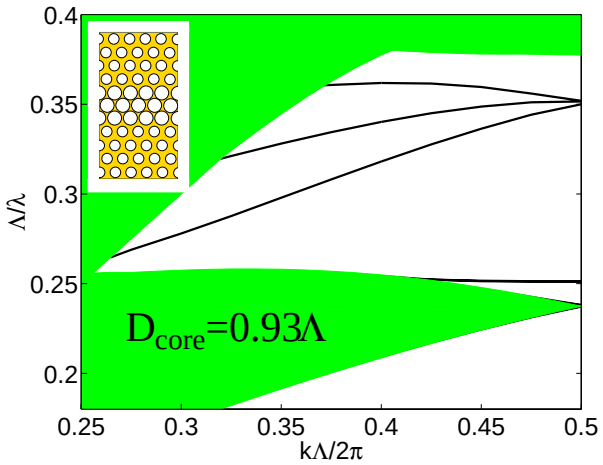

Figure 10.6: Banddiagram for a photonic crystal waveguide based on a silicon slab suspended in air with air-holes arranged on a triangular lattice. The diameter of the photonic crystal air-holes is D=0.7Λ, where Λ is the crystal lattice constant. A line defect has been created by replacing three rows of air-holes with larger air-holes having the diameter D_{core}=0.93Λ.

discrete band was relatively flat, but for the case of two or three rows there are bands with a steep slope covering a significant part of the gap.

The structure of the bands and the degeneracy of the bands at $k\Lambda/2\pi = 0.5$ can be understood by looking at a fully periodic structure with the same size of air-holes that is used in the core region of the waveguide. A banddiagram for a fully periodic structure with air-holes arranged on a triangular lattice in a silicon slab suspended in air is shown in Fig. 10.7. The diameter of the air-holes is D=0.93Λ which is the air-hole diameter of the core holes in the figures 10.5-10.6. The continuum of bands seen in Fig. 10.7 is equivalent to the continuum of bands seen in the figures 10.4-10.6 except that this calculation is for a structure with larger air-holes. The modes above the light line correspond to modes that are not localized to the slab. Only those modes below the light line are guided by the photonic crystal slab. The boundaries of the continuum of slab modes is indicated by a dashed line. Note the behaviour of this continuum at $k\Lambda/2\pi = 0.5$ where it reduces to one point. In the figures 10.5-10.6 guided modes in the gap region also meet at one point at $k\Lambda/2\pi = 0.5$, and this is both the case for two rows of holes and three rows of holes. For the case of three rows of holes the degeneracy frequency at $k\Lambda/2\pi = 0.5$ is 0.35 in both Fig. 10.6 and Fig. 10.7. In this way the guided modes behave similarly to the slab modes of a fully periodic structure, and we can expect that as we increase the number of rows of large air-holes further there will be guided modes that eventually transform into a continuum of modes being the same continuum of modes that we see in Fig. 10.7.

If we for the case of three rows of large holes increase the diameter of the core holes the bands in the gap will cover a larger frequency range, but the frequency range with single-mode guidance may in fact be reduced because the waveguide will become double-moded at an even lower frequency. The waveguide with two rows of large air-holes is in fact single-moded over a slightly larger frequency range compared to the case of three rows. Again this is the case because the waveguide with three rows becomes double-moded at a lower frequency. These examples give an insight into how the guidance properties are related to the properties of the material placed in the line defect region when the line defect region is wide.

10.4 Conclusion

In conclusion, a general design principle has been presented for making planar photonic crystal waveguides that support leakage-free guidance of

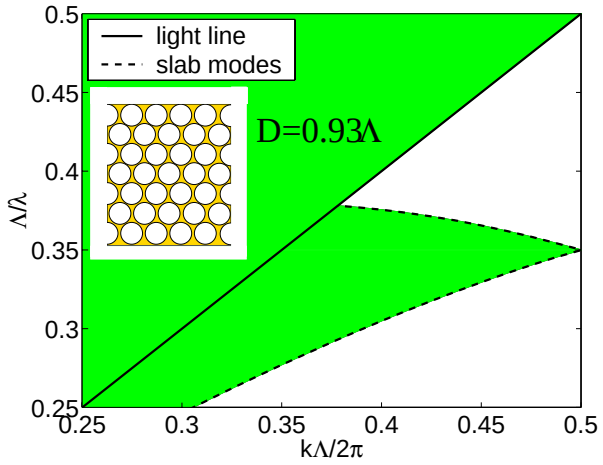

Figure 10.7: Banddiagram for a photonic crystal slab based on a silicon slab with air-holes arranged on a triangular lattice. The height of the slab being suspended in air is h=0.76Λ, where Λ is the crystal lattice constant. The diameter of the air-holes is D=0.93Λ.

light over large frequency intervals. The design idea is to introduce a line defect in a photonic crystal slab where the material in the line defect has appropriate dispersion properties. The dispersion properties are well-known for a dielectric slab, and for a line defect consisting of a slab with refractive index 1.5 we obtained single-mode leakage-free guidance of light over a large frequency range covering at least 60% of the gap in the photonic crystal slab. Another approach to obtain a large bandwidth was also investigated, where the line-defect consisted of a number of rows of large air-holes in silicon.

Chapter 11

Summary

In summary, the work presented in this thesis contributes to two topics within optics of dielectric microstructures, namely, emission of radiation by sources in dielectric microstructures, and planar photonic crystal waveguides.

Concerning the first topic three methods have been presented for calculating spontaneous and classical emission of radiation from sources in dielectric microstructures, and the methods have been applied to various structures including a photonic crystal, a photonic crystal microcavity, the active step-index fiber, and the finite-sized cylindrically symmetric dielectric disk. In the first method spontaneous emission is calculated by use of the Fermi golden rule. In this method a complete set of orthogonal electromagnetic modes is used as a basis for quantization of the electromagnetic radiation field. In a quantum mechanical picture the energy of an electromagnetic mode in the vacuum state (no photons) is not zero. The finite energy in the vacuum state may be interpreted as being due to vacuum fluctuations in the electromagnetic field. The rate of spontaneous emission is proportional to the sum of amplitudes of the electric field squared for each electromagnetic mode normalized to the vacuum state energy. Thereby the rate of spontaneous emission is proportional to the strength of the electric field vacuum fluctuations at the position of the emitter. The electromagnetic modes of the radiation field were calculated by use of plane-wave-expansion theory and a variational principle. Plane-wave-expansion theory is suitable for periodic dielectric structures such as photonic crystals. The method was applied to investigate the spontaneous emission properties of a two-dimensional photonic crystal and a two-dimensional photonic crystal microcavity. The rate of spontaneous emission was found to depend significantly on the position

of the emitter. For the photonic crystal microcavity the rate of spontaneous emission was enhanced for dipole transition frequencies matching the frequencies of localized cavity modes, but only for those positions of the emitter where the field amplitude of the cavity mode is not low.

A general theory has been presented for calculating spontaneous emission from sources in active dielectric microstructures. For the case of dielectric structures with amplifying or absorbing media (active dielectric structures) a complete set of orthogonal electromagnetic modes does not exist. For active dielectric microstructures it is convenient to use the electromagnetic fields and generating currents as primary observables that are defined by their commutation relations. The fields and current operators are related by a classical Green's tensor, and in particular the spontaneous emission can be related to the transverse part of the Green's tensor. A method was presented for constructing the Green's tensor for active structures as a summation over a complete set of biorthogonal electromagnetic modes. The method was exemplified for an active step-index fiber, which is sufficiently simple to allow analytic solutions. For the fiber spontaneous emission was studied with respect to transition frequency, position, and vector orientation of an electric dipole emitter. Far field radiation patterns were studied by use of a Poynting vector approach.

Finally, an integral equation approach has been presented for the emission of radiation by sources in finite-sized dielectric microstructures. In this method a reference system is considered, which could be free space, along with a field solution in the reference system. The reference field solution can be the field emitted by a distribition of current sources in free space. The actual structure of interest corresponds to the reference system which has been changed within a finite-sized spatial region. The integral equation expresses field solutions in the actual structure of interest in terms of the field solution of the reference system. With this method calculations were presented for both near fields and far fields generated by a dipole emitter in the center of a finite-sized dielectric disk. Furthermore, the total rate of emission was studied with respect to the diameter of the disk, and resonances were found for certain disk diameters. The enhancement relative to the rate of emission from a dipole located in free space was on the order of a factor 13.

Concerning the second topic, planar photonic crystal waveguides (PCW's), a collection of results for the theory of PCW's has been presented. The work concerns both getting a fundamental understanding of the electromagnetic properties of PCW's, but does also concern how to design PCW's with desired properties such as large bandwidth and low losses.

The initial theoretical work on PCW's was for the idealized case of two-dimensional or infinite-height photonic crystal structures, where e.g. dielectric rods are infinitely high, or air-holes in a dielectric material are infinitely deep, such that the structures only vary in two dimensions. Fundamental research was presented for the electromagnetic properties of two-dimensional PCW's with designs based on introducing a line defect in a two-dimensional photonic crystal. For waveguides based on a photonic crystal with high-refractive-index rods arranged on a triangular lattice in air an analysis was given for the dispersion properties, the electromagnetic energy flow in terms of energy propagation velocity and Poynting vector distribution, and the number of guided electromagnetic modes versus waveguide width and frequency. These properties were shown to be very different for different orientations of the waveguide in the photonic crystal.

In any real planar photonic crystal waveguide the dielectric rods cannot be infinitely high, and the air holes in a dielectric substrate cannot be infinitely deep. The finite height of real PCW's must be accounted for when designing PCW's that support leakage-free guidance of light. A method has been developed and presented for obtaining guidelines for the design of leakage-free finite-height PCW's by comparing two-dimensional calculations for infinite-height PCW's with dispersion relations for the media above and below the corresponding finite-height PCW. By use of this technique it became clear that PCW's with a large air line-defect tend to be leaky waveguides. It also became clear that it is advantageous to introduce line defects along directions in a photonic crystal with shortest spatial periodicity. The technique furthermore allows making an estimate of relevant design parameters such as the diameter of an air-hole.

For a PCW based on the semiconductor-on-insulator materials system both a two-dimensional and fully three-dimensional theoretical analysis was carried out. In this case the three-dimensional analysis takes into account in a rigorous way the finite height of the photonic crystal. Compared to the two-dimensional analysis the three-dimensional analysis resulted in fewer guided modes, and the guided modes were shifted significantly in frequency. The field distribution of the guided modes in the center plane of the finite-height PCW were, however, qualitatively similar to the field distributions obtained by use of two-dimensional calculations. Three-dimensional calculations may be necessary to obtain good agreement between experiments and theoretical results. Two out of three theoretically predicted frequency ranges with leakage-free guidance of light coincide with low measured propagation losses [130, 146]. High losses for the third frequency range was explained theoretically by investigating the vertical or out-of-plane field confinement

of the bandgap guided modes. This led us to the conclusion that a glass layer on top of the experimental structure is presently not thick enough for the structure to support guidance for the third frequency range.

The theoretical work by the author and also other researchers for finite-height PCW's shows that leakage-free waveguides with a high refractive index in the waveguiding region have very flat dispersion curves that only cover narrow frequency intervals. Consequently such waveguides are characterized by narrow bandwidth and very low group velocity for guided modes. A general design principle has been presented for the construction of PCW's that support leakage-free guidance of light over very large frequency intervals. The design idea is to introduce a line defect in a photonic crystal, where the material in the line defect has appropriate dispersion properties. A relevant material can be found from effective refractive index considerations. The design idea was illustrated with three-dimensional calculations for a few examples of line defects.

Chapter 12

Resume (danish)

Afhandlingen bidrager til to områder indenfor dielektriske mikrostrukturers optiske egenskaber. Disse områder er emission af elektromagnetisk stråling fra kilder i dielektriske mikrostrukturer og planare bølgeledere baseret på fotoniske krystaller.

Indenfor det første område er der blevet præsenteret tre metoder til at beregne spontan og klassisk emission af stråling fra kilder i dielektriske mikrostrukturer. Metoderne er blevet anvendt på en fotonisk krystal, en fotonisk krystal baseret mikrokavitet, en aktiv step-indeks fiber og en cirkulær symmetrisk dielektrisk skive. I den første metode bliver spontan emission beregnet vha. Fermi's gyldne regel. I denne metode bliver en komplet mængde af ortogonale elektromagnetiske feltløsninger brugt som en basis for kvantisering af stålingsfeltet. I et kvantemekanisk billede er energien i en elektromagnetisk tilstand ikke nul i vakuumtilstanden (ingen fotoner). Den endelige energi i vakuumtilstanden kan fortolkes som værende relateret til vakuumfluktuationer i det elektromagnetiske felt. Raten for spontan emission er proportional med summen af amplituder kvadreret for det elektriske felt hørende til hver elektromagnetisk feltløsning normeret til energien i vakuumtilstanden. Dermed er raten for spontan emission proportional med styrken af det elektriske felts vakuumfluktuationer på det sted kilden befinder sig. De elektromagnetiske feltløsninger blev beregnet vha. planbølgerækkeudviklingsteori og et variations princip. Planbølgerækkeudviklingsteori er velegnet til periodiske strukturer som fotoniske krystaller. Metoden blev anvendt til at undersøge egenskaber vedrørende spontan emission for en to-dimensional fotonisk krystal og en to-dimensional fotonisk krystal baseret mikrokavitet. Raten for spontan emission afhænger kraftigt af kildens position. For mikrokaviteten blev raten for spontan emission

forstærket for kildeemissionsfrekvenser, der stemte overens med frekvenser for kavitetsbølgetyper, hvis kilden var placeret et sted hvor intensiteten af kavtitetsbølgetyperne ikke er lav.

Der er blevet præsenteret en general teori for beregning af spontan emission fra kilder i aktive dielektriske mikrostrukturer. For dielektriske strukturer der forstærker eller absorberer lys (aktive strukturer) findes ikke en komplet mængde af ortogonale feltløsninger. Det er en velegnet procedure for aktive dielektriske strukturer at bruge strømme og elektromagnetiske felter som primære målbare størrelser, der er defineret ved deres kommutationsrelationer. Felt- og strømoperatorer er relateret til hinanden via en klassisk Green's tensor, og spontan emission kan relateres til den transverse komponent af Green's tensoren. Der er blevet præsenteret en metode til at konstruere Green's tensoren for aktive strukturer som en summation af biortogonale elektromagnetiske feltløsninger. Metoden blev illustreret for en aktiv step-indeks fiber, der er en tilstrækkeligt simpel struktur til at der findes analytiske løsninger. For fiberen blev spontan emission studeret mht. emissionsfrekvens, position og vektoriel orientering af en elektrisk dipol. Fjenfelts udstrålingsdiagrammer blev studeret via beregning af Poynting vektoren.

Endeligt blev en integralligningsmetode præsenteret, der kan bruges til at beregne elektromagnetisk stråling genereret af kilder i dielektriske mikrostrukturer med endelig udstrækning. I denne metode blev der brugt et referencesystem, f.eks frit rum, og en feltløsning i referencesystemet. Referencefeltløsningen kan være feltet der udsendes fra en fordeling af kilder i frit rum. Den faktiske mikrostruktur, der har vores interesse, svarer til referencesystemet med ændringer indenfor et område med begrænset udstrækning. Integralligningen giver en feltløsning i mikrostrukturen ud fra feltløsningen i referencesystemet. Med denne metode blev præsenteret beregninger for både nær- og fjernfelter genereret af en dipol strømkilde placeret midt i en dielektrisk skive. Desuden blev sammenhængen mellem den totale udstråling fra kilden og skivens diameter beregnet, og der blev fundet resonancer i udstrålingen for bestemte diametre. Emissionen i resonanstilfældet var 13 gange større end den tilsvarende emission fra den samme dipole placeret i frit rum.

Angående det andet emne, planare bølgeledere baseret på fotoniske krystaller, er der blevet præsenteret en samling af teori resultater. Det præsenterede arbejde giver både en fundamental forståelse for de elektromagnetiske egenskaber af bølgelederne, men giver også retningslinier for hvordan bølgelederne kan designes til at have ønskelige egenskaber som stor båndbredde og lave tab.

Det tidlige teoretiske arbejde for bølgelederne omhandlede det idealis-

erede tilfælde af to-dimensionale eller uendelig-højde bølgeledere, hvor f.eks. dielektriske søjler er uendeligt høje, eller lufthuller i et dielektrisk materiale er uendeligt dybe, således at strukturen kun varierer i to dimensioner. Grundlæggende forskningsresultater blev præsenteret for de elektromagnetiske egenskaber for to-dimensionale bølgeledere hvor designet er baseret på at introducere en liniedefekt i en to-dimensional fotonisk krystal. For bølgeledere baseret på en fotonisk krystal med dielektriske søjler med højt brydningsindeks repeteret periodisk på et triangulært gitter i luft blev givet en analyse af dispersionsegenskaber, energiudbredelse via energiudbredelseshastighed og Poynting-vektor fordeling, og antallet af guidede elektromagnetiske bølgetyper som funktion af frekvens og bølgelederens bredde. Bølgelederens optiske egenskaber er kraftigt afhængige af orienteringen af bølgelederen eller liniedefekten i den fotoniske krystal.

I en virkelig realisering af planare bølgeledere baseret på fotoniske krystaller kan dielektriske søjler ikke være uendeligt høje, og lufthuller i et dielektrisk materiale kan ikke være uendeligt dybe. Den endelige højde af virkelige bølgeledere skal tages i betragtning når bølgelederne ønskes designet til at være fri for udbredelsestab pga. at lys lækker ud af bølgelederen. Der er blevet udviklet og præsenteret en metode der giver retningslinier for design af læktabsfri endelig-højde bølgeledere. I metoden sammenlignes to-dimensionale beregninger for uendelig-højde bølgeledere med dispersionskurver for medier over og under den endeligt høje bølgeleder. Med denne metode blev det klart at bølgeledere med en stor luftfyldt liniedefekt i stor udstrækning har læktab. Det blev også klart at det er fordelagtigt at introducere liniedefekter langs retninger i den fotoniske krystal hvor den rumlige periodicitet er mindst mulig.

For en fotonisk krystal baseret bølgeleder konstrueret af halvledermateriale (silicium) og elektrisk isolerende materiale (glas) blev der foretaget både en to-dimensional og tre-dimensional teoretisk analyse. Den tre-dimensional analyse inkluderer på en nøjagtig måde den endelige højde af den fotoniske krystal. Sammenlignet med den to-dimensionale analyse resulterede den tredimensionale analyse i færre guidede bølgetyper, og de guidede bølgetypers frekvens var forskudt. Feltfordelingen af de guidede bølgetyper i en plan gennem midten af den endeligt høje bølgeleder (3D beregning) var meget lig de tilsvarende feltfordelinger beregnet via en to-dimensional beregning. Tredimensionale beregninger kan være nødvendige for at opnå god overensstemmelse mellem eksperimenter og teoretiske resultater. To ud af tre beregnede frekvensintervaller, hvor lys kan guides uden læktab, stemmer overens med lave målte udbredelsestab [130, 146]. Høje målte udbredelsestab for det tredie frekvensinterval blev forklaret teoretisk ved at undersøge den vertikale

lokalisering af feltet. Dette førte til konklusionen at et glaslag på toppen af den eksperimentelle bølgeleder skal være tykkere for at den understøtter guidede bølgetyper for det tredie frekvensinterval.

Forfatterens og andre forskeres teoretiske arbejde for endelig-højde fotonisk krystal baserede bølgedere viser at bølgeledere uden læktab og med et højt brydningsindeks i bølgelederområdet ofte har flade dispersionskurver, der dækker begrænsede frekvensintervaller. Dermed er bølgelederne karakteriseret ved lille båndbredde og en lille energiudbredelseshastighed for de guidede modes. Der er blevet præsenteret et generelt princip for design af bølgeledere der understøtter læktabsfri bølgeledning for store frekvensintervaller. Designideen går ud på at introducere et materiale i liniedefekten med passende dispersionsegenskaber. Et relevant materiale kan findes vha. overvejelser omkring materialets effektive brydningsindeks. Design ideen blev illustreret med tre-dimensionale beregninger for nogle få udvalgte eksempler på liniedefekter.

Bibliography

[1] G.P. Agrawal, *Fiber-Optic Communication Systems*, Wiley, New York, 1992.

[2] J.D. Joannopoulos, J.N. Winn, and R.D. Meade, *Photonic Crystals: Molding the Flow of Light*, Princeton University Press, Princeton, NJ, 1995.

[3] J.C. Knight, J. Broeng, T.A. Birks, and P.St.J. Russell, "Photonic band gap guidance in optical fibers," *Science - AAAS - Weekly Paper Edition*, vol. 282, no. 5393, pp. 1476, 1998.

[4] J. Broeng, S.E. Barkou, T. Søndergaard, and A. Bjarklev, "Analysis of air-guiding photonic bandgap fibers," *Opt. Lett.*, vol. 25, pp. 96, 2000.

[5] T. Søndergaard, "Photonic crystal distributed feedback fiber lasers with bragg gratings," *IEEE J. Lightwave Technol.*, vol. 18, pp. 589, 2000.

[6] E. Yablonovitch, "Inhibited spontaneous emission in solid-state physics and electronics," *Phys. Rev. Lett.*, vol. 58, no. 20, pp. 2059, 1987.

[7] S. John, "Strong localization of photons in certain disordered dielectric superlattices," *Phys. Rev. Lett.*, vol. 58, pp. 2486, 1987.

[8] E. Yablonovitch, "Photonic bandgap structures," *J. Opt. Soc. Am. B.*, vol. 10, pp. 283, 1993.

[9] M. Bayindir, B. Temelkuran, and E. Ozbay, "Propagation of photons by hopping: A waveguiding mechanism through localized coupled cavities in three-dimensional photonic crystals," *Phys. Rev. B*, vol. 61, no. 18, pp. R11855, 2000.

[10] J.G. Fleming and Shawn-Yu Lin, "Three-dimensional photonic crystal with a stop band from 1.35 to 1.95 μm," *Opt. Lett.*, vol. 24, no. 1, pp. 49, 1999.

[11] S. Noda, N. Yamamoto, H. Kobayashi, M. Okano, and K. Tomoda, "Optical properties of three-dimensional photonic crystals based on iii-v semiconductors at infrared to near-infrared wavelengths," *Appl. Phys. Lett.*, vol. 75, no. 7, pp. 905, 1999.

[12] E. Yablonovitch, "Photonic crystals: semiconductors of light," *Sci. Am.*, pp. 36–41, Dec. 2001.

[13] T.F. Krauss and R.M. De La Rue, "Photonic crystals in the optical regime - past, present and future," *Prog. Quantum Electron.*, vol. 23, pp. 51, 1999.

[14] O. Painter, R.K. Lee, A. Scherer, A. Yariv, J.D. O'Brien, P.D. Dapkus, and I. Kim, "Two-dimensional photonic band-gap defect mode laser," *Science - AAAS - Weekly Paper Edition*, vol. 284, no. 5421, pp. 1819, 1999.

[15] M. Meier, A. Dodabalapur, J.A. Rogers, R.E. Slusher, A. Mekis, and A. Timko, "Emission characteristics of two-dimensional organic photonic crystal lasers fabricated by replica modeling," *J. Appl. Phys.*, vol. 86, pp. 3502, 1999.

[16] J. Moosburger, M. Kamp, F. Klopf, J.P. Reithmaier, and A. Forchel, "Semiconductor lasers with 2-D-photonic crystal mirrors based on a wet-oxidized Al_2O_3-mask," *IEEE Photon. Technol. Lett.*, vol. 13, pp. 406, 2001.

[17] J.K. Hwang, H.Y. Ryu, D.S. Song, I.Y. Han, H.K. Park, D.H. Jang, and Y.H. Lee, "Continuous room-temperature operation of optically pumped two-dimensional photonic crystal lasers at 1.6 μm," *IEEE Photon. Technol. Lett.*, vol. 12, pp. 1295, 2000.

[18] A. Mekis, J.C. Chen, I. Kurland, S. Fan, P.R. Villeneuve, and J.D. Joannopoulos, "High transmission through sharp bends in photonic crystal waveguides," *Phys. Rev. Lett.*, vol. 77, pp. 3787, 1996.

[19] T. Søndergaard and K.H. Dridi, "Energy flow in photonic crystal waveguides," *Phys. Rev. B*, vol. 61, pp. 15688, 2000.

[20] E.M. Purcell, "Spontaneous emission probabilities at radio frequencies," *Phys. Rev.*, vol. 69, pp. 681, 1946.

[21] P.W. Milonni and P.L. Knight, "Spontaneous emission between mirrors," *Opt. Comm.*, vol. 9, no. 2, pp. 119, 1973.

[22] M.R. Philpott, "Fluorescence from molecules between mirrors," *Chem. Phys. Lett.*, vol. 19, no. 3, pp. 435, 1973.

[23] W. Lukosz, "Theory of optical-environment-dependent spontaneous-emission rates for emitters in thin layers," *Phys. Rev. B*, vol. 22, no. 6, pp. 3030, 1980.

[24] H. Yokoyama and K. Ujihara, *Spontaneous emission and laser oscillations in microcavities*, CRC Press, New York, 1995.

[25] P. Milonni, *The quantum vacuum. An introduction to quantum electrodynamics*, Academic Press, San Diego, 1994.

[26] J. Rarity and C. Weisbuch, *Microcavities and Photonic Bandgaps*, Kluwer, Dordrecht, 1996.

[27] R.K. Chang and A.J. Campillo, *Optical Processes in Microcavities*, World Scientific, Singapore, 1996.

[28] P. Goy, J.M. Raimond, M. Gross, and S. Haroche, "Observation of cavity-enhanced single-atom spontaneous emission," *Phys. Rev. Lett.*, vol. 50, no. 24, pp. 1903, 1983.

[29] G. Gabrielse and H. Dehmelt, "Observation of inhibited spontaneous emission," *Phys. Rev. Lett.*, vol. 55, no. 1, pp. 67, 1985.

[30] R.G. Hulet, E.S. Hilfer, and D. Kleppner, "Inhibited spontaneous emission by a Rydberg atom," *Phys. Rev. Lett.*, vol. 55, no. 20, pp. 2137, 1985.

[31] G. Björk, S. Machida, Y. Yamamoto, and K. Igeta, "Modification of spontaneous emission rate in planar dielectric microcavity structures," *Phys. Rev. A*, vol. 44, no. 1, pp. 669, 1991.

[32] J.-M. Gérard, B. Sermage, B. Gayral, B. Legrand, E. Costard, and V. Thierry-Mieg, "Enhanced spontaneous emission by quantum boxes in a monolithic optical microcavity," *Phys. Rev. Lett.*, vol. 81, no. 5, pp. 1110, 1998.

[33] D.G. Deppe, L.A. Graham, and D.L. Huffaker, "Enhanced spontaneous emission using quantum dots and an apertured microcavity," *IEEE J. Quantum Electron.*, vol. 35, no. 10, pp. 1502, 1999.

[34] P.M.W. Skovgaard, S.D. Brorson, I. Balslev, and C.C. Larsen, "Microcavity effects in Er3+-doped optical fibres," in *Microcavities and photonic bandgaps: physics and applications*, J. Rarity and C. Weisbuch, Eds. Kluwer, Dordrecht, 1996.

[35] H. Zbinden, A. Müller, and N. Gisin, "Decay time and spectrum of rare earth fluorescence in silvered microfibers," in *Microcavities and photonic bandgaps: physics and applications*, J. Rarity and C. Weisbuch, Eds. Kluwer, Dordrecht, 1996.

[36] A.M. Vredenberg, N.E.J. Hunt, E.F. Schubert, D.C. Jacobsen, J.M. Poate, and G.J. Zydzik, "Controlled atomic spontaneous emission from Er3+ in a transparent Si/SiO2 microcavity," *Phys. Rev. Lett.*, vol. 71, no. 4, pp. 517, 1993.

[37] I. Abram, I. Robert, and R. Kuszelewicz, "Spontaneous emission control in semiconductor microcavities with metallic or Bragg mirrors," *IEEE J. Quantum Electron.*, vol. 34, no. 1, pp. 71, 1998.

[38] T. Søndergaard, "Spontaneous emission in two-dimensional photonic crystal microcavities," *IEEE J. Quantum Electron.*, vol. 36, no. 4, pp. 450, 2000.

[39] T. Søndergaard and B. Tromborg, "General theory for spontaneous emission in active dielectric microstructures: example of a fiber amplifier," *Phys. Rev. A*, vol. 64, pp. 033812, 2001.

[40] T. Søndergaard, D. Lenstra, and B. Tromborg, "Near fields and far fields generated by sources in the presence of dielectric structures with cylindrical symmetry," *Opt. Lett.*, vol. 26, pp. 1705, 2001.

[41] O. Painter, J. Vuckovic, and A. Scherer, "Defect modes of a two-dimensional photonic crystal in an optically thin dielectric slab," *J. Opt. Soc. Am. B*, vol. 16, no. 2, pp. 275, 1999.

[42] X.P. Feng and Y. Arakawa, "Off-plane angle dependence of photonic band gap in a two-dimensional photonic crystal," *IEEE J. Quantum Electron.*, vol. 32, no. 3, pp. 535, 1996.

[43] T. Søndergaard, J. Broeng, A. Bjarklev, K. Dridi, and S.E. Barkou, "Suppression of spontaneous emission for a two-dimensional honeycomb photonic bandgap structure estimated using a new effective-index model," *IEEE, J. Quantum Electron.*, vol. 34, no. 12, pp. 2308, 1998.

[44] R Louden, *The Quantum Theory of Light, second edition*, Clarendon Press, Oxford, 1983.

[45] T. Søndergaard, J. Broeng, and A. Bjarklev, "Suppression of spontaneous emission for two-dimensional GaAs photonic crystal microcavities," in *CLEO'99*, 23-28 May 1999, p. JFA2.

[46] K. Busch and S. John, "Photonic band gap formation in certain self-organizing systems," *Phys. Rev. E*, vol. 58, no. 3, pp. 3896, 1998.

[47] R.D. Meade, A.M. Rappe, K.D. Brommer, J.D. Joannopoulos, and O.L. Alerhand, "Accurate theoretical analysis of photonic band-gap materials," *Phys. Rev. B*, vol. 48, no. 11, pp. 8434, 1993.

[48] R.D. Meade, A.M. Rappe, K.D. Brommer, J.D. Joannopoulos, and O.L. Alerhand, "Erratum:accurate theoretical analysis of photonic band-gap materials," *Phys. Rev. B*, vol. 55, no. 23, pp. 15942, 1997.

[49] K.M. Ho, C.T. Chan, and C.M. Soukoulis, "Existence of a photonic gap in periodic dielectric structures," *Phys. Rev. Lett.*, vol. 65, no. 25, pp. 3152, 1990.

[50] S.C. Ching, H.M. Lai, and K. Young, "Dielectric microspheres as optical cavities: Einstein A and B coefficients and level shift," *J. Opt. Soc. Am. B*, vol. 4, no. 12, pp. 2004, 1987.

[51] S. Ramo, J.R. Whinnery, and T.Van Ducer, *Fields and Waves in Communication Electronics (Third Edition)*, John Wiley and sons, New York, 1994.

[52] S.M. Barnett, B. Huttner, and R. Louden, "Spontaneous emission in absorbing dielectric media," *Phys. Rev. Lett.*, vol. 68, no. 25, pp. 3698, 1992.

[53] S.C. Ching, H.M. Lai, and K. Young, "Dielectric microspheres as optical cavities: thermal spectrum and density of states," *J. Opt. Soc. Am. B*, vol. 4, no. 12, pp. 1995, 1987.

[54] M.P. Teter, M.C. Payne, and D.C. Allan, "Solution of schrödinger's equation for large systems," *Phys. Rev. B*, vol. 40, no. 18, pp. 12255, 1989.

[55] D.E. Aspnes, "Local-field effects and effective-medium theory: A microscopic perspective," *Am. J. Phys.*, vol. 50, no. 8, pp. 704, 1981.

[56] M. Plihal and A.A. Maradudin, "Photonic band structure of two-dimensional systems," *Phys. Rev. B*, vol. 44, no. 16, pp. 8565, 1991.

[57] A.A. Maradudin and A.R. McGurn, "Out of plane propagation of electromagnetic waves in a two-dimensional periodic dielectric medium," *J. Mod. Opt.*, vol. 41, no. 2, pp. 275, 1994.

[58] S.D. Brorson, H. Yokoyama, and E.P. Ippen, "Spontaneous emission rate alteration in optical waveguide structures," *IEEE J. Quantum Electron.*, vol. 26, no. 9, pp. 1492, 1990.

[59] M.P. van Exter, G. Nienhuis, and J.P. Woerdman, "Two simple expressions for the spontaneous emission factor β," *Phys. Rev. A*, vol. 54, no. 4, pp. 3553, 1996.

[60] G.S. Agarwal, "Quantum electrodynamics in the presence of dielectrics and conductors. iv. general theory for spontaneous emission in finite geometries," *Phys. Rev. A*, vol. 12, pp. 1475, 1975.

[61] J.M. Wylie and J.E. Sipe, "Quantum electrodynamics near an interface," *Phys. Rev. A*, vol. 30, pp. 1185, 1984.

[62] R.J. Glauber and M. Lewenstein, "Quantum optics of dielectric media," *Phys. Rev. A*, vol. 43, no. 1, pp. 467, 1991.

[63] T. Gruner and D.-G. Welsch, "Green-function approach to the radiation-field quantization for homogeneous and inhomogeneous Kramers-Kronig dielectrics," *Phys. Rev. A*, vol. 53, no. 3, pp. 1818, 1996.

[64] S. Scheel, L. Knöll, and D.-G. Welsch, "Quantum local-field corrections and spontaneous decay," *Phys. Rev. A*, vol. 60, no. 2, pp. 1590, 1999.

[65] R. Sprik, B.A. Van Tiggelen, and A. Lagendijk, "Optical emission in periodic dielectrics," *Europhys. lett.*, vol. 35, no. 4, pp. 265, 1996.

[66] H.T. Dung, L. Knöll, and D.-G. Welsch, "Three-dimensional quantization of the electromagnetic field in dispersive and absorbing inhomogeneous dielectrics," *Phys. Rev. A*, vol. 57, no. 5, pp. 3931, 1998.

[67] B. Huttner and S.M. Barnett, "Quantization of the electromagnetic field in dielectrics," *Phys. Rev. A*, vol. 46, no. 7, pp. 4306, 1992.

[68] M.S. Barnett, B. Huttner, R. Loudon, and R. Matloob, "Decay of excited atoms in absorbing dielectrics," *J. Phys. B: At. Mol. Opt. Phys.*, vol. 29, pp. 3763, 1996.

[69] A. Tip, "Canonical formalism and quantization for a class of classical fields with application to radiative atomic decay in dielectrics," *Phys. Rev. A*, vol. 56, no. 6, pp. 5022, 1997.

[70] S. Scheel, L. Knöll, and D.-G. Welsch, "QED commutation relations for inhomogeneous kramers-kronig dielectrics," *Phys. Rev. A*, vol. 58, no. 1, pp. 700, 1998.

[71] M.S. Yeung and T.K. Gustafson, "Spontaneous emission near an absorbing dielectric surface," *Phys. Rev. A*, vol. 54, no. 6, pp. 5227, 1996.

[72] W. Vogel and D.-G. Welsch, *Lectures on quantum optics*, Akademie Verlag, Berlin, 1994.

[73] H.T. Dung, L. Knöll, and D.-G. Welsch, "Spontaneous decay in the presence of dispersing and absorbing bodies: General theory and application to a spherical cavity," *Phys. Rev. A*, vol. 62, pp. 053804, 2000.

[74] K. Petermann, "Calculated spontaneous emission factor for double-heterostructure injection lasers with gain-induced waveguiding," *IEEE J. Quantum Electron.*, vol. QE-15, no. 7, pp. 566, 1979.

[75] H.A. Haus and S. Kawakami, "On the "excess spontaneous emission factor" in gain-guided laser amplifiers," *IEEE J. Quantum Electron.*, vol. QE-21, no. 1, pp. 63, 1985.

[76] C.H. Henry, "Theory of spontaneous emission noise in open resonators and its application to lasers and optical amplifiers," *J. Lightwave Technol.*, vol. LT-4, no. 3, pp. 288, 1986.

[77] I.H. Deutsch, J.C. Garrison, and E.M. Wright, "Excess noise in gain-guided amplifiers," *J. Opt. Soc. Am. B*, vol. 8, no. 6, pp. 1244, 1991.

[78] B. Tromborg, H.E. Lassen, and H. Olesen, "Traveling wave analysis of semiconductor lasers: modulation responses, mode stability and quantum mechanical treatment of noise spectra," *IEEE J. Quantum Electron.*, vol. 30, no. 4, pp. 939, 1994.

[79] R. Marani and M. Lax, "Spontaneous emission in non-Hermitian optical systems: Distributed-feedback semiconductor lasers," *Phys. Rev. A*, vol. 52, no. 3, pp. 2376, 1995.

[80] C.H. Henry and R.F. Kazarinov, "Quantum noise in photonics," *Rev. Mod. Phys.*, vol. 68, pp. 801, 1996.

[81] A.E. Siegman, "Excess spontaneous emission in non-Hermitian optical systems. I. laser amplifiers," *Phys. Rev. A*, vol. 39, no. 3, pp. 1253, 1989.

[82] A.E. Siegman, "Excess spontaneous emission in non-Hermitian optical systems. II. laser oscillators," *Phys. Rev. A*, vol. 39, no. 3, pp. 1264, 1989.

[83] W.A. Hamel and J.P. Woerdman, "Nonorthogonality of the longitudinal eigenmodes of a laser," *Phys. Rev. A*, vol. 40, no. 5, pp. 2785, 1989.

[84] A.E. Siegman, "Lasers without photons - or should it be lasers with too many photons?," *Appl. Phys. B*, vol. 60, pp. 247, 1995.

[85] Ph. Grangier and J.-Ph. Poizat, "A simple quantum picture for the Petermann excess noise factor," *Eur. Phys. J. D*, vol. 1, pp. 97, 1998.

[86] M.S. Tomaŝ, "Green function for multilayers: Light scattering in planar cavities," *Phys. Rev. A*, vol. 51, no. 3, pp. 2545, 1995.

[87] M.S. Tomaŝ and Z. Lenac, "Decay of excited molecules in absorbing planar cavities," *Phys. Rev. A*, vol. 56, pp. 4197, 1997.

[88] M.S. Tomaŝ and Z. Lenac, "Spontaneous emission spectrum in an absorbing Fabry-Perot cavity," *Phys. Rev. A*, vol. 60, pp. 2431, 1999.

[89] H. Rigneault, S. Robert, C. Begon, B. Jacquier, and P. Moretti, "Radiative and guided wave emission of Er3+ atoms located in planar

multidielectric structures," *Phys. Rev. A*, vol. 55, no. 2, pp. 1497, 1997.

[90] H.P. Urbach and G.L.J.A. Rikken, "Spontaneous emission from a dielectric slab," *Phys. Rev. A*, vol. 57, no. 5, pp. 3913, 1998.

[91] B. Demeulenaere, R. Baets, and D. Lenstra, "Quantum electrodynamical theory and modeling of light emission in vertical cavity devices," *Proceedings of the SPIE*, vol. 2693, pp. 188, 1996.

[92] C. Hooijer, D. Lenstra, and A. Lagendijk, "Mode density inside an omnidirectional mirror is heavily directional but not small," *Opt. Lett.*, vol. 25, pp. 1666, 2000.

[93] D.Y. Chu and S.-T. Ho, "Spontaneous emission from excitons in cylindrical dielectric waveguides and the spontaneous-emission factor of microcavity ring lasers," *J. Opt. Soc. Am. B*, vol. 10, no. 2, pp. 381, 1993.

[94] H. Nha and W. Jhe, "Cavity quantum electrodynamics for a cylinder: Inside a hollow dielectric and near a solid dielectric cylinder," *Phys. Rev. A*, vol. 56, pp. 2213, 1997.

[95] W. Zakowicz and M. Janowicz, "Spontaneous emission in the presence of a dielectric cylinder," *Phys. Rev. A*, vol. 62, pp. 013820, 2000.

[96] C.L.A. Hooijer, *Spontaneous emission in a dielectric environment*, Vrije Universiteit, Amsterdam, Holland, Ph.D-thesis, 2001.

[97] C. Cohen-Tannoudji, J. Dupont-Roc, and G. Grynberg, *Photons and Atoms - Introduction to Quantum Electrodynamics*, John Wiley Sons, N.Y., 1989.

[98] H.-G. Unger, *Planar optical waveguides and fibres*, Clarendon Press, Oxford, 1977.

[99] W.A. Snyder and J.D. Love, *Optical Waveguide Theory*, Chapman and Hall, New York, 1983.

[100] A. Dodabalapur, M. Berggren, R.E. Slusher, Z. Bao, A. Timko, P. Schiortino, E. Laskowski, H.E. Katz, and O. Nalamasu, "Resonators and materials for organic lasers based on energy transfer," *IEEE J. Select. Top. Quantum Electron.*, vol. 4, pp. 67, 1998.

[101] E.M. Purcell and C.R. Pennypacker, "Scattering and absorption of light by nonspherical dielectric grains," *The Astrophysical Journal*, vol. 186, pp. 706, 1973.

[102] B.T. Draine, "The discrete-dipole approximation and its application to interstellar graphite grains," *The astrophysical journal*, vol. 848, pp. 1988, 1988.

[103] A. Hoekstra, J. Rahola, and P. Sloot, "Accuracy of internal fields in volume integral equation simulations of light scattering," *Appl. Opt.*, vol. 37, pp. 8482, 1998.

[104] G.H. Goedecke and S.G. O'Brien, "Scattering by irregular inhomogeneous particles via the digitized green's function algorithm," *Appl. Opt.*, vol. 27, pp. 2431, 1988.

[105] M.F. Iskander, H.Y. Chen, and J.E. Penner, "Optical scattering and absorption by branched chains of aerosols," *Appl. Opt.*, vol. 28, pp. 3083, 1989.

[106] C. Girard and A. Dereux, "Near-field optics theories," *Rep. Prog. Phys.*, vol. 59, pp. 657, 1996.

[107] O.J.F. Martin, C. Girard, D.R. Smith, and S. Schultz, "Generalized field propagator for arbitrary finite-size photonic band gap structures," *Phys. Rev. Lett.*, vol. 82, pp. 315, 1999.

[108] M.L.M. Balistreri, J.P. Korterik, L. Kuipers, and N.F. van Hulst, "Local observations of phase singularities in optical fields in waveguide structures," *Phys. Rev. Lett.*, vol. 85, pp. 294, 2000.

[109] P.L. Phillips, J.C. Knight, B.J. Mangan, P.St.J. Russell, M.D.B. Charlton, and G.J. Parker, "Near-field optical microscopy of thin photonic crystal films," *J. Appl. Phys.*, vol. 85, pp. 6337, 1999.

[110] S.I. Bozhevolnyi, J. Erland, K. Leosson, P.M.W. Skovgaard, and J.M. Hvam, "Waveguiding in surface plasmon polariton band gap structures," *Phys. Rev. Lett.*, vol. 86, pp. 3008, 2001.

[111] S.T. Ho, S.L. McCall, and R.E. Slusher, "Spontaneous emission from excitons in thin dielectric layers," *Opt. Lett.*, vol. 18, no. 11, pp. 909, 1993.

[112] J. van Bladel, *Singular electromagnetic fields and sources*, IEEE press, NJ, 1991.

[113] O.J.F. Martin, C. Girard, and A. Dereux, "Generalized field propagator for electromagnetic scattering and light confinement," *Phys. Rev. Lett.*, vol. 74, pp. 526, 1995.

[114] J. Nachamkin, "Integrating the dyadic green's function near sources," *IEEE Trans. Ant. Prop.*, vol. 38, pp. 919, 1990.

[115] A.D. Yaghjian, "Electric dyadic green's functions in the source region," *Proc. IEEE*, vol. 68, pp. 243, 1980.

[116] J.-M. Gérard and B. Gayral, "Strong purcell effect for InAs quantum boxes in three-dimensional solid-state microcavities," *J. Lightwave Technol.*, vol. 17, no. 11, pp. 2089, 1999.

[117] L.A. Graham, D.L. Huffaker, and D.G. Deppe, "Spontaneous lifetime control in a native-oxide-apertured microcavity," *Appl. Phys. Lett.*, vol. 74, no. 17, pp. 2408, 1999.

[118] H. Nha and W. Jhe, "Cavity quantum electrodynamics between parallel dielectric surfaces," *Phys. Rev. A*, vol. 54, pp. 3505, 1996.

[119] J. Arentoft, M. Kristensen, T. Søndergaard, and A. Boltasseva, "Realization of robust photonic crystal waveguides designed to reduce out-of-plane scattering," *27th European Conference on Optical Communication (ECOC'01), Amsterdam, Proceedings-volume 4*, p. paper th.a.2.6, 2001.

[120] M.D.B. Charlton, G.J. Parker, and M.E. Zoorob, "Recent developments in the design and fabrication of visible photonic band gap waveguide devices," *J. Mater. Sci. - Mat. Electron.*, vol. 10, pp. 429, 1999.

[121] M. Tokushima, H. Kosaka, A. Tomita, and H. Yamada, "Lightwave propagation through a 120 degrees sharply bent single-line-defect photonic crystal waveguide," *Appl. Phys. Lett.*, vol. 76, pp. 952, 2000.

[122] C.J.M. Smith, H. Benisty, S. Olivier, M. Rattier, C. Weisbuch, T.F. Krauss, R.M. De La Rue, R. Houdre, and U. Oesterle, "Low-loss channel waveguides with two-dimensional photonic crystal boundaries," *Appl. Phys. Lett.*, vol. 77, pp. 2813, 2000.

[123] M. Loncar, D. Nedeljkovich, T. Doll, A. Vuckovic, A. Scherer, and T.P. Pearsall, "Waveguiding in planar photonic crystals," *Appl. Phys. Lett.*, vol. 77, pp. 1937, 2000.

[124] S.Y. Lin, E. Chow, S.G. Johnson, and J.D. Joannopoulos, "Demonstration of highly efficient waveguiding in a photonic crystal slab at the 1.5μm wavelength," *Opt. Lett.*, vol. 25, pp. 1297, 2000.

[125] S. Olivier, M. Rattier, H. Benisty, C. Weisbuch, C.J.M. Smith, R.M. De La Rue, T.F. Krauss, U. Oesterle, and R. Houdre, "Ministopbands of a one-dimensional system: The channel waveguide in a two-dimensional photonic crystal," *Phys. Rev. B*, vol. 63, pp. 113311, 2001.

[126] A. Talneau, L. Le Gouezigou, and N. Bouadma, "Quantitative measurement of low propagation losses at 1.55μm on planar photonic crystal waveguides," *Opt. Lett.*, vol. 26, no. 16, pp. 1259, 2001.

[127] T. Baba, N. Fukaya, and A. Motegi, "Clear correspondence between theoretical and experimental light propagation characteristics in photonic crystal waveguides," *Electron. Lett.*, vol. 37, pp. 761, 2001.

[128] E. Chow, S.Y. Lin, J.R. Wendt, S.G. Johnson, and J.D. Joannopoulos, "Quantitative analysis of bending efficiency in photonic-crystal waveguide bends at $\lambda = 1.55$ mm wavelengths," *Opt. Lett.*, vol. 26, pp. 286, 2001.

[129] M. Notomi, A. Shinya, K. Yamada, J. Takahashi, C. Takahashi, and I. Yokohama, "Single-mode transmission within photonic bandgap of width-varied single-line-defect photonic crystal waveguides on SOI substrates," *Electron. Lett.*, vol. 37, pp. 292, 2001.

[130] J. Arentoft, T. Søndergaard, M. Kristensen, A. Boltasseva, M. Thorhauge, and L. Frandsen, "Low-loss silicon-on-insulator photonic crystal waveguides," *submitted for Electronics letters*, 2001.

[131] S. Olivier, C. Smith, M. Rattier, H. Benisty, C. Weisbuch, T. Krauss, R. Houdre, and U. Oesterle, "Miniband transmission in a photonic crystal coupled-resonator optical waveguide," *Opt. Lett.*, vol. 26, no. 13, pp. 1019, 2001.

[132] H. Benisty, "Modal analysis of optical guides with two-dimensional photonic band-gap boundaries," *J. Appl. Phys.*, vol. 79, pp. 7483, 1996.

[133] A. Mekis, S. Fan, and J.D. Joannopoulos, "Bound states in photonic crystal waveguides and waveguide bends," *Phys. Rev. B*, vol. 58, pp. 4809, 1998.

[134] E. Centeno and D. Felbacq, "Guiding waves with photonic crystals," *Opt. Comm.*, vol. 160, pp. 57, 1999.

[135] E. Centeno, B. Guizal, and D. Felbacq, ," *J. Opt. A: Pure Appl. Opt.*, vol. 1, pp. L10, 1999.

[136] R.W. Ziolkowski and M. Tanaka, "FDTD analysis of PBG waveguides, power splitters and switches," *Opt. Quant. Electron.*, vol. 31, pp. 843, 1999.

[137] J.B. Nielsen, T. Søndergaard, S.E. Barkou, A. Bjarklev, and J. Broeng, "Two-dimensional kagomé photonic bandgap waveguide," *IEEE Photon. Technol. Lett.*, vol. 12, pp. 60, 2000.

[138] T. Søndergaard, A. Bjarklev, M. Kristensen, J. Erland, and J. Broeng, "Designing finite height photonic crystal waveguides," *Appl. Phys. Lett.*, vol. 77, pp. 785, 2000.

[139] T. Søndergaard, A. Bjarklev, J. Arentoft, M. Kristensen, J. Erland, J. Broeng, and S.E. Barkou Libori, "Designing finite-height photonic crystal waveguides: confinement of light and dispersion relations," *Opt. Comm.*, vol. 194, pp. 341, 2001.

[140] Ph. Lalanne and H. Benisty, "Out-of-plane losses of two-dimensional photonic crystals waveguides: Electromagnetic analysis," *J. Appl. Phys.*, vol. 89, pp. 1512, 2001.

[141] M. Palamaru and Ph. Lalanne, "Photonic crystal waveguides: Out-of-plane losses and adiabatic modal conversion," *Appl. Phys. Lett.*, vol. 78, pp. 1466, 2001.

[142] O. Painter, R.K. Lee, A. Scherer, A. Yariv, J.D. O'Brien, P.D. Dapkus, and I. Kim, "Two-dimensional photonic band-gap defect mode laser," *Science - AAAS - Weekly Paper Edition*, vol. 284, no. 5421, pp. 1819, 1999.

[143] M. Loncar, T. Doll, J. Vuckovic, and A. Scherer, "Design and fabrication of silicon photonic crystal optical waveguides," *J. Lightwave Technol.*, vol. 18, pp. 1402, 2000.

[144] X. Letartre, C. Seassal, C. Grillet, P. Rojo-Romeo, P. Viktorovitch, M. Le Vassor d'Yerville, D. Cassagne, and C. Jouanin, "Group velocity and propagation losses measurement in a single-line photonic-crystal waveguide on inp membranes," *Appl. Phys. Lett.*, vol. 79, no. 15, pp. 2312, 2001.

[145] S.G. Johnson, P.R. Villeneuve, S. Fan, and J.D. Joannopoulos, "Linear waveguides in photonic crystal slabs," *Phys. Rev. B*, vol. 62, pp. 8212, 2000.

[146] T. Søndergaard, J. Arentoft, and M. Kristensen, "Theoretical analysis of finite-height semiconductor-on-insulator based planar photonic crystal waveguides," *Submitted to J. Lightwave Technol. in sept. 2001, Accepted subject to revisions in jan. 2002.*

[147] M. Loncar, J. Vuckovic, and A. Scherer, "Methods for controlling positions of guided modes of photonic-crystal waveguides," *J. Opt. Soc. Am. B*, vol. 18, no. 9, pp. 1362, 2001.

[148] T. Søndergaard and A. Lavrinenko, "Large-bandwidth planar photonic crystal waveguides," *Submitted to Opt. Comm. in oct. 2001, Accepted subject to revisions in jan. 2002.*

[149] S. Fan, P.R. Villeneuve, J.D. Joannopoulos, and E.F. Schubert, "High extraction efficiency of spontaneous emission from slabs of photonic crystals," *Phys. Rev. Lett.*, vol. 78, no. 17, pp. 3294, 1997.

[150] M. Boroditsky, R. Vrijen, T.F. Krauss, R. Coccioli, R. Bhat, and E. Yablonovitch, "Spontaneous emission extraction and Purcell enhancement from thin-film 2-d photonic crystals," *J. Lightwave Technol.*, vol. 17, pp. 2096, 1999.

[151] S.G. Johnson, S. Fan, and J.D. Joannopoulos, "Guided modes in photonic crystal slabs," *Phys. Rev. B*, vol. 60, pp. 5751, 1999.

[152] H.-Y. Ryu, J.-K. Hwang, and Y.-H. Lee, "Conditions of single guided mode in two-dimensional triangular photonic crystal slab waveguides," *J. Appl. Phys.*, vol. 88, pp. 4941, 2000.

[153] A. Chutinan and S. Noda, "Waveguides and waveguide bends in two-dimensional photonic crystal slabs," *Phys. Rev. B*, vol. 62, pp. 4488, 2000.

[154] S. Kuchinsky, D.C. Allan, N.F. Borelli, and J.-C. Cotteverte, "3D localization in a channel waveguide in a photonic crystal with 2D periodicity," *Opt. Comm.*, vol. 175, pp. 147, 2000.

[155] T. Baba and T. Matsuzaki, "Theoretical calculation of photonic gap in semiconductor 2-dimensional photonic crystals with various shapes of optical atoms," *Japanese Journal of Applied Physics, Part 1*, vol. 34, no. no.8B, pp. 4496, 1995.

[156] C.M. Anderson and K.P. Giapis, "Larger two-dimensional photonic band gaps," *Phys. Rev. Lett.*, vol. 77, pp. 2949, 1996.

[157] D. Cassagne, C. Jouanin, and D. Bertho, "Photonic band gaps in two-dimensional graphite structure," *Phys. Rev. B*, vol. 52, pp. R2217, 1995.

[158] T.F. Krauss, "Photonic crystals for integrated optics," *AIP Conf. Proc.*, vol. 560, pp. 89, 2001.

[159] A. Yariv, Y. Xu, R.K. Lee, and A. Scherer, "Coupled-resonator optical waveguide: a proposal and analysis," *Opt. Lett.*, vol. 24, pp. 711, 2000.

[160] R.A. Sammut, "Orthogonality and normalization of radiation modes in dielectric waveguides," *J. Opt. Soc. Am.*, vol. 72, no. 10, pp. 1335, 1982.

Appendix A

Biorthogonality and normalization of radiation modes

This appendix concerns the relations between the coefficients A_α, B_α, C_α^+, C_α^-, D_α^+, D_α^- in Eqs. (4.38) and (4.39) for a given set of quantization parameters m, β, q, and we will use the notation introduced in Sec. 4.4. Due to the boundary conditions at the core-cladding interface of the step-index optical fiber these coefficients are not independent. Furthermore, in this appendix a biorthogonal set of radiation modes is constructed, and a normalization integral for the modes is calculated.

The relations between C_α^+, C_α^-, D_α^+, D_α^- and A_α and B_α may be expressed by first introducing a number of constants

$$T = {H_m^{(1)}}'(qa)H_m^{(2)}(qa) - {H_m^{(2)}}'(qa)H_m^{(1)}(qa) = \frac{4i}{\pi qa}, \tag{A.1}$$

$$K_1 = i\frac{\beta}{a}mJ_m(\kappa a)H_m^{(2)}(qa)\sqrt{\frac{\beta^2+q^2}{\varepsilon_2}}\frac{\varepsilon_2-\varepsilon_1}{\kappa^2 q^2}, \tag{A.2}$$

$$K_2 = i\frac{\beta}{a}mJ_m(\kappa a)H_m^{(1)}(qa)\sqrt{\frac{\beta^2+q^2}{\varepsilon_2}}\frac{\varepsilon_2-\varepsilon_1}{\kappa^2 q^2}, \tag{A.3}$$

$$M_1 = \frac{1}{\kappa}{J_m}'(\kappa a)H_m^{(2)}(qa) - \frac{1}{q}J_m(\kappa a){H_m^{(2)}}'(qa), \tag{A.4}$$

$$M_2 = \frac{1}{\kappa}{J_m}'(\kappa a)H_m^{(1)}(qa) - \frac{1}{q}J_m(\kappa a){H_m^{(1)}}'(qa), \tag{A.5}$$

$$L_1 = \frac{\varepsilon_1}{\kappa} {J_m}'(\kappa a) {H_m}^{(2)}(qa) - \frac{\varepsilon_2}{q} J_m(\kappa a) {H_m}^{(2)'}(qa), \tag{A.6}$$

$$L_2 = \frac{\varepsilon_1}{\kappa} {J_m}'(\kappa a) {H_m}^{(1)}(qa) - \frac{\varepsilon_2}{q} J_m(\kappa a) {H_m}^{(1)'}(qa), \tag{A.7}$$

where here ($'$) denotes the derivative with respect to the argument.

In terms of these constants the relations between A_α, B_α, C_α^+, C_α^-, D_α^+, D_α^- obtained from the boundary conditions may be written

$$C_\alpha^+ = \frac{q}{T\varepsilon_2}\Big(A_\alpha L_1 + \mu_0 c B_\alpha K_1\Big), \tag{A.8}$$

$$C_\alpha^- = \frac{q}{T^*\varepsilon_2}\Big(A_\alpha L_2 + \mu_0 c B_\alpha K_2\Big), \tag{A.9}$$

$$\mu_0 c D_\alpha^+ = -\frac{q}{T}\Big(A_\alpha K_1 - \mu_0 c B_\alpha M_1\Big), \tag{A.10}$$

$$\mu_0 c D_\alpha^- = -\frac{q}{T^*}\Big(A_\alpha K_2 - \mu_0 c B_\alpha M_2\Big). \tag{A.11}$$

Clearly, only two coefficients are linearly independent, and the index p will be used to label two such linearly independent solutions. These two solutions must be chosen so that the biorthogonality requirement

$$\int \varepsilon(\mathbf{r}) \mathbf{E}_\alpha(\mathbf{r}) \cdot \mathbf{E}_{\widetilde{\alpha'}}(\mathbf{r}) d^3r = N_\alpha \delta_{mm'} \delta_{pp'} \delta(\beta - \beta') \delta(q - q') \tag{A.12}$$

is satisfied. Similar to what was reported in [160] for dielectric waveguides, all finite terms resulting from the integration in the fiber core will cancel with each other. The singular terms giving rise to the Dirac delta functions result only as the integration limits tend to infinity. Taking advantage of the cancellation of finite terms we need only identify the factor N_α in front of the δ-functions. Thereby, the evaluation of the integral in Eq. (A.12) is aided significantly by taking advantage of the following limiting forms of the Hankel functions:

$$ {H^{(1)}}_m(q\rho) \approx \sqrt{\frac{2}{\pi q\rho}} e^{i(q\rho - m\pi/2 - \pi/4)} \quad , \quad \rho >> 1/q \tag{A.13}$$

$$ {H^{(2)}}_m(q\rho) \approx \sqrt{\frac{2}{\pi q\rho}} e^{-i(q\rho - m\pi/2 - \pi/4)} \quad , \quad \rho >> 1/q \tag{A.14}$$

Straightforward calculations then lead to

$$\int_{\rho=0}^{\infty} \left(\mathbf{F}_{\alpha}(\rho) \cdot \mathbf{F}_{\widetilde{\alpha'}}(\rho)\right)_{\substack{\beta=\beta' \\ m=m'}} \rho d\rho =$$

$$\frac{4}{qq'\sqrt{qq'}}\Big(\left((qq'+\beta^2)C_{\alpha}^{+}C_{\alpha'}{}^{-} - \frac{\mu_0}{\varepsilon_0\varepsilon_2}\sqrt{(\beta^2+q^2)(\beta^2+q'^2)}D_{\alpha}^{+}D_{\alpha'}^{-}\right)\delta^{+}(q-q') +$$

$$\left((qq'+\beta^2)C_{\alpha}^{-}C_{\alpha'}^{+} - \frac{\mu_0}{\varepsilon_0\varepsilon_2}\sqrt{(\beta^2+q^2)(\beta^2+q'^2)}D_{\alpha}^{-}D_{\alpha'}^{+}\right)\delta^{-}(q-q')\Big)(-1)^m$$

$$+\text{non-singular terms}, \tag{A.15}$$

where

$$\delta^{\pm}(q-q') = \frac{1}{2\pi}\int_{\rho=0}^{\infty} e^{\pm i(q-q')\rho}d\rho. \tag{A.16}$$

Note that $\delta(q-q') = \delta^{+}(q-q') + \delta^{-}(q-q')$.

The polarization indices p, p' represent a specific choice of the sets of coefficients A_α, B_α and $A_{\alpha'}$, $B_{\alpha'}$ for $\alpha = \{m, p, \beta, q\}$ and $\alpha' = \{m, p', \beta, q\}$. A convenient choice of coefficients is $A_\alpha = 1$, $A_{\alpha'} = 1$, $B_\alpha = i\eta$, $B_{\alpha'} = -i\eta$, since η can be chosen in such a way that the two polarization modes are biorthogonal. The requirement for two modes to be biorthogonal is obtained from (A.15), i.e.

$$C_{\alpha}^{+}C_{\alpha'}^{-} - \frac{\mu_0}{\varepsilon_0\varepsilon_2}D_{\alpha}^{+}D_{\alpha'}^{-} = C_{\alpha}^{-}C_{\alpha'}^{+} - \frac{\mu_0}{\varepsilon_0\varepsilon_2}D_{\alpha}^{-}D_{\alpha'}^{+} = 0. \tag{A.17}$$

Using Eqs. (A.8-A.11) biorthogonal modes are obtained for

$$\eta^2 = \frac{\varepsilon_0\varepsilon_2}{\mu_0}\frac{\varepsilon_2 K_1 K_2 - L_1 L_2}{\varepsilon_2 K_1 K_2 - {\varepsilon_2}^2 M_1 M_2}. \tag{A.18}$$

For a homogeneous dielectric medium with dielectric constant ε_2 the equation (A.18) reduces to the well-known $\eta = \pm\sqrt{\frac{\varepsilon_0\varepsilon_2}{\mu_0}}$.

The normalization factor N_α is obtained from (A.12) and (A.15), i.e.

$$N_\alpha = \varepsilon_2(2\pi)^2 4\frac{\beta^2+q^2}{q^3}(C_{\alpha}^{+}C_{\alpha}^{-} - \frac{\mu_0}{\varepsilon_0\varepsilon_2}D_{\alpha}^{+}D_{\alpha}^{-})(-1)^m. \tag{A.19}$$

Appendix B

The transverse delta operator δ_T for non-homogeneous dielectric media

This appendix concerns the construction of the transverse delta operator δ_T related to a dielectric constant $\varepsilon(\mathbf{r})$. It is defined as the operator which projects an arbitrary vector field $\mathbf{F}(\mathbf{r})$ onto its transverse component $\mathbf{F}_T(\mathbf{r})$, i.e. $\delta_T \mathbf{F} = \mathbf{F}_T$, where

$$\mathbf{F} = \mathbf{F}_T + \mathbf{F}_{GL} \tag{B.1}$$

with $\nabla \cdot \mathbf{F}_T = 0$ and $\nabla \times (\mathbf{F}_{GL}/\varepsilon) = \mathbf{0}$.

By inspection one can easily verify that

$$\mathbf{F}_{GL} = \sum_n \frac{\varepsilon(\mathbf{r}) \nabla \phi_n(\mathbf{r})}{M_n} \int (\nabla \widetilde{\phi}_n(\mathbf{r}'))^* \cdot \mathbf{F}(\mathbf{r}') d^3 r' \ , \tag{B.2}$$

where ϕ_n and M_n are given by (4.28) and (4.29). The expression obviously satisfies the condition for $\mathbf{F}_{GL}/\varepsilon$ being longitudinal, and the completenes of the solutions to (4.28) ensures that $\mathbf{F} - \mathbf{F}_{GL}$ is transverse. Hence

$$\delta_T \mathbf{F} = \mathbf{F}_T = \mathbf{F} - \mathbf{F}_{GL}, \tag{B.3}$$

and

$$\delta_T^\dagger \mathbf{F}(\mathbf{r}) = \mathbf{F}(\mathbf{r}) - \sum_n \frac{\nabla \tilde{\phi}_n(\mathbf{r})}{M_n^*} \int (\varepsilon(\mathbf{r}') \nabla \phi_n(\mathbf{r}'))^* \cdot \mathbf{F}(\mathbf{r}') d^3 r' \ . \tag{B.4}$$

In the case of a passive structure (real ε) we have

$$\delta_T^\dagger \mathbf{E}_n = \mathbf{E}_n^T = \mathbf{E}_n, \tag{B.5}$$

and

$$\delta_T^\dagger \nabla \phi_n = \mathbf{0} \tag{B.6}$$

for a generalized transverse field $\mathbf{E}_n$ and for any solution ϕ_n to (4.28). For eq. (4.32) this implies that $\mathbf{G}_T = \mathbf{G}_{GT}$.

Appendix C

Derivation of driving term

In this appendix a derivation will be presented for the expressions (5.13)-(5.15). The following volume integral expression for $\mathbf{G}^b$

$$\mathbf{G}^b(\mathbf{r},\mathbf{r}_0) = \mathbf{G}(\mathbf{r},\mathbf{r}_0;1) - \mathbf{G}(\mathbf{r},\mathbf{r}_0;n) + \int_V \mathbf{G}(\mathbf{r},\mathbf{r}';1) {k_0}^2 (n^2-1) \cdot \mathbf{G}(\mathbf{r}',\mathbf{r}_0;n) d^3r' \tag{C.1}$$

will be converted into a surface integral expression.

We will consider the case where both positions $\mathbf{r}$ and $\mathbf{r}_0$ are inside the volume V and convert the volume integral into a surface integral by use of the Green theorems. The Green theorems cannot be applied directly to a volume integral with singularities in the integrand. The integral directly over the singularities at $\mathbf{r}$ and $\mathbf{r}_0$ can be calculated by enclosing the singularities by infinitesimally small spherical volumes δV_1 and δV_n. Here δV_1 is a sphere around $\mathbf{r}$, and δV_n is a sphere around $\mathbf{r}_0$. When integrating over the spheres δV_1 and δV_n one of the two Green's tensors can be treated as constant for $\mathbf{r} \neq \mathbf{r}_0$. The integral of the other Green's tensor over the sphere has been tabulated by Yaghjian [115]. The contribution to Eq. (C.1) from these small spheres is then given by

$$\int_{\delta V_1} \mathbf{G}(\mathbf{r},\mathbf{r}';1) {k_0}^2 (n^2-1) \cdot \mathbf{G}(\mathbf{r}',\mathbf{r}_0;n) d^3r' = -\frac{1}{3}(n^2-1)\mathbf{G}(\mathbf{r},\mathbf{r}_0;n) \ , \tag{C.2}$$

$$\int_{\delta V_n} \mathbf{G}(\mathbf{r},\mathbf{r}';1) {k_0}^2 (n^2-1) \cdot \mathbf{G}(\mathbf{r}',\mathbf{r}_0;n) d^3r' = -\frac{1}{3}\frac{n^2-1}{n^2}\mathbf{G}(\mathbf{r},\mathbf{r}_0;1) \ . \tag{C.3}$$

Before the Green theorems are applied the remaining integral is rewritten in a convenient form by use of the following Green's tensor relation

$$\mathbf{G}(\mathbf{r},\mathbf{r}';n) = \frac{1}{{k_0}^2 n^2}\left(\nabla\nabla - \mathbf{I}\nabla^2\right) g(\mathbf{r},\mathbf{r}';n) \ , \ \mathbf{r} \neq \mathbf{r}' \tag{C.4}$$

where the scalar green's function g is given by

$$g(\mathbf{r},\mathbf{r}';n) = \frac{e^{ik_0 n|\mathbf{r}-\mathbf{r}'|}}{4\pi \mid \mathbf{r}-\mathbf{r}' \mid} \quad . \tag{C.5}$$

In Eq. (C.4) the differentiations could also be with respect to the primed coordinates. We will use g_1 as shorthand notation for $g(\mathbf{r},\mathbf{r}';1)$ and g_n as shorthand notation for $g(\mathbf{r}',\mathbf{r}_0;n)$. The remaining volume integral may then be written

$$\begin{aligned} \int_{V\setminus\{\delta V_1\cup\delta V_n\}} \mathbf{G}(\mathbf{r},\mathbf{r}';1){k_0}^2(n^2-1)\cdot\mathbf{G}(\mathbf{r}',\mathbf{r}_0;n)d^3r' &= \\ \frac{n^2-1}{{k_0}^2n^2}\int_{V\setminus\{\delta V_1\cup\delta V_n\}}((\nabla'\nabla'g_1)\cdot(\nabla'\nabla'g_n) - (\nabla'\nabla'g_1)\nabla'^2 g_n &- \\ (\nabla'\nabla'g_n)\nabla'^2 g_1 + (\nabla'^2 g_1)(\nabla'^2 g_n))d^3r' &\quad , \end{aligned} \tag{C.6}$$

where the integral is over the volume V minus the volume regions δV_1 and δV_n. The integral can be transformed into a surface integral by use of the following formulas that we have derived using the Green theorems

$$\begin{aligned} \int_{V'}(\nabla'\nabla'g_1)\cdot(\nabla'\nabla'g_n)d^3r' &= \int_{\partial V'}(\hat{n}\nabla'g_1)\cdot\nabla'\nabla'g_n dS' \\ &- \int_{\partial V'} g_1\hat{n}\cdot\nabla'\nabla'\nabla'g_n dS' \\ &+ n^2\int_{V'}(\nabla'\nabla'g_n)\nabla'^2 g_1 d^3r' \quad , \end{aligned} \tag{C.7}$$

$$\begin{aligned} \frac{n^2-1}{n^2}\int_{V'}(\nabla'\nabla'g_1)\nabla'^2 g_n d^3r' &= \int_{\partial V'}(\hat{n}\cdot\nabla'g_n)\nabla'\nabla'g_1 dS' \\ &- \int_{\partial V'} g_n(\hat{n}\cdot\nabla')\nabla'\nabla'g_1 dS' \quad , \end{aligned} \tag{C.8}$$

$$\begin{aligned} (1-n^2)\int_{V'}(\nabla'\nabla'g_n)\nabla'^2 g_1 d^3r' &= \int_{\partial V'}(\hat{n}\cdot\nabla'g_1)\nabla'\nabla'g_n dS' \\ &- \int_{\partial V'} g_1(\hat{n}\cdot\nabla')\nabla'\nabla'g_n dS' \quad , \end{aligned} \tag{C.9}$$

$$\begin{aligned} \frac{n^2-1}{n^2}\int_{\partial V'}(\nabla'^2 g_1)(\nabla'^2 g_n)d^3r' &= -{k_0}^2\int_{\partial V'}(g_1\hat{n}\cdot\nabla'g_n \\ &- g_n\hat{n}\cdot\nabla'g_1)dS' \quad , \end{aligned} \tag{C.10}$$

where $\hat{n}$ is the outward surface normal-vector, V' refers to a general volume where the integrands are non-singular, and $\partial V'$ refers to the surface of the volume V'.

Thereby

$$\begin{aligned}
\int_{V\setminus\{\delta V_1\cup\delta V_n\}} \mathbf{G}(\mathbf{r},\mathbf{r}';1){k_0}^2(n^2-1)\cdot\mathbf{G}(\mathbf{r}',\mathbf{r}_0;n)d^3r' &= \\
\frac{n^2-1}{{k_0}^2n^2}\int_{\partial(V\setminus\{\delta V_1\cup\delta V_n\})} (\hat{n}\nabla' g_1\cdot\nabla'\nabla' g_n - (\hat{n}\cdot\nabla' g_1)\nabla'\nabla' g_n &- \\
\frac{n^2}{n^2-1}(\hat{n}\cdot\nabla' g_n)\nabla'\nabla' g_1 + \frac{n^2}{n^2-1}g_n(\hat{n}\cdot\nabla')\nabla'\nabla' g_1 &- \\
{k_0}^2\frac{n^2}{n^2-1}(g_1\hat{n}\cdot\nabla' g_n - g_n\hat{n}\cdot\nabla' g_1))dS' \ . &\qquad \text{(C.11)}
\end{aligned}$$

Note that the surface integral here includes an integration over both the surface of the volume V but also an integration over the surface of the infinitesimally small volumes δV_1 and δV_n. The integrands in the surface integrals are highly singular near the surfaces of δV_1 and δV_n. The contribution from the surfaces around these singularities result in terms containing both Green's functions and second derivatives ($\nabla\nabla$) of Green's functions.

A relatively simple integral over the surface of one of the small spheres is

$$\begin{aligned}
\int_{\partial\delta V_1}\hat{n}\nabla' g_1\cdot\nabla'\nabla' g_n dS' &\approx \int_{\partial\delta V_1}\frac{(\mathbf{r}'-\mathbf{r})(\mathbf{r}'-\mathbf{r})}{4\pi\mid\mathbf{r}'-\mathbf{r}\mid^4}dS'\cdot\nabla\nabla g(\mathbf{r},\mathbf{r}_0;n) \\
&\approx \frac{1}{3}\nabla\nabla g(\mathbf{r},\mathbf{r}_0;n) \ . \qquad \text{(C.12)}
\end{aligned}$$

Here it was sufficient to include only the most singular terms in ∇g_1.

In a similar way we obtain

$$\int_{\partial\delta V_1}\hat{n}\cdot\nabla' g_1\nabla'\nabla' g_n dS' \approx \nabla\nabla g(\mathbf{r},\mathbf{r}_0;n) \ , \qquad \text{(C.13)}$$

$$\int_{\partial\delta V_n}\hat{n}\cdot\nabla' g_n\nabla'\nabla' g_1 dS' \approx \nabla\nabla g(\mathbf{r},\mathbf{r}_0;1) \ , \qquad \text{(C.14)}$$

$$\int_{\partial\delta V_n}\hat{n}\cdot\nabla' g_n g_1 dS' \approx g(\mathbf{r},\mathbf{r}_0;1) \ , \qquad \text{(C.15)}$$

$$\int_{\partial\delta V_1}\hat{n}\cdot\nabla' g_1 g_n dS' \approx g(\mathbf{r},\mathbf{r}_0;n) \ . \qquad \text{(C.16)}$$

In order to evaluate the other surface integrals it becomes necessary to make the following taylor expansions

$$\begin{aligned}
g_n &\approx g(\mathbf{r},\mathbf{r}_0;n) + (\mathbf{r}'-\mathbf{r})\cdot\nabla g(\mathbf{r},\mathbf{r}_0;n) \\
&+ \frac{1}{2}(\mathbf{r}'-\mathbf{r})\cdot\nabla\nabla g(\mathbf{r},\mathbf{r}_0;n)\cdot(\mathbf{r}'-\mathbf{r}) \quad , \ \mathbf{r}'\approx\mathbf{r} \qquad \text{(C.17)}
\end{aligned}$$

$$\nabla' g_n \approx \nabla g(\mathbf{r},\mathbf{r}_0;n) + (\mathbf{r}'-\mathbf{r})\cdot\nabla\nabla g(\mathbf{r},\mathbf{r}_0;n) \quad , \ \mathbf{r}' \approx \mathbf{r} \tag{C.18}$$

$$\nabla' g_1 \approx \nabla' g(\mathbf{r},\mathbf{r}';1)\mid_{\mathbf{r}'=\mathbf{r}_0} + (\mathbf{r}'-\mathbf{r}_0)\cdot\nabla\nabla g(\mathbf{r},\mathbf{r}_0;1) \quad , \ \mathbf{r}' \approx \mathbf{r}_0 \tag{C.19}$$

These expansions allow us to deal with singularities of higher order as compared to Eqs. (C.12)-(C.16). As an example we consider the term

$$\int_{\partial\delta V_n} \hat{n}\nabla' g_1 \cdot \nabla'\nabla' g_n dS' = \int_{\partial\delta V_n} -\frac{\mathbf{R}'}{R'}\left(\nabla g(\mathbf{r},\mathbf{r}_0;1) + \mathbf{R}'\cdot\nabla\nabla g(\mathbf{r},\mathbf{r}_0;1)\right)\cdot$$
$$k_0{}^2 n^2 \left(\mathbf{I}\left[\frac{i}{k_0 n R'} - \frac{1}{k_0{}^2 n^2 R'^2}\right] - \frac{\mathbf{R}'}{R'}\frac{\mathbf{R}'}{R'}\left[\frac{3i}{k_0 n R'} - \frac{3}{k_0{}^2 n^2 R'^2}\right]\right) g_n dS' \tag{C.20}$$

where $\mathbf{R}' = \mathbf{r}' - \mathbf{r}_0$ and $R' = \mid \mathbf{r}' - \mathbf{r}_0 \mid$. Some terms in Eq. (C.20) can be immediately discarded because for the spherical exclusion volumes chosen here

$$\int_{\partial\delta V_n} \frac{\mathbf{R}'}{R'} dS = \mathbf{0} \quad , \tag{C.21}$$

$$\int_{\partial\delta V_n} \frac{\mathbf{R}'}{R'}\frac{\mathbf{R}'}{R'}\frac{\mathbf{R}'}{R'} dS = \mathbf{0} \quad . \tag{C.22}$$

This leaves us with the following

$$\int_{\partial\delta V_n} \hat{n}\nabla' g_1 \cdot \nabla'\nabla' g_n dS' = \int_{\partial\delta V_n} -\frac{\mathbf{R}'}{R'}\frac{\mathbf{R}'}{R'}\cdot(\nabla\nabla g(\mathbf{r},\mathbf{r}_0;1))\cdot$$
$$k_0{}^2 n^2 \left(\mathbf{I}\left[-\frac{1}{k_0{}^2 n^2}\right] - \frac{\mathbf{R}'}{R'}\frac{\mathbf{R}'}{R'}\left[-\frac{3}{k_0{}^2 n^2}\right]\right)\frac{1}{4\pi}\frac{1}{R'^2} dS'$$
$$= \frac{1}{3}\nabla\nabla g(\mathbf{r},\mathbf{r}_0;1) - 3\nabla\nabla g(\mathbf{r},\mathbf{r}_0;1) : \mathbf{M} \ , \tag{C.23}$$

where

$$\mathbf{M} = \int_{\partial\delta V_n} \frac{\mathbf{R}'}{R'}\frac{\mathbf{R}'}{R'}\frac{\mathbf{R}'}{R'}\frac{\mathbf{R}'}{R'}\frac{1}{R'^2}\frac{1}{4\pi} dS' \tag{C.24}$$

is a compound of four vectors grouped together or two dyadics grouped together. The symbol : is a double dot-product such that for vectors $\mathbf{v}_1$, $\mathbf{v}_2$, $\mathbf{v}_3$, $\mathbf{v}_4$

$$(\mathbf{v}_1\mathbf{v}_2) : (\mathbf{v}_3\mathbf{v}_4) = (\mathbf{v}_2\cdot\mathbf{v}_3)(\mathbf{v}_1\cdot\mathbf{v}_4) \quad . \tag{C.25}$$

In a similar way we obtain

$$\int_{\partial\delta V_n} \hat{n}\cdot\nabla' g_1 \nabla'\nabla' g_n dS' = \frac{1}{3}\nabla^2 g(\mathbf{r},\mathbf{r}_0;1)\mathbf{I}$$
$$- \ 3\nabla\nabla g(\mathbf{r},\mathbf{r}_0;1) : \mathbf{M} \ , \tag{C.26}$$

$$\int_{\partial\delta V_1} \hat{n}\cdot\nabla' g_n \nabla'\nabla' g_1 dS' = \frac{1}{3}\nabla^2 g(\mathbf{r},\mathbf{r}_0;n)\mathbf{I} - 3\nabla\nabla g(\mathbf{r},\mathbf{r}_0;n):\mathbf{M} \ , \quad \text{(C.27)}$$

where we have used

$$\nabla\nabla g : \mathbf{I}\,\mathbf{I} = \nabla^2 g \mathbf{I} \ . \quad \text{(C.28)}$$

The last term to consider in detail is

$$\int_{\partial\delta V_1} g_n \hat{n}\cdot\nabla'\nabla'\nabla' g_1 dS' \approx \int_{\partial\delta V_1} (g(\mathbf{r},\mathbf{r}_0;n) + (\mathbf{r}'-\mathbf{r})\cdot\nabla g(\mathbf{r},\mathbf{r}_0;n) + \frac{1}{2}(\mathbf{r}'-\mathbf{r})\cdot\nabla\nabla g(\mathbf{r},\mathbf{r}_0;n)\cdot(\mathbf{r}'-\mathbf{r}))\hat{n}\cdot\nabla'\nabla'\nabla' g_1 dS' \quad \text{(C.29)}$$

In this case only those terms in Eq. (C.29) that are proportional to $g(\mathbf{r},\mathbf{r}_0;n)$ and $\nabla\nabla g(\mathbf{r},\mathbf{r}_0;n)$ are nonzero for the integration over the surface of the spherical exclusion volume δV_n. These non-zero terms are

$$g(\mathbf{r},\mathbf{r}_0;n)\int_{\partial\delta V_1} \hat{n}\cdot\nabla'\nabla'\nabla' g_1 dS' = -\frac{1}{3}{k_0}^2\mathbf{I}g(\mathbf{r},\mathbf{r}_0;n) \ , \quad \text{(C.30)}$$

$$\nabla\nabla g(\mathbf{r},\mathbf{r}_0;n) : \int_{\partial\delta V_1} \frac{\mathbf{R}}{R}\frac{\mathbf{R}}{R}\hat{n}\cdot\nabla'\nabla'\nabla' g_1 dS' = -\nabla^2 g(\mathbf{r},\mathbf{r}_0;n)\mathbf{I} + 9\nabla\nabla g(\mathbf{r},\mathbf{r}_0;n):\mathbf{M} \ , \quad \text{(C.31)}$$

where $\mathbf{R} = \mathbf{r}' - \mathbf{r}$. The above expressions can now be evaluated by use of the following property of the four vector compound $\mathbf{M}$

$$\mathbf{A}:\mathbf{M} = \frac{1}{15}\left(Tr\,(\mathbf{A})\,\mathbf{I} + \mathbf{A} + \mathbf{A}^T\right) \quad \text{(C.32)}$$

where the dyadic $\mathbf{A}$ can be arbitrary. Here ^{T} refers to the transpose, and Tr refers to the trace or sum of diagonal elements. However, for the cases of interest here $\mathbf{A}$ will be the symmetric dyadic $\nabla\nabla g(\mathbf{r},\mathbf{r}_0;n)$ or $\nabla\nabla g(\mathbf{r},\mathbf{r}_0;1)$, and consequently the transpose operation will have no effect, i.e.

$$\nabla\nabla g : \mathbf{M} = \frac{1}{15}\left(\nabla^2 g\mathbf{I} + 2\nabla\nabla g\right) \ . \quad \text{(C.33)}$$

After inserting expressions (C.12)- (C.16), (C.23), (C.26), (C.27), and (C.29)-(C.31) into Eq. (C.11), adding the terms (C.2), (C.3) then finally by use of

Eq. (C.4) we obtain the main result of this appendix, namely

$$\begin{aligned}
\int_V \mathbf{G}(\mathbf{r},\mathbf{r}';1){k_0}^2(n^2-1)\cdot\mathbf{G}(\mathbf{r}',\mathbf{r}_0;n)d^3r' &= \\
\mathbf{G}(\mathbf{r},\mathbf{r}_0;n)-\mathbf{G}(\mathbf{r},\mathbf{r}_0;1) &+ \\
\frac{n^2-1}{{k_0}^2n^2}\int_{\partial V}(\hat{n}\nabla' g_1\cdot\nabla'\nabla' g_n-(\hat{n}\cdot\nabla' g_1)\nabla'\nabla' g_n &- \\
\frac{n^2}{n^2-1}(\hat{n}\cdot\nabla' g_n)\nabla'\nabla' g_1+\frac{n^2}{n^2-1}g_n(\hat{n}\cdot\nabla')\nabla'\nabla' g_1 &- \\
\mathbf{I}{k_0}^2\frac{n^2}{n^2-1}(g_1\hat{n}\cdot\nabla' g_n-g_n\hat{n}\cdot\nabla' g_1))dS' \ . &\qquad \text{(C.34)}
\end{aligned}$$

Thereby we see that the volume integral expression for $\mathbf{G}^b$ has now been transformed into a surface integral, where the integral can be a surface far away from the Green's tensor singularities. Clearly $\mathbf{G}^b$ is non-singular. The expression (C.34) refers to the case where both positions $\mathbf{r}$ and $\mathbf{r}_0$ are inside the volume V. In the case where $\mathbf{r}$ is outside the volume V the only difference will be that the term $\mathbf{G}(\mathbf{r},\mathbf{r}_0;n)$ in Eq. (C.34) should be omitted. The results Eq. (5.13)-(5.15) are now directly obtained from Eq. (C.1) and Eq. (C.34).

Note that for the case of absorbing media, or passive media when the retarded Green's function is considered, the Green's functions decay exponentially with distance for large distances. Therefore, if we consider a volume with refractive index n taking up the whole three-dimensional space, and the surface of V is therefore placed at infinity, the surface integral in Eq. (C.34) vanishes. In that case we are left with the following simple integral equation relation between two Green's tensors for different homogeneous media

$$\mathbf{G}(\mathbf{r},\mathbf{r}_0;n)=\mathbf{G}(\mathbf{r},\mathbf{r}_0;1)+\int\mathbf{G}(\mathbf{r},\mathbf{r}';1){k_0}^2(n^2-1)\cdot\mathbf{G}(\mathbf{r}',\mathbf{r}_0;n)d^3r' \qquad \text{(C.35)}$$

Appendix D

Acknowledgements

During the three years that I have studied for the ph.d-degree I have encountered many individuals that I would like to acknowledge for discussions and cooperation.

I would like to give a special thanks to Bjarne Tromborg for our cooperations, in particular the cooperation on a general theory for spontaneous emission, for our many discussions on mathematical issues, and for bringing me in contact with the group of Daan Lenstra, Vrije Universiteit (VU), Amsterdam, The Netherlands. During the course of the ph.d-work I stayed six months at VU. I would like to thank Daan Lenstra and the people that I encountered at VU for their hospitality during this time.

Anders Bjarklev, Jes Broeng, and Stig E. Barkou are acknowledged for having introduced me to the field of photonic crystals and for our cooperations. Anders Bjarklev is furthermore acknowledged for opening doors to participation in the PICCO project and COST 268 meetings, and for bringing me in contact with various people with whom I have had fruitful cooperations within the ph.d-project.

Martin Kristensen and Jesper Arentoft are acknowledged for our cooperation on semiconductor-on-insulator based planar photonic crystal waveguides in relation to the PICCO project.

Kim Dridi is acknowledged for our cooperation on the energy flow in planar photonic crystal waveguides.

Andrei Lavrinenko is acknowledged for our cooperation on large-bandwidth photonic crystal waveguides. T.F. Krauss is acknowledged for pointing out the need for design of large-bandwidth photonic crystal waveguides.

I have also enjoyed the interaction and cooperation with M.G. Dyndgaard, A. Tycho, E. Knudsen, J. Erland and A. Boltasseva.

Finally I would like to acknowledge the anonymous referees for their useful comments and suggestions to my manuscripts.

Appendix E

List of publications

List of first-authored journal papers.

T. Søndergaard, J. Broeng, A. Bjarklev, K. Dridi and S.E. Barkou, "Suppression of spontaneous emission for a two-dimensional honeycomb photonic bandgap structure estimated using a new effective-index model", IEEE J. Quantum Electron., vol. 34, 2308-13, 1998.

T. Søndergaard, "Spontaneous emission in two-dimensional photonic crystal microcavities", IEEE J. Quantum Electron., vol. 36, 450-7, 2000.

T. Søndergaard, "Photonic crystal distributed feedback fiber lasers with Bragg gratings", J. Lightwave Technol., vol. 18, 589-97, 2000.

T. Søndergaard and K.H. Dridi, "Energy flow in photonic crystal waveguides", Phys. Rev. B, vol. 61, 15688-96, 2000.

T. Søndergaard, A. Bjarklev, M. Kristensen, J. Erland, and J. Broeng, "Designing finite-height two-dimensional photonic crystal waveguides", Appl. Phys. Lett., vol. 77, 785-7, 2000.

T. Søndergaard and B. Tromborg, "General theory for spontaneous emission in active dielectric microstructures: Example of a fiber amplifier", Phys. Rev. A, vol. 64, 033812, 2001.

T. Søndergaard, A. Bjarklev, J. Arentoft, M. Kristensen, J. Erland, J. Broeng, S.E. Barkou Libori, "Designing finite-height photonic crystal waveg-

uides: confinement of light and dispersion relations", Opt. Comm., vol. 194, 341-51, 2001.

T. Søndergaard, D. Lenstra and B. Tromborg, "Near fields and far fields generated by sources in the presence of dielectric structures with cylindrical symmetry", Opt. Lett., vol. 26, 1705-7, 2001.

T. Søndergaard, J. Arentoft, A. Boltasseva, A. Lavrinenko, M. Kristensen, and B. Tromborg, "Planar photonic crystal waveguides", DOPS-NYT 2-2001, p. 35-39.

T. Søndergaard, J. Arentoft, and M. Kristensen, "Theoretical analysis of finite-height semiconductor-on-insulator based planar photonic crystal waveguides", submitted to J. Lightwave Technol. in Sept. 2001, Accepted subject to revisions in Jan. 2002.

T. Søndergaard and A. Lavrinenko, "Large-bandwidth planar photonic crystal waveguides", submitted to Opt. Comm. in Nov. 2001, Accepted subject to revisions in Jan. 2002.

List of coauthored journal papers.

J. Broeng, T. Søndergaard, S.E. Barkou, P.M. Barbeito, and A. Bjarklev, "Waveguidance by the photonic bandgap effect", J. Optics A: Pure Appl. Opt., vol. 1, 477-82, 1999.

J.B. Nielsen, T. Søndergaard, S.E. Barkou, A. Bjarklev, J. Broeng, and M.B. Nielsen, "Two-dimensional Kagomé structure, fundamental hexagonal photonic crystal configuration", Electron. Lett., vol. 35, 1736, 1999.

J.B. Nielsen, T. Søndergaard, S.E. Barkou, A. Bjarklev, and J. Broeng, "Two-dimensional Kagomé photonic bandgap waveguide, IEEE Photon. Technol. Lett., vol. 12, 630-2, 2000.

A. Bjarklev, J. Broeng, S.E. Barkou, E. Knudsen, T. Søndergaard, T.W. Berg, and M.G. Dyndgaard, "Polarization properties of honeycomb-structured photonic bandgap fibres", J. Opt. A: Pure Appl. Opt., vol. 2, 584-8, 2000.

J. Broeng, S.E. Barkou, T. Søndergaard, and A. Bjarklev, "Analysis of air-guiding photonic bandgap fibers", Opt. Lett., vol. 25, 96-98, 2000.

J. Broeng, S.E. Barkou, A. Bjarklev, T. Søndergaard, and E. Knudsen, "Review paper: crystal fibre technology", DOPS-NYT, vol. 15, 22-28, 2000.

M.G. Dyndgaard, T. Søndergaard, J. Broeng, A.O. Bjarklev, S.A. Guldberg-Kjær, and M.R. Poulsen, "Design optimisation of erbium-doped planar waveguide DBR lasers", OSA, Trends in Optics and Photonics (TOPS), vol. 30, 140-46, 1999.